Doctoral Thesis
博士論文

Plasma Current Start-up by the Lower Hybrid Wave Using Capacitively-Coupled Combline Antennas on the TST-2 Spherical Tokamak
(球状トカマク TST-2 における静電結合型コムラインアンテナを使った低域混成波によるプラズマ電流立ち上げ)

A Thesis Submitted for Degree of Doctor of Philosophy
December 2018

平成 30 年 12 月博士(理学)申請

Department of Physics, Graduate School of Science,
The University of Tokyo

東京大学大学院理学系研究科物理学専攻

Satoru Yajima

矢嶋　悟

Contents

List of abbreviations

AXUV Absolute eXtreme UltraViolet

CCCA Capacitively-Coupled Combline Antenna

CCW CounterClockWise

CS Central Solenoid

CW ClockWise

DT Deuterium-Tritium

ECH Electron Cyclotron Heating

ECW Electron Cyclotron Wave

FW Fast Wave

LHW Lower Hybrid Wave

OH Ohmic Heating

RF Radio Frequency

SBD Surface Barrier Diode

SOL Scrape-Off Layer

ST Spherical Tokamak

Abstract

The tokamak is presently the most promising magnetic confinement system for the first power-producing nuclear fusion reactor because of its capability to achieve high ion temperature and high density with good confinement and adequate stability. In the tokamak, a toroidal plasma current must be driven in order to produce the poloidal magnetic field necessary for plasma confinement. The use of the lower hybrid wave (LHW) is a promising candidate for driving the plasma current non-inductively and sustaining it in a steady state. Plasma current ramp-up by the LHW is being studied on the TST-2 spherical tokamak. Based on the results of ray-tracing calculations using GENRAY, which predicted that launching the LHW from the top side of the plasma has many beneficial effects, the top-launch antenna was designed, fabricated, and installed in TST-2. The beneficial effects include avoidance of the density limit for current drive, propagation of the LHW to the plasma core, and improvement of the single-pass absorption of the LHW because of the strong upshift of the parallel index of refraction $N_{\parallel} = ck_{\parallel}/\omega$ as the wave propagates into the plasma. Installation of the top-launch antenna enabled comparison of the three launching scenarios: outboard launch, top-launch, and simulated bottom launch. The simulated bottom launch is realized by using the top-launch antenna with a reversed toroidal magnetic field. According to GENRAY / CQL3D (iterated ray-tracing and Fokker-Planck) calculations, in the cases of top launch and simulated bottom launch, the LHW wave number variation (wave number upshift in the case of top launch and wave number downshift in the case of simulated bottom launch) depends on the magnetic field pitch angle. The wave number ranges of the propagating LHW for these cases become broader than that for the case of outboard launch. The achievable plasma current can be improved by broadening the wave number range for Landau damping. The installation of the top-launch antenna resulted in the restriction of the plasma cross section, which caused the reduction in the achievable plasma current using the outboard-launch antenna from 25 kA to 21.1 kA. However, because of the superiority of the top-launch antenna for current drive, the maximum plasma current increased to 26 kA for top launch and 26.7 kA for simulated bottom launch.

The $N_{\parallel}$ upshift observed in GENRAY calculations for top launch could not be explained by the known effects of magnetic shear or magnetic field gradient in the poloidal

direction. A theoretical explanation of $N_{\|}$ upshift was discussed in the framework of cold plasma, electrostatic approximation using the pitch angle of the magnetic field line, plasma density, and magnetic field strength. Investigation of the plasma current dependent $N_{\|}$ upshift calculated by GENRAY using a rescaled magnetic field pitch angle gave a qualitative agreement with the experimental observation that the intensity of soft X-ray emission in the energy range 200–300 eV, considered to be produced by a large $N_{\|}$ upshift, increased abruptly for discharges with plasma current above 15 kA. GENRAY / CQL3D calculations confirmed that soft X-ray emission in this energy range increased abruptly as the plasma current increased above 16 kA.

In order to investigate the $N_{\|}$ spectrum of the LHW excited in the plasma, finite element calculations were performed using COMSOL Multiphysics. Based on the ion and electron density profile data measured previously by Langmuir probes, the transmissivity of the outboard-launch antenna and the RF electric field distribution in the vicinity of the antenna were calculated. For both outboard-launch and top-launch antennas, the peak of the $N_{\|}$ spectrum did not change significantly from the spectrum measured during antenna tuning in the air (with the main peak around $N_{\|} = -5$). In the case of the outboard-launch antenna, COMSOL calculation revealed that the limiter plates installed on both sides of the antenna for reducing the density in front of the antenna reflect a significant fraction of the excited LHW, which produces an oppositely propagating peak in the $N_{\|}$ spectrum which is a mirror image of the main LHW peak. COMSOL calculations also showed that the reflection can be reduced to an insignificant level by moving the limiter farther away by 70 mm toroidally. For the top-launch antenna, COMSOL calculations were performed to investigate the dependence on the distance from the antenna surface to the plasma cutoff layer where the LHW starts to propagate, using the same density gradient as for the outboard-launch antenna. As the distance between the antenna and the cutoff layer becomes smaller, the antenna transmissivity decreases, which means that the power radiated into the plasma increases. However, when the distance becomes too small, a short wavelength component that propagates in the opposite direction becomes excited. The optimum distance between the antenna and the cutoff layer was determined to be 17–27 mm with the corresponding antenna transmissivity of 18–40%.

This research aims to explore the applicability of the LHW for non-inductive tokamak plasma start-up, and has the following significances: (1) Comparison of current drive performance among three different launching locations (outboard launch, top launch, and simulated bottom launch) enabled discussions of optimizing operation scenario for the plasma current ramp-up phase. (2) Wave propagation and $N_{\|}$ evolution during the plasma current ramp-up phase were studied both numerically and analytically, and a satisfactory agreement with experimental results was obtained. (3) LHW excitation by Capacitively-coupled combline antennas was modeled by COMSOL and the conditions for maintaining the desired $N_{\|}$ spectrum were investigated. Such analyses gave us guidance on antenna performance improvement and future antenna design.

Chapter 1

Introduction

1.1 Nuclear fusion

There are several attractive points in utilizing nuclear fusion reactions. First of all, discharged energy per single chemical reaction is of the order of eVs, while the energy per single nuclear reaction is of the order of MeVs. Additionally, unlike nuclear fission, nuclear fusion is not relying on a chain reaction which may become destructive and uncontrollable.

In order to realize the nuclear fusion reaction, the ions must overcome the Coulomb barrier of each other. The radius of a nucleus is roughly square root of the number of nucleons, so the height of Coulomb barrier is proportional to $qA^{-1/3}$, where q is the ion charge, A is the number of nucleons, and q basically increases quicker than $A^{1/3}$ as A increases. The ion source for nuclear fusion is hydrogen because of its lower binding energy (Fig. 1.1) and lower Coulomb barrier. Hydrogen can easily be extracted from water in the sea, which means that the fuel is nearly inexhaustible. As a reaction product, helium has large binding energy, and therefore any reaction which produces helium gives large energy. The most promising reaction is a deuterium-tritium (DT) reaction because of its higher reaction rate due to lower Coulomb barrier compared with single proton (Fig. 1.2). The target ion temperature is above 10 keV but not more than 100 keV [1].

1.2 Tokamak

The tokamak configuration (Fig. 1.3) can confine high-temperature plasmas suitable for a fusion reactor for long enough duration [4, 5], and is presently the most promising candidate for the first generation fusion reactor. When there is a strong enough magnetic field, charged particles gyrate around the magnetic field line while they are free to move along the magnetic field line. In order to eliminate losses along the magnetic field,

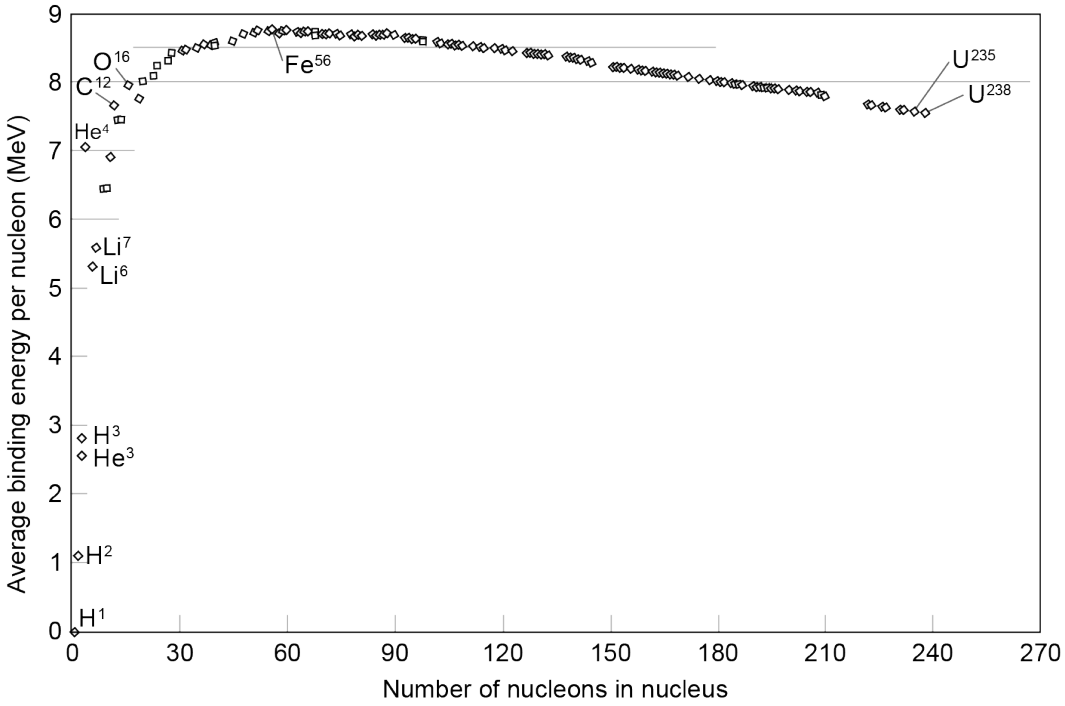

Figure 1.1: Binding energies of various nuclei [2].

a strong circular magnetic field (called the toroidal magnetic field) is created by toroidal magnetic field coils which surround a torus where the plasma is produced and confined. However, with the toroidal magnetic field alone, charged particles quickly drift out of the torus because of magnetic field inhomogeneity and magnetic field curvature. In order to avoid this loss, the poloidal magnetic field (in the direction short way around the torus) must be superposed. The charged particles mostly move along the helically twisted magnetic field lines, and the displacement from the magnetic field lines due to the drift is significantly reduced. In the tokamak, the poloidal magnetic field is generated by the current flowing inside the plasma in the toroidal direction (this is called the plasma current). In the tokamak, one of the most important requirements is to drive the plasma current with high enough efficiency. Since a toroidal current tends to expand outward (in the major radial direction), the vertically oriented magnetic field (called the vertical magnetic field) is required to apply a canceling inwardly directed $\boldsymbol{j} \times \boldsymbol{B}$ force to maintain force balance in the major radial direction.

Generally, in designing a nuclear fusion reactor by a magnetic field confinement system, it is necessary to have a cycle for sustaining the DT reaction continuously. Supply of deuterium can be almost inexhaustibly covered by extracting it from sea water, but it is not easy to extract tritium in the same way. For sufficient production of tritium,

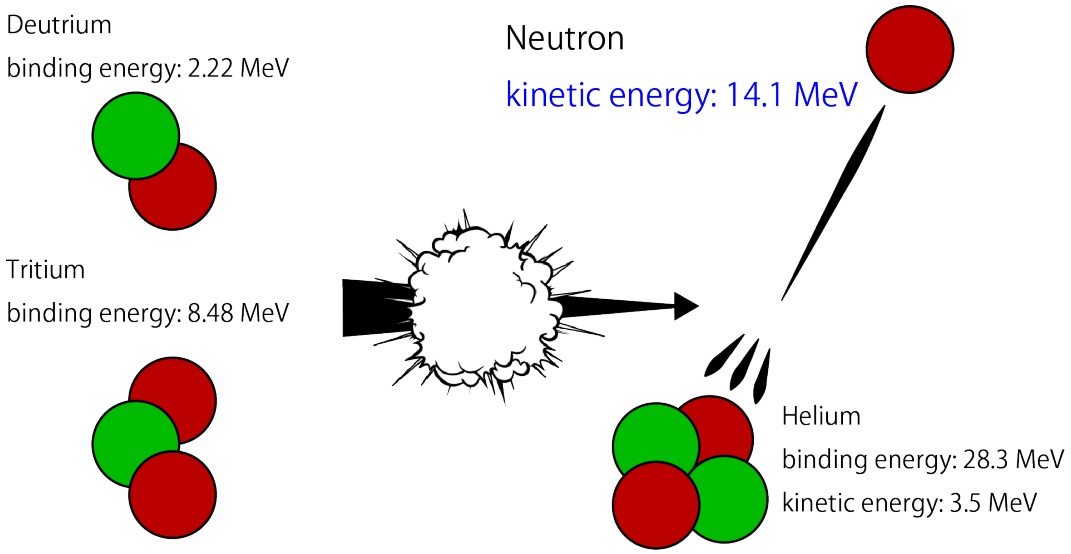

Figure 1.2: An illustration of D-T reaction [3].

it is considered to use the wall containing lithium. The high energy neutrons generated after the DT reaction can be decelerated to heat after undergoing the following processes:

$$^{6}\mathrm{Li} + \mathrm{n} \rightarrow {}^{4}\mathrm{He} + \mathrm{T} \tag{1.2.1}$$

$$^{7}\mathrm{Li} + \mathrm{n} \rightarrow {}^{4}\mathrm{He} + \mathrm{T} + \mathrm{n}. \tag{1.2.2}$$

At the same time, tritium can be released, so a fuel cycle for sustaining the reaction is established.

1.3 Spherical tokamak

A class of tokamak with a small aspect ratio ($A = R_0/a$, where R_0 is the major radius of the plasma center and a is the minor radius of the toroidal plasma) of typically less than 2 is called the spherical tokamak (ST) because the plasma shape approaches a sphere with the central cylinder removed [7] (Fig. 1.4). In the ST configuration, the plasma cross section is D-shaped, and because of small A, the ratio of the toroidal magnetic field B_t on the inboard side and outboard side of the torus is very large. Combined with the high pressure capability which increases the poloidal magnetic field B_p on the outboard side and reduces B_p on the inboard side, the helical magnetic field line is much longer on the inboard side (where the plasma is stable because the magnetic field line is convex towards the plasma) than on the outboard side (where the plasma is unstable because the magnetic field line is convex away from the plasma). This leads to improved

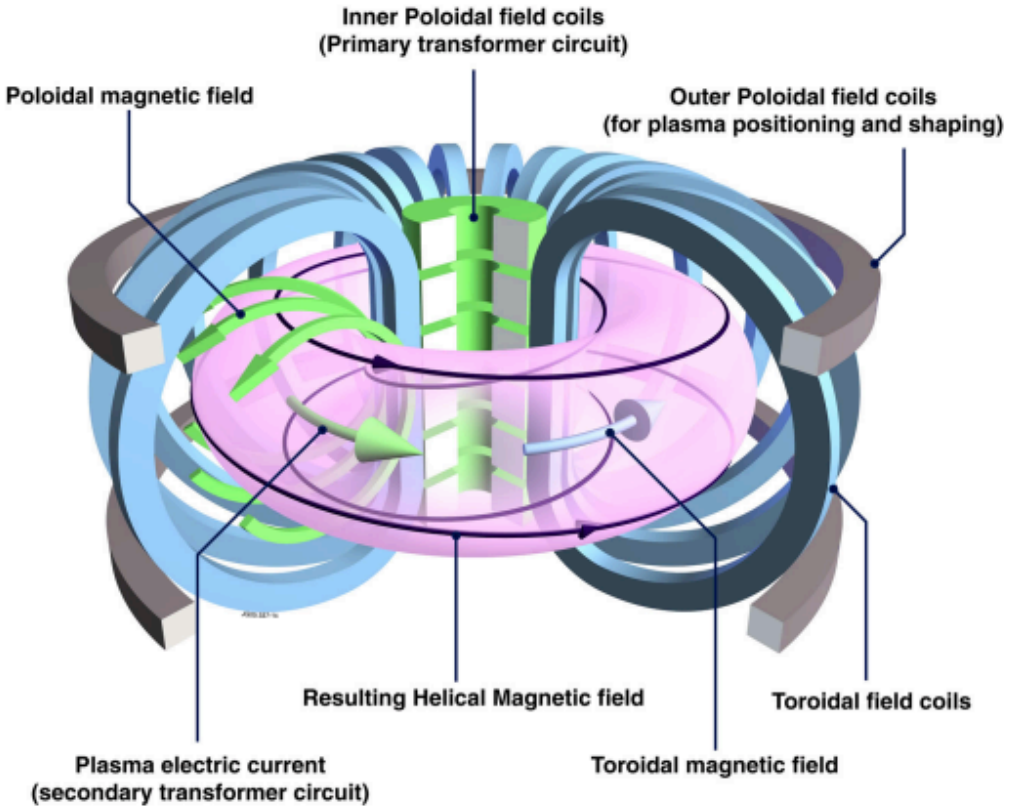

Figure 1.3: Tokamak configuration [6].

stability of the ST plasma compared to the conventional tokamak plasma [8]. Because of the improved stability, ST plasmas can remain stable up to higher levels of the normalized plasma pressure ($\beta = 2\mu_0\langle p\rangle/B^2$ where $\langle p\rangle$ is the volume averaged plasma pressure), a substantial fraction of the plasma current can be driven spontaneously by the plasma. Numerical studies show that the ratio of the self-driven plasma current to the total plasma current can approach 100%. Since the self-driven current reduces the requirement for external power for the current drive, this is a great advantage for the economic competitiveness of a fusion reactor.

In the tokamak (including ST), the plasma current, needed for equilibrium and confinement, is driven by magnetic induction with the central solenoid (CS) which is the coil located on the inboard side of the torus. This coil is also called the Ohmic heating (OH) coil or the transformer coil. However, because of the magnetic flux capability and the need to shield the coil from neutron bombardment, it is impractical to design a D-T fusion ST reactor with the CS. If the function of the CS (ramping up and sustaining the plasma current) can be substituted by other means, such as current

drive using plasma waves, ST fusion reactor would become more practical.

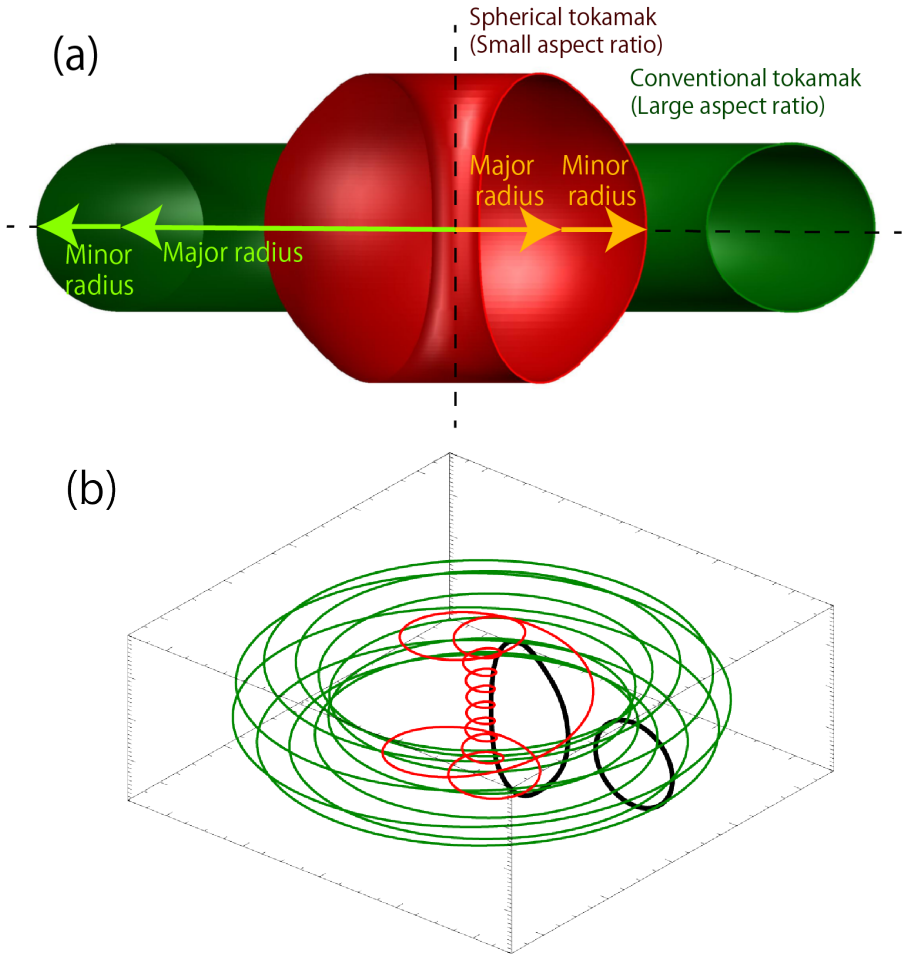

Figure 1.4: (a) Spherical tokamak compared to the conventional tokamak. (b) The tokamak edge shapes (black) and typical magnetic field lines in a spherical tokamak (red) and the conventional tokamak (green) [9].

1.4 Previous studies of lower hybrid current drive experiments in TST-2

In order to create high-performance fusion plasmas with a low aspect ratio and to maintain the fusion reaction in a steady state, a non-inductive method to ramp up the plasma current and sustain it must be developed to eliminate the need for the CS. On

the TST-2 spherical tokamak [10–12], experiments using LHW have been conducted to investigate the capability of the LHW [13–15] for ST plasma formation and initial plasma current ramp-up [16–18]. The previous research on the current drive using the LHW with different antennas are reported in Refs. [19, 20]. For current drive experiments using lower hybrid wave (LHW), the current drive experiments using a waveguide array antenna (which is called grill antenna) were initially performed in TST-2 [21]. The wave number scan of the LHW was performed using the antenna, and the optimum wave number of LHW in TST-2 ($N_{\parallel} = -5$, where $N_{\parallel}$ is the parallel refractive index for LHW and the sign shows the direction along toroidal magnetic field) was decided from both of the generation efficiency of fast electrons responsible for the plasma current and the power injection efficiency into the plasma. The antennas presently in use on TST-2 are novel antennas developed specifically for the present experiment. They can excite the LHW traveling unidirectionally in one toroidal direction, and are called the capacitively-coupled combline (CCC) antennas. In addition to the sharp wavenumber spectrum and the high directionality of the excited LHW, this type of antenna is simple, requires only one RF input port, and requires no matching network. Though the injected wave number was fixed, the directivity of the wave number spectrum was greatly improved and the current driving efficiency was also increased [22]. By using this antenna, the plasma current of 25 kA was achieved [23], which was about 20 % of the driven current by inductive startup method in TST-2 (120 kA). The initial experiment was performed with the antenna installed on the outboard side of the plasma (outboard-launch antenna). An additional antenna was installed on the top side of the plasma (top-launch antenna) [24], guided by numerical simulations of wave propagation, absorption, and current drive.

1.5 Thesis objective

In the previous study, the initial result of the LHW top injection experiment was shown to prove the validity of the top launching. Therefore, as the next step, from both experimental and numerical view, it was essential to compare the wave propagation and the current generation characteristics among the different launching locations (top, outboard, and bottom sides) to extract the significant and apparent differences in the physics related to the electron acceleration and the formation of the electron velocity distribution.

After the installation of the top launch, it was necessary to adjust the height of the top limiter for suppressing the plasma density in the vicinity of the antenna. Since the influence on the driven current by the limiter location was unrevealed, it was necessary to investigate the effect of comparative experiments for each limiter location to confirm the better way to optimize the plasma current.

The directivity of the wave number spectrum generated from the antenna is substan-

tially related to the current drive efficiency. Though this property was confirmed in the laboratory, it is still unconfirmed whether the wave number spectrum is maintained in any condition in the plasma presence. Understanding the injected wave number characteristics of the LHW considering the antenna-plasma interaction and investigating conditions for maintaining ideal wave property is essential for antenna control. In this paper, we investigated the LHW launching condition by utilizing the three-dimensional electromagnetic field simulation considering the antenna structure and dielectric constant of the plasma.

Chapter 2

Plasma Wave Theory

2.1 Plasma frequency and Debye length

Plasma is a collection of charged particles (electrons and ions) and can be represented as a highly conductive medium. Since plasma particles can move freely under the influence of electromagnetic fields, one important characteristic of the plasma is its tendency to cancel out the electric field. In the absence of a magnetic field, a charge imbalance creates an electric field, and plasma particles (mostly electrons because of their lighter mass) move to cancel this electric field. But because of the finite mass of electrons, they overshoot and cause an oscillation. This is called the plasma oscillation. This process can be described using the Poisson equation, the equation of motion, and the continuity equation. The one dimentional linearized equations can be expressed as

$$ikE = \frac{\rho}{\varepsilon_0}, \tag{2.1.1}$$

$$-im_{\mathrm{e}}\omega v_{\mathrm{e}} = -eE, \tag{2.1.2}$$

$$-i\omega n_e + ikn_{\mathrm{e}}v_{\mathrm{e}} = 0, \tag{2.1.3}$$

where ρ is the charge density, E is the electric field, ε_0 is the electric permittivity in a vacuum, m_{e}, n_{e}, v_{e} and $-e$ are mass, number density, velocity, and charge of the electron, and ω and k are the angular frequency and the wave number of the perturbation. The oscillation frequency is called the plasma frequency,

$$\omega_{\mathrm{pe}} = \sqrt{\frac{n_{\mathrm{e}}e^2}{\varepsilon_0 m_{\mathrm{e}}}}, \tag{2.1.4}$$

and is given approximately by

$$\omega_{\mathrm{pe}} = 90\sqrt{n_{20}}\,[\mathrm{GHz}]. \tag{2.1.5}$$

where n_{20} is the electron density n_{e} in units of $10^{20}\,\mathrm{m}^{-3}$.

A static electric field is shielded over a distance called the Debye length λ_{D}. This phenomenon is known as Debye shielding. The electrostatic potential around a fixed charge q in the absence of plasma is $\phi = q/(4\pi\varepsilon_0 r)$. In the presence of plasma, electrons and ions move freely under the influence of the electric field, and their number densities follow the Boltzmann distribution. The Poisson equation in spherical coordinates can be written as

$$\frac{1}{r^2}\frac{\mathrm{d}}{\mathrm{d}r}r^2\frac{\mathrm{d}\phi}{\mathrm{d}r} = \frac{n_0 e}{\varepsilon_0}\left[\exp\left(\frac{e\phi}{T_{\mathrm{e}}}\right) - \exp\left(\frac{-e\phi}{T_{\mathrm{i}}}\right)\right], \tag{2.1.6}$$

where ions are assumed to be singly charged, T_{s} is the temperature of species s (electron or ion), and since the temperatures are expressed in energy units (eV), the Boltzmann constant is 1. In the low potential limit $|e\phi|/T_{\mathrm{s}} \ll 1$,

$$\frac{1}{r^2}\frac{\mathrm{d}}{\mathrm{d}r}r^2\frac{\mathrm{d}\phi}{\mathrm{d}r} = \frac{n_0 e}{\varepsilon_0}\left(\frac{1}{T_{\mathrm{e}}} + \frac{1}{T_{\mathrm{i}}}\right)\phi, \tag{2.1.7}$$

where n_0 is the electron density at $r \to \infty$ (where $\phi \to 0$). The potential in the presence of plasma can be written as

$$\phi = \frac{e}{4\pi\varepsilon_0 r}\exp\left(-\frac{r}{\lambda_{\mathrm{D}}}\right), \tag{2.1.8}$$

where the Debye length is defined as

$$\frac{1}{\lambda_{\mathrm{D}}^2} = \frac{1}{\lambda_{\mathrm{D}e}^2} + \frac{1}{\lambda_{\mathrm{D}i}^2} = \frac{e^2 n_0}{\varepsilon_0 T_{\mathrm{e}}} + \frac{e^2 n_0}{\varepsilon_0 T_{\mathrm{i}}}. \tag{2.1.9}$$

Often the ion contribution can be neglected because it only makes an order of one correction when T_{i} is comparable to T_{e}. The electron Debye length is related to the plasma frequency by

$$\lambda_{\mathrm{De}} = \frac{v_{\mathrm{te}}}{\sqrt{2}\omega_{\mathrm{pe}}}, \tag{2.1.10}$$

where $v_{\mathrm{te}} = \sqrt{2T_{\mathrm{e}}/m_{\mathrm{e}}}$ is the electron thermal velocity. The Debye length is usually much shorter than the typical scale size of the plasma. Therefore, in the bulk of the plasma the charge imbalance $|n_{\mathrm{e}}–n_{\mathrm{i}}|/n_{\mathrm{e}}$ is negligibly small. This is called quasi-neutrality.

2.2 Cyclotron frequency and Larmor radius

The magnetic field is widely used to confine plasmas, because charged particles gyrate around magnetic field line. The spiral motion around the magnetic field line (assumed to be oriented in the direction along the z axis) is described by the equation of motion,

$$-im\omega\boldsymbol{v}_{\mathrm{s}} = q_{\mathrm{s}}\boldsymbol{v}_{\mathrm{s}} \times \boldsymbol{B}, \tag{2.2.1}$$

where $\boldsymbol{B}$ denotes the magnetic field vector. Using the rotating coordinates $x^{\pm} \equiv x \pm iy$ ($x+iy$ and $x-iy$ represent counterclockwise and clockwise rotation), $\boldsymbol{v}_{\mathrm{s}}^{\pm} \times \boldsymbol{B}$ becomes $\mp i v_{\mathrm{s}}^{+} B$, where v_{s}^{+} corresponds to the velocity of counterclockwise rotation. The gyration frequency (also called the cyclotron frequency) is given by

$$\omega = \frac{q_{\mathrm{s}} B}{m_{\mathrm{s}}} \equiv \Omega_{\mathrm{s}}. \tag{2.2.2}$$

The radius of gyration is called the Larmor radius and is defined as

$$\rho_{\mathrm{s}} = \frac{v_{\mathrm{s}}^{+}}{\Omega_{\mathrm{s}}} = \frac{m_{\mathrm{s}} v_{\mathrm{s}}^{+}}{q_{\mathrm{s}} B}. \tag{2.2.3}$$

The cyclotron frequencies of electrons and hydrogen ions are given approximately as

$$\Omega_{\mathrm{e}} = -28B\,[\mathrm{GHz}], \tag{2.2.4}$$

$$\Omega_{\mathrm{H}} = 15B\,[\mathrm{MHz}]. \tag{2.2.5}$$

2.3 Tokamak equilibrium

The tokamak configuration consists of nested toroidal flux surfaces. The flux surface is a surface of constant flux ψ. The magnetic field line lies on the flux surface, and never crosses it. Consequently, the gradient of ψ is perpendicular to the flux surface,

$$\nabla\psi \cdot \boldsymbol{B} = 0. \tag{2.3.1}$$

In a toroidally symmetric configuration ($\partial/\partial\phi = 0$) such as the tokamak,

$$\psi(r, z) = r A_{\phi}, \tag{2.3.2}$$

where A_{ϕ} is the toroidal component of the vector potential $\boldsymbol{A}$. In a steady state, the one-fluid equation of motion for the plasma is

$$\boldsymbol{j} \times \boldsymbol{B} = \nabla p. \tag{2.3.3}$$

The following relations also hold:

$$\boldsymbol{B} \cdot \nabla p = 0, \tag{2.3.4}$$

$$\boldsymbol{j} \cdot \nabla p = 0. \tag{2.3.5}$$

From Eqs. (2.3.2) and (2.3.4)

$$-\frac{\partial\psi}{\partial z}\frac{\partial p}{\partial r} + \frac{\partial\psi}{\partial r}\frac{\partial p}{\partial z} = 0. \tag{2.3.6}$$

This means that the plasma pressure is a function of ψ. A similar equation is obtained for RB_ϕ and is obtained from Eqs. (2.3.2) and (2.3.5) as

$$-\frac{\partial\psi}{\partial z}\frac{\partial(RB_\phi)}{\partial r}+\frac{\partial\psi}{\partial r}\frac{\partial(RB_\phi)}{\partial z}=0. \tag{2.3.7}$$

This means that the parameter $F = RB_\phi$ is also a function of ψ. Finally, from the radial component of Eq. (2.3.1), the following equation for ψ is obtained,

$$\Delta^*\psi=-\mu_0R^2\frac{\mathrm{d}p}{\mathrm{d}\psi}-\frac{1}{2}\frac{\mathrm{d}F^2}{\mathrm{d}\psi}, \tag{2.3.8}$$

where μ_0 is the magnetic permeability, and the operator Δ^* is,

$$\Delta^*\psi\equiv R^2\nabla\cdot\left(\frac{1}{R^2}\nabla\psi\right)=R\frac{\partial}{\partial R}\left(\frac{1}{R}\frac{\partial\psi}{\partial R}\right)+\frac{\partial^2\psi}{\partial Z^2}. \tag{2.3.9}$$

This equation is called the Grad–Shafranov equation. The magnetic field and the current density can be expressed in terms of ψ

$$\boldsymbol{B}=\frac{1}{R}\nabla\psi\times\hat{e}_\phi+\frac{F}{R}\hat{e}_\phi, \tag{2.3.10}$$

$$\mu_0\boldsymbol{j}=\frac{1}{R}\frac{\mathrm{d}F}{\mathrm{d}\psi}\nabla\psi\times\hat{e}_\phi-\frac{1}{R}\Delta^*\psi\hat{e}_\phi, \tag{2.3.11}$$

where $\hat{e}_\phi$ is the unit vector in the toroidal direction.

2.4 Cold plasma dispersion relation

The wave equation is derived from the following two Maxwell equations:

$$\nabla\times\boldsymbol{E} = -\frac{\partial\boldsymbol{B}}{\partial t}, \tag{2.4.1}$$

$$\nabla\times\boldsymbol{B} = \mu_0\boldsymbol{j}+\mu_0\varepsilon_0\frac{\partial\boldsymbol{E}}{\partial t}. \tag{2.4.2}$$

In the presence of a plasma, considering a single wave number and a single frequency of perturbation, the plasma current perturbation can be included in the electric field term in Eq. (2.4.2) using the susceptibility tensor $\overleftrightarrow{\chi}$ as

$$\boldsymbol{k}\times\boldsymbol{B} = -i\omega\mu_0\varepsilon_0\left(1+\overleftrightarrow{\chi}\right)\boldsymbol{E}, \tag{2.4.3}$$

$$\boldsymbol{j} = -i\omega\varepsilon_0\overleftrightarrow{\chi}\boldsymbol{E}. \tag{2.4.4}$$

Therefore, $\overleftrightarrow{\chi}$ describes the plasma current driven by the oscillating electric field. The plasma current is derived by solving the equations of motion,

$$m_{\rm s} n_{\rm s} \left[\frac{\partial \boldsymbol{v}_{\rm s}}{\partial t} + (\boldsymbol{v}_{\rm s} \cdot \nabla) \boldsymbol{v}_{\rm s} \right] = q_{\rm s} n_{\rm s} \left(\boldsymbol{E} + \boldsymbol{v}_{\rm s} \times \boldsymbol{B} \right) - \nabla \cdot \overleftrightarrow{\Psi}_{\rm s}, \tag{2.4.5}$$

where $\overleftrightarrow{\Psi}_{\rm s}$ is the stress tensor. In the cold plasma approximation, the stress tensor term can be neglected. The linearized equation becomes

$$-i m_{\rm s} \omega n_{\rm s} \boldsymbol{v}_{\rm s} = q_{\rm s} n_{\rm s} \left(\boldsymbol{E} + \boldsymbol{v}_{\rm s} \times \boldsymbol{B} \right). \tag{2.4.6}$$

Considering that

$$\begin{aligned}
\overleftrightarrow{\chi_s} \boldsymbol{E} = \frac{\boldsymbol{j}_{\rm s}}{-i\omega\varepsilon_0} &= -\frac{\omega_{\rm ps}^2}{\omega^2} \left(\boldsymbol{E} + \frac{\boldsymbol{j}_{\rm s}}{q_{\rm s} n_{\rm s}} \times \boldsymbol{B} \right) && (2.4.7) \\
&= -\frac{\omega_{\rm ps}^2}{\omega^2} \left(\boldsymbol{E} - i\frac{\omega \Omega_{\rm s}}{\omega_{\rm ps}^2} (\overleftrightarrow{\chi_s} \boldsymbol{E}) \times \frac{\boldsymbol{B}}{B} \right) && (2.4.8) \\
&= -\frac{\omega_{\rm ps}^2}{\omega^2} \boldsymbol{E} + i\frac{\Omega_{\rm s}}{\omega} (\overleftrightarrow{\chi_s} \boldsymbol{E}) \times \frac{\boldsymbol{B}}{B}, && (2.4.9)
\end{aligned}$$

taking $\boldsymbol{B} \parallel \hat{\boldsymbol{z}}$ and using the coordinate system $(x^+, x^-, z) = (x + iy, x - iy, z)$, the cross product can be simplified and moved to the left hand side,

$$\begin{pmatrix} \frac{\omega+\Omega_{\rm s}}{\omega} & 0 & 0 \\ 0 & \frac{\omega-\Omega_{\rm s}}{\omega} & 0 \\ 0 & 0 & 1 \end{pmatrix} \overleftrightarrow{\chi_s} \boldsymbol{E} = -\frac{\omega_{\rm ps}^2}{\omega^2} \boldsymbol{E}. \tag{2.4.10}$$

Therefore,

$$\overleftrightarrow{\chi_s} = \begin{pmatrix} -\frac{\omega_{\rm ps}^2}{\omega(\omega+\Omega_{\rm s})} & 0 & 0 \\ 0 & -\frac{\omega_{\rm ps}^2}{\omega(\omega-\Omega_{\rm s})} & 0 \\ 0 & 0 & -\frac{\omega_{\rm ps}^2}{\omega^2} \end{pmatrix}. \tag{2.4.11}$$

The total susceptibility tensor $\overleftrightarrow{\chi}$ is the sum of the contributions of all charged particle species ($\overleftrightarrow{\chi} = \sum_s \overleftrightarrow{\chi_s}$). Finally, the dielectric tensor is written as

$$\begin{aligned}
\overleftrightarrow{\varepsilon} &= \begin{pmatrix} R & 0 & 0 \\ 0 & L & 0 \\ 0 & 0 & P \end{pmatrix}, && (2.4.12) \\
& && (2.4.13)
\end{aligned}$$

where

$$R = 1 - \sum_s \frac{\omega_{\rm ps}^2}{\omega(\omega + \Omega_{\rm s})}, \tag{2.4.14}$$

$$L = 1 - \sum_s \frac{\omega_{\rm ps}^2}{\omega(\omega - \Omega_{\rm s})}, \tag{2.4.15}$$

$$P = 1 - \sum_s \frac{\omega_{\rm ps}^2}{\omega^2}. \tag{2.4.16}$$

In the Cartesian coordinate system,

$$\overleftrightarrow{\varepsilon} = \begin{pmatrix} S & -iD & 0 \\ iD & S & 0 \\ 0 & 0 & P \end{pmatrix}, \tag{2.4.17}$$

where

$$S = \frac{R+L}{2} \tag{2.4.18}$$

$$D = \frac{R-L}{2}. \tag{2.4.19}$$

The wave equation can be written as

$$\boldsymbol{n} \times \boldsymbol{n} \times \boldsymbol{E} + \overleftrightarrow{\varepsilon} \boldsymbol{E} = 0 \tag{2.4.20}$$

or

$$\left[n_{\rm i} n_{\rm j} - n^2 \delta_{\rm ij} + \varepsilon_{\rm ij}\right] \cdot E_{\rm i} = 0, \tag{2.4.21}$$

where $\boldsymbol{n} = c\boldsymbol{k}/\omega$ is the vector refractive index. Assuming that the wavevector is tilted from the z axis by angle θ, $\boldsymbol{n} = (n\sin\theta, 0, n\cos\theta)$ and the dispersion relation is expressed as

$$\det \begin{pmatrix} S - n^2\cos^2\theta & -iD & n^2\cos\theta\sin\theta \\ iD & S - n^2 & 0 \\ n^2\cos\theta\sin\theta & 0 & P - n^2\sin^2\theta \end{pmatrix} = 0. \tag{2.4.22}$$

Finally, the dispersion relation can be written as

$$An^4 - Bn^2 + C = 0, \tag{2.4.23}$$

where

$$A = S\sin^2\theta + P\cos^2\theta, \tag{2.4.24}$$

$$B = RL\sin^2\theta + PS(1 + \cos^2\theta), \tag{2.4.25}$$

$$C = PRL. \tag{2.4.26}$$

2.5 Electrostatic approximation

The electrostatic wave has no oscillating magnetic field, so $\boldsymbol{k} \times \boldsymbol{E} = 0$ (*i.e.*, $\boldsymbol{k} \parallel \boldsymbol{E}$). In this case the cold plasma dispersion relation is simplified as

$$\boldsymbol{k} \cdot \boldsymbol{D} = \boldsymbol{k} \cdot \overleftrightarrow{\varepsilon} \cdot \boldsymbol{k}\phi = 0 \tag{2.5.1}$$

Using the cold plasma dielectric tensor Eq. (2.4.17), the dispersion relation is reduced to

$$Sk_\perp^2 + Pk_\parallel^2 = 0. \tag{2.5.2}$$

Separating the electric field into the components parallel and perpendicular to the wave number vector ($\boldsymbol{E} = \boldsymbol{E}_\parallel + \boldsymbol{E}_\perp$), Eq. (2.4.20) can be rewritten as

$$(n^2 I - \overleftrightarrow{\varepsilon}) \cdot \boldsymbol{E}_\perp = \overleftrightarrow{\varepsilon} \cdot \boldsymbol{E}_\parallel. \tag{2.5.3}$$

For the electrostatic wave, the electric field is mostly oriented along the wave number vector ($E_\parallel \gg E_\perp$). Therefore, a sufficient condition for the electrostatic wave is

$$n^2 \gg |\varepsilon_{\mathrm{ij}}|. \tag{2.5.4}$$

2.6 Accessibility and density limits for LHW

The cold plasma dispersion relation derived in Eq. (2.4.23) can be rewritten in the form of quadratic equation for n_x^2 (n_x is the component of the refractive index in the direction of plasma inhomogeneity, perpendicular to the magnetic field) as

$$an_x^4 - bn_x^2 + c = 0, \tag{2.6.1}$$

where

$$a = S, \tag{2.6.2}$$
$$b = RL + PS - Pn_\parallel^2 - Sn_\parallel^2, \tag{2.6.3}$$
$$c = P\left(RL - 2Sn_\parallel^2 + n_\parallel^4\right), \tag{2.6.4}$$

and $N_\parallel$ is the refractive index component parallel to the magnetic field [25]. In the low density limit ($|D| \ll 1, S \simeq 1$, and $RL \simeq 1$), the two roots can be factorized as

$$\left[n_x^2 - P\left(1 - n_\parallel^2\right)\right]\left[n_x^2 - \left(1 - n_\parallel^2\right)\right] = 0. \tag{2.6.5}$$

Since $N_\parallel$ cannot be smaller than 1 for the LHW, the second root $[n_x^2 = (1 - n_\parallel^2) < 0]$ is evanescent, while the first root $[n_x^2 = P(1 - n_\parallel^2)]$ is propagating when the electron

density is above the cutoff density ($P < 0$, or $\omega_{\rm pe} > \omega$). In the high density limit where $|P| \gg 1$ and $|P| \gg |S|$,

$$a > 0 \quad \rightarrow \quad S > 0, \tag{2.6.6}$$

$$b > 0 \quad \rightarrow \quad n_{\parallel}^2 > \left|\frac{RL}{P}\right| + |S|, \tag{2.6.7}$$

$$b^2 - 4ac > 0 \quad \rightarrow \quad n_{\parallel}^2 > \left(\sqrt{S} + \sqrt{\left|\frac{D^2}{P}\right|}\right)^2 . \tag{2.6.8}$$

The second condition is less strict than the third condition. The third condition can give multiple roots at a certain density. This is the case where the two roots coalesce, and the slow wave (LHW) can convert to the fast wave (FW) or vise versa. This is called mode conversion. When the LHW (electrostatic wave) is converted to the FW (electromagnetic wave), Landau damping becomes very weak. In the present case, the density region where the LHW can propagate is bounded by the cutoff density (lower limit) and the mode conversion density (upper limit). The upper limit depends on $N_{\parallel}$ as indicated in Fig. 2.1.

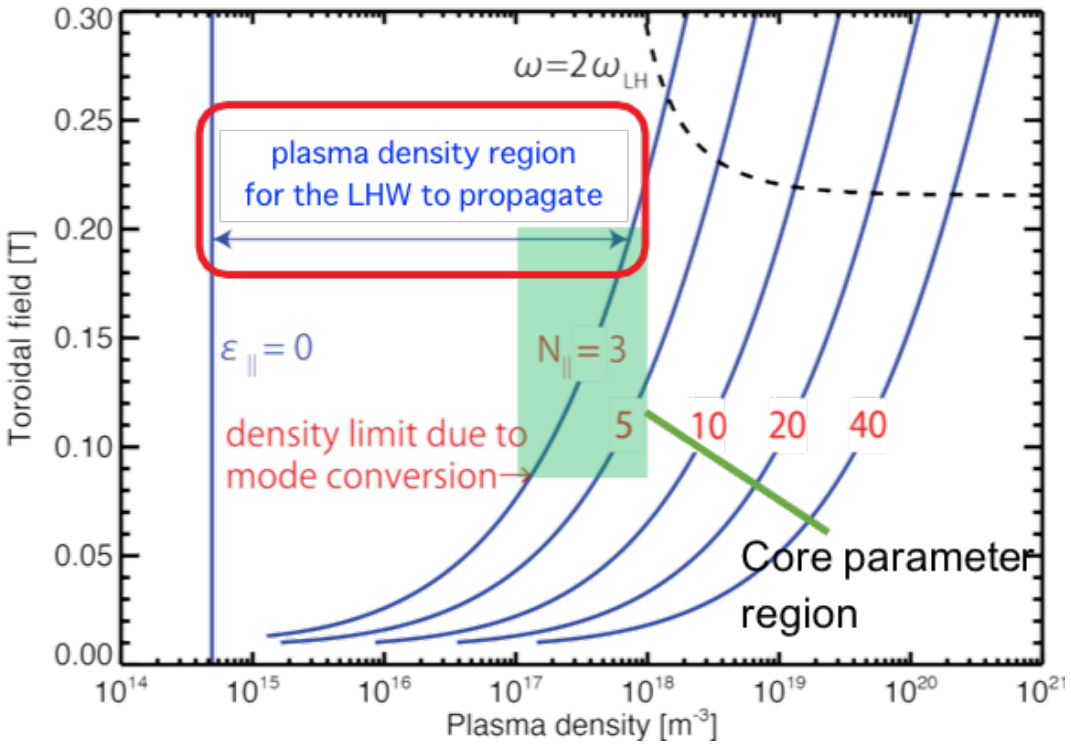

Figure 2.1: Density region where the LHW can propagate.

2.7 Ray tracing

Waves can be considered to propagate as a wave packet

$$\boldsymbol{E}(\boldsymbol{r},t) \simeq \int d\boldsymbol{k}\boldsymbol{E}(\boldsymbol{k}) \exp\left[i\boldsymbol{k}\cdot\boldsymbol{r} - i\omega(\boldsymbol{k})t\right] \tag{2.7.1}$$

through a weakly inhomogeneous plasma. Assuming that the wave number spectrum is localized around a peak at $\boldsymbol{k} = \boldsymbol{k}_0$, and when the primary term and the first order term of the Taylor expansion of ω are taken into account $[\omega(\boldsymbol{k}) \simeq \omega(\boldsymbol{k}_0) + \mathrm{d}\omega/\mathrm{d}\boldsymbol{k}\cdot(\boldsymbol{k}-\boldsymbol{k}_0)]$,

$$\begin{aligned}
\boldsymbol{E}(\boldsymbol{r},t) &\simeq \exp\left[i\boldsymbol{k}_0\cdot\boldsymbol{r} - i\omega(\boldsymbol{k}_0)t\right] \int \mathrm{d}\boldsymbol{k}\boldsymbol{E}(\boldsymbol{k}) \exp i(\boldsymbol{k}-\boldsymbol{k}_0)\cdot\left(\boldsymbol{r} - \frac{\mathrm{d}\omega}{\mathrm{d}\boldsymbol{k}}t\right) && (2.7.2)\\
&= \exp\left[i\boldsymbol{k}_0\cdot\boldsymbol{r} - i\omega(\boldsymbol{k}_0)t\right] I\left(\boldsymbol{r} - \frac{\mathrm{d}\omega}{\mathrm{d}\boldsymbol{k}}t\right). && (2.7.3)
\end{aligned}$$

The first factor (exp[...]) describes the primary oscillation and the second factor $[I(...)]$ describes the envelope traveling at the speed $\mathrm{d}\omega/\mathrm{d}\boldsymbol{k}$, which is the group velocity. The dispersion relation is written in the form

$$D(\boldsymbol{r},\boldsymbol{k},\omega,t) = 0. \tag{2.7.4}$$

Using D as the Hamiltonian, the following canonical equations are obtained

$$\begin{aligned}
\frac{\mathrm{d}\boldsymbol{r}}{\mathrm{d}\tau} &= \frac{\partial D}{\partial \boldsymbol{k}}, && (2.7.5)\\
\frac{\mathrm{d}\boldsymbol{k}}{\mathrm{d}\tau} &= -\frac{\partial D}{\partial \boldsymbol{r}}, && (2.7.6)\\
\frac{\mathrm{d}\omega}{\mathrm{d}\tau} &= \frac{\partial D}{\partial t}, && (2.7.7)\\
\frac{\mathrm{d}t}{\mathrm{d}\tau} &= -\frac{\partial D}{\partial \omega}, && (2.7.8)
\end{aligned}$$

where τ is a parameter indicating the distance along the ray trajectory.

2.8 Landau damping

A crucially important physical phenomenon for the present research is the wave-particle interaction called Landau damping [26,27]. The physical mechanism of Landau damping is described in this section. Consider a one-dimentional charged particle motion under the influence of the oscillating electric field given by $E\cos(kz - \omega t)$,

$$m\frac{\mathrm{d}v}{\mathrm{d}t} = qE\cos(kz - \omega t), \tag{2.8.1}$$

Taking the zeroth order particle motion to be $z(t) = v_0 t + z_0$, the first order perturbed motion is given as,

$$m\frac{\mathrm{d}v_1}{\mathrm{d}t} = qE\cos\left(kz_0 + kv_0 t - \omega t\right), \tag{2.8.2}$$

$$v_1 = \frac{qE}{m}\frac{\sin\left(kz_0 + kv_0 t - \omega t\right) - \sin\left(kz_0\right)}{kv_0 - \omega}. \tag{2.8.3}$$

Taking the average over the initial position, the energy gain per particle is

$$\left\langle \frac{\mathrm{d}}{\mathrm{d}t}\frac{mv^2}{2} \right\rangle_{z_0} = \frac{q^2E^2}{2m}\left[-\frac{\omega\sin(\alpha t)}{\alpha^2} + t\cos(\alpha t) + \frac{\omega t\cos(\alpha t)}{\alpha}\right], \tag{2.8.4}$$

where $\alpha = kv_0 - \omega$. Taking the average over the distribution of initial velocities $f(v_0)$ annihilates the second and third terms, and using Taylor expansion of $f(v_0)$ in the vicinity of the wave phase velocity $v_0 = \omega/k$ gives

$$\left\langle \frac{\mathrm{d}}{\mathrm{d}t}\frac{mv^2}{2} \right\rangle_{z_0,v_0} \simeq -\frac{\pi\omega q^2E^2}{2mk|k|}\left[\frac{\mathrm{d}f\left(v_0\right)}{\mathrm{d}v_0}\right]_{v_0=\frac{\omega}{k}} \tag{2.8.5}$$

for the rate of wave energy absorption. This is called Landau damping.

2.9 Quasi-linear diffusion

Quasi-linear diffusion is a diffusion in velocity space induced by RF waves under the framework of weak turbulence theory [26], and drives the velocity distribution function away from the Maxwellian distribution. The first order motion under the influence of a weak electrostatic fluctuation $E_1 = E\cos(kz - \omega t)$ is given by Eq. (2.8.3). Taking the average of the square of the perturbed velocity over initial position, $(\Delta v)^2 = \langle v_1^2 \rangle$, the diffusion coefficient is derived as

$$D_v = \frac{(\Delta v)^2}{2t} = \frac{\pi}{2}\left(\frac{qE}{m}\right)^2 \delta(\omega - kv) \tag{2.9.1}$$

The first-order Vlasov equation is written as,

$$\frac{\partial f_1}{\partial t} + v\frac{\partial f_1}{\partial z} + \frac{qE_1}{m}\frac{\partial f_0}{\partial v} = 0. \tag{2.9.2}$$

Using Fourier and Laplace analyses in space and time, respectively,

$$f_1\left(\omega_k, k\right) = -\frac{iq}{m}\frac{1}{\omega_k - kv}E\left(\omega_k, k\right)\frac{\partial f_0}{\partial v} + \frac{ig(v,k)}{\omega_k - kv}, \tag{2.9.3}$$

where $g(v,z) \equiv f_1(v,z,t=0)$ is the initial disturbance and $g(v,k) \equiv \int_{-\infty}^{\infty} dz g(v,z) e^{-ikz}$. The zeroth order distribution function is deformed gradually due to the feedback from the first order disturbance,

$$\frac{\partial f_0(v,t)}{\partial t} \simeq -\frac{q}{m}\left\langle E_1 \frac{\partial f_1}{\partial v} \right\rangle. \tag{2.9.4}$$

Eventually, the deformation of the velocity distribution function is evaluated by solving the following equation,

$$\frac{\partial f_0(v,t)}{\partial t} = \frac{2\pi i q^2}{m^2 L^2} \sum_{k\neq 0} |E_k(t)|^2 \frac{\partial}{\partial v} \frac{1}{\omega_k - kv} \frac{\partial f_0(v,t)}{\partial v}, \tag{2.9.5}$$

where L is the scale of box normalization for Fourier transform,

$$E_k(t) = \frac{1}{\sqrt{2\pi}} \int_{-L/2}^{L/2} dz e^{-ikz} E(z,t) \tag{2.9.6}$$

$$E(z,t) = \frac{\sqrt{2\pi}}{L} \sum_k e^{ikz} E_k(t). \tag{2.9.7}$$

2.10 Fokker-Planck equation

When simulating plasma phenomena, one approach is to calculate the behavior of an interacting multi-body system, taking all charged particles into account, but it is impractical to trace motions of all particles. Another approach is to describe the plasma as a magnetized fluid, under the framework of magnetohydrodynamics (MHD). In this case, the plasma motion is described by the mass-averaged particle velocity. However, this framework cannot describe phenomena associated with the wave-particle interaction or non-Maxwellian particle velocity distribution function. In order to describe these phenomena, a Boltzmann equation which describes the evolution of the velocity distribution function is used. According to Fisch and Karney [28], the velocity distribution function is flattened by quasi-linear diffusion in the vicinity of the component of the phase velocity of the wave parallel to the magnetic field. When the velocity space diffusion coefficient is D_{QL}, a Boltzmann equation can be represented in the form of a Fokker-Planck equation as

$$\frac{\partial f}{\partial t} + \boldsymbol{v}\cdot\nabla f + \frac{\boldsymbol{F}}{m}\cdot\nabla_{\mathrm{v}} f = \frac{\partial}{\partial v_z}\left(D_{\mathrm{QL}}\frac{\partial f}{\partial v_z}\right) + \left(\frac{\delta f}{\delta t}\right)_{\mathrm{coll.}}, \tag{2.10.1}$$

where the collision term is

$$\left(\frac{\delta f}{\delta t}\right)_{\mathrm{coll.}} = -\sum_{\mathrm{i,e}}\left(\frac{1}{v^2}\frac{\partial}{\partial v}(v^2 J_{\mathrm{v}}) + \frac{1}{v\sin\theta}\frac{\partial}{\partial\theta}(\sin\theta J_\theta)\right), \tag{2.10.2}$$

$$J_{\mathrm{v}} = -D_{\parallel}\frac{\partial f}{\partial v} + Af, \quad J_\theta = -D_\perp \frac{1}{v}\frac{\partial f}{\partial\theta}, \tag{2.10.3}$$

where $D_{\parallel}$ and $D_{\perp}$ are the parallel and perpendicular components of the diffusion tensor in velocity space, and A is the coefficient of dynamic friction [29].

The effect of Landau damping is represented by the diffusion term D_v of Eq. 2.9.1, which can be substituted into D_{QL}, resulting in the flattening of the electron velocity distribution function. However, as can be seen from the delta function in the diffusion coefficient, the electron velocity distribution can only be flattened locally at the wave phase velocity. Only a small deformation of the Maxwellian distribution function can be expected. In order to flatten the electron velocity distribution over a substantial range, it is necessary for the LHW to have a broad wave number spectrum (broad phase velocity range) in the plasma core corresponding to the electron velocity range to be flattened (Fig. 2.2). Eventually, a tail of the electron velocity distribution is formed extended from a certain point of the Maxwellian distribution function, as shown in Fig. 2.2. This is called the quasi-linear plateau. The plasma current is generated due to the asymmetry of the velocity distribution function. When the wave number spectrum of the LHW in the plasma has a certain width, the generated current is roughly proportional to the following expression:

$$n_{\mathrm{e}} \int_{-\infty}^{\infty} v_{\parallel} f(v_{\parallel}) dv_{\parallel} \propto \frac{n_{\mathrm{e}}}{N_{\parallel,\mathrm{min}}^2} \exp\left[-\left(\frac{c}{v_{\mathrm{Te}} N_{\parallel,\mathrm{max}}} \right)^2 \right], \tag{2.10.4}$$

where n_{e} is the electron density, v_{Te} is the electron thermal velocity, and $N_{\parallel,\mathrm{max}}$ ($N_{\parallel,\mathrm{min}}$) is the maximum (minimum) parallel refractive index of the LHW existing in the plasma core. As can be seen from Fig. 2.2 and Eq. 2.10.4, the minimum wave number should be smaller, and the maximum wave number should be larger to maximize the driven plasma current, and sufficient electron density and electron temperature should also be maintained for effective current generation.

To summarize the relationship between the wave number spectrum of the LHW and the velocity distribution function formed by quasi-linear diffusion, it is sufficient to focus on the following three points:

- The largest wave number of the LHW propagating in the plasma (larger wave number extends the electron velocity distribution function from the higher part of the Maxwellian distribution function, so the number of fast electrons becomes larger).
- The smallest wave number of the LHW propagating in the plasma (smaller wave number produces faster electrons so the average contribution of fast electrons to the plasma current becomes larger).
- Whether the LHW wave number spectrum covers the wave number range continuously between the largest and smallest wave numbers (if there is a gap in the wave number range of the propagating LHW, fast electrons cannot be accelerated beyond the velocity corresponding to the phase velocity gap).

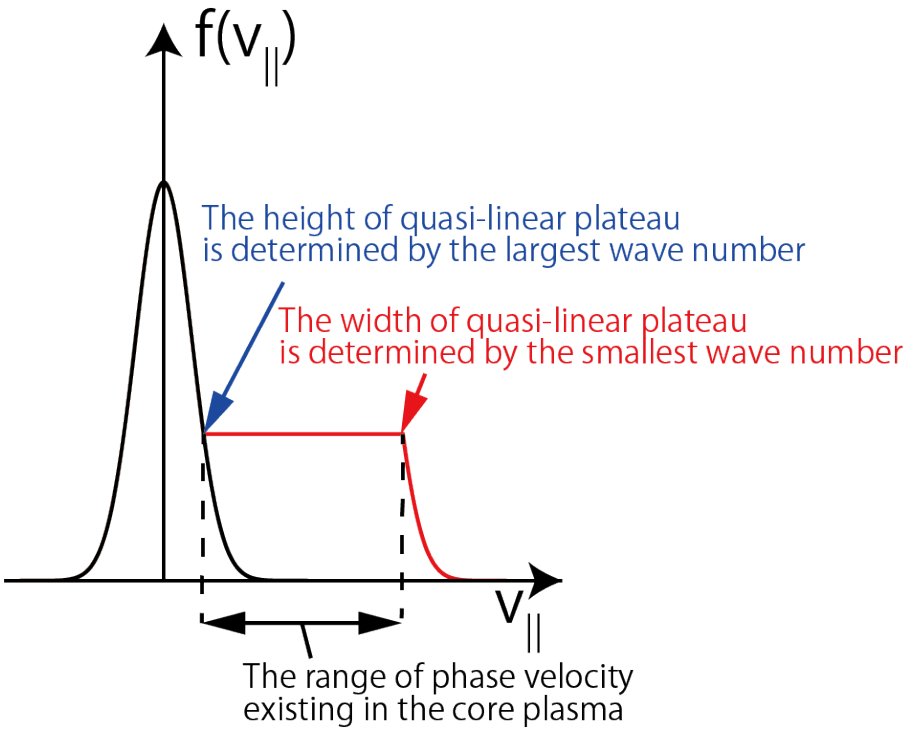

Figure 2.2: Schematic of the extension of the electron velocity distribution function (quasi-linear plateau) formed by Laudau damping.

Chapter 3

Experimental Setup

3.1 TST-2 spherical tokamak

The TST-2 (Tokyo Spherical Tokamak - 2) apparatus (Fig. 3.1), originally constructed in 1999 on the Hongo Campus of the University of Tokyo, is now installed on the Kashiwa Campus. Its major radius is $R_0 = 0.36\,\mathrm{m}$, minor radius is $a = 0.23\,\mathrm{m}$, and the aspect ratio is $A = R_0/a = 1.6$. On TST-2, the main research emphasis is on plasma formation and plasma current ramp-up of a spherical tokamak plasma. The two methods of plasma start-up and plasma current ramp-up are inductive start-up using the central solenoid (CS) and non-inductive start-up using the LHW. In both cases, plasma pre-ionization by electron cyclotron heating (ECH) is normally used (maximum of 5 kW of microwave power at 2.45 GHz for about 10 ms). In the inductive start-up experiment, the maximum current of over 120 kA can be achieved in approximately 20 ms after the start of the CS current swing, and the total discharge duration is about 45 ms. The discharge duration and the plasma current are limited by the CS power supply. In the non-inductive start-up experiment, it is possible to extend the discharge duration to 100 ms. The maximum plasma current achieved in non-inductive start-up is 27 kA (about a quarter of a typical inductive start-up discharge). The discharge duration is presently limited by the capacitor bank power supply for the toroidal field coils. For exciting the LHW, two traveling wave antennas are presently in use, the top-launch antenna and the outboard-launch antenna [30]. Both antennas are designed to excite the LHW (with the RF electric field polarized in the toroidal direction) at 200 MHz. Presently, it is possible to inject up to 100 kW for the top-launch antenna and up to 200 kW for the outboard-launch antenna.

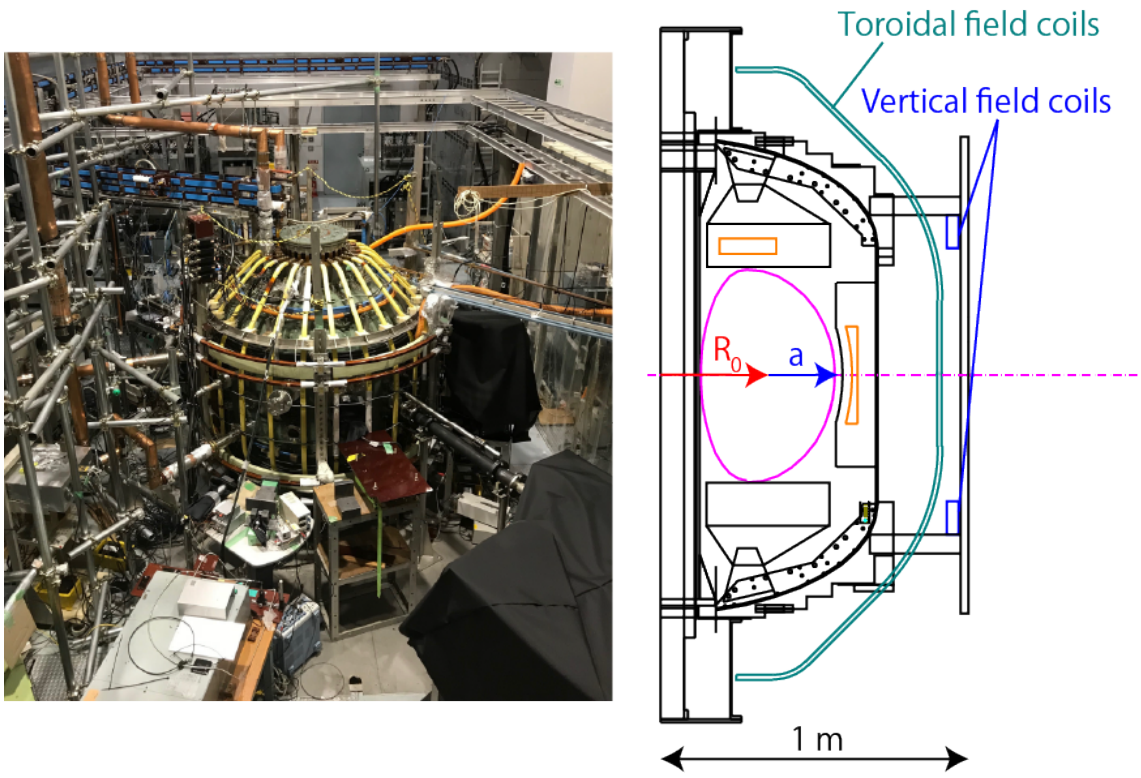

Figure 3.1: Photograph of TST-2 (left) and cross section of TST-2 (right) [31].

3.2 RF system for LHW experiment

The high power 200 MHz RF system for LHW experiments on TST-2 consists of four amplifier chains with up to 100 kW output each. Just after installing the top-launch antenna, the RF system was configured as shown in the upper half of Fig. 3.2. The signal generator generates a CW 200 MHz sine wave with a power of +15 dBm. The amplitude of this 200 MHz signal is modulated by a pulse waveform generated by the pulse modulator, and the semiconductor amplifier amplifies the modulated RF pulse to a power level of 1 kW. The RF pulse is amplified to about 20 kW by the exciter vacuum tube amplifier. This power is divided into four ways with 5 kW RF pulses by the power splitter. Each of the four RF pulses is adjusted in amplitude and phase, amplified by the intermediate vacuum tube amplifier (up to maximum power of 40 kW), and finally amplified up to 100 kW level by the final vacuum tube amplifier. For the outboard-launch antenna, outputs of the two final amplifiers are combined by the ring coupler. A total RF power of up to 200 kW can be delivered to the outboard antenna. The installation of an additional top-launch antenna necessitated independent control of the RF power delivered to the two antennas. The RF system was reconfigured to

two independent systems by adding a second driver chain consisting of an RF signal generator, a pulse modulator, and a solid state amplifier. However, since the maximum output power of the solid-state amplifier was only 150 W, an additional intermediate vacuum tube amplifier was connected in series to achieve 100 kW RF power output from the final vacuum tube amplifier (lower half of Fig. 3.2).

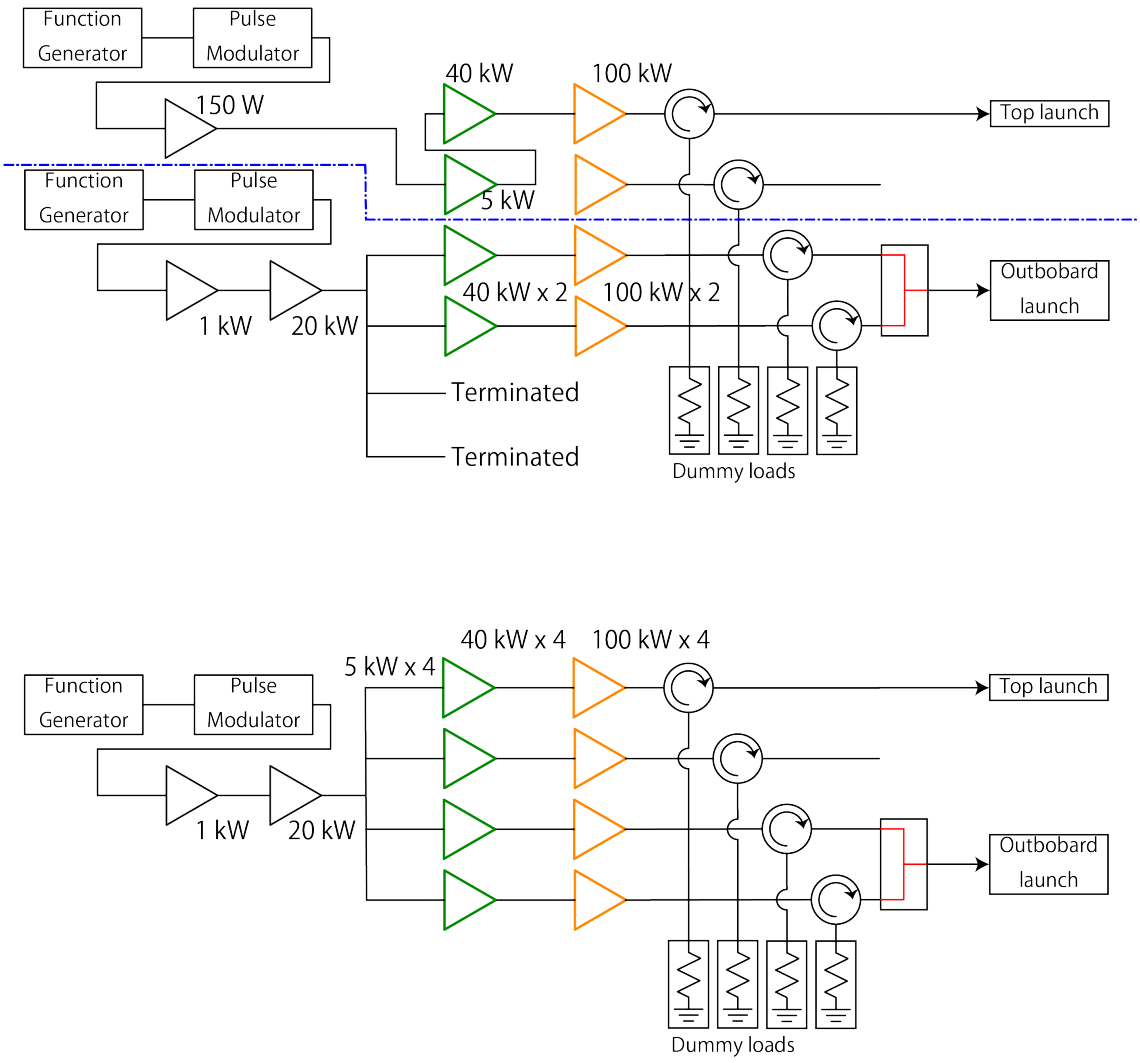

Figure 3.2: The original RF system (top) and the modified RF system (bottom). The modified RF system enables independent control for two separate LHW launchers.

3.3 Capacitively-coupled combline antenna

The CCC antennas were developed in collaboration with General Atomics [32] specifically for the current ramp-up experiment on TST-2. The original (inductively-coupled) combline antenna [33] is an array of L-C resonant circuits which couple to each other by mutual inductance. When the inductor is oriented vertically and the resonant circuits are arrayed in the toroidal direction, the antenna excites the FW. It works like the combline band-pass filter, and the phase shift between adjacent elements defines the toroidal wavenumber of the excited FW. In contrast, in the CCC antenna, L-C resonant circuits coupled to each other by mutual capacitance. When the capacitive element is exposed to the plasma and the resonant circuits are arrayed in the toroidal direction, the antenna excites the LHW.

In conventional tokamaks, waveguide array antennas are widely used for exciting the LHW [34, 35]. These antennas are composed of many waveguides arrayed in both toroidal and poloidal directions with the long dimension of the waveguide in the vertical direction. The RF (microwave) power is transmitted in the TE_{10} mode to each waveguide with specific phase differences made by power splitter or independent control in order to define the wavenumber. In such antennas, it is necessary to feed RF power to each waveguide with a controlled phase distribution, so the power feeding system becomes complicated. In contrast, since the electric field is automatically excited after proper pre-tuning of the CCC antenna, only a single coaxial transmission line is required to feed RF power to the first resonant circuit. The CCC antennas are in use on TST-2 (Fig. 3.3). The outboard-launch antenna is located on the outboard side ($R = 621\,\mathrm{mm}$, $Z = -145 \sim 145\,\mathrm{mm}$) and the top-launch antenna is located on the top side ($R = 190 \sim 375\,\mathrm{mm}$, $Z = 336, 386$, or $436\,\mathrm{mm}$), where R is the major radius and Z is the height measured from the midplane. In both antennas, the antenna elements (L-C resonant circuits) are arrayed in the toroidal direction and excite the LHW with a well-defined wavenumber in the toroidal direction. Both antennas are tuned at 200 MHz and the excited LHW has a toroidal wavenumber spectrum peaked around $N_\parallel \sim -5$ (at $R = 283\,\mathrm{mm}$ for the top antenna), and the HWHM is about $\Delta N_\parallel = 2$ In addition to the antenna elements, metal plates called limiters are installed on both ends of the antenna. The limiters are required to control the plasma density in front of the antenna for proper wave excitation. The LHW propagates in the plasma provided the plasma density exceeds the cutoff density ($5 \times 10^{14}\,\mathrm{m}^{-3}$ for 200 MHz) (Fig. 3.4). In order to excite a sharp wavenumber spectrum with good directivity, it is necessary to secure a low-density region (below the cutoff density) in front of the antenna elements. The location of the front surfaces of the limiters were adjusted to provide a thick enough evanescent region (with the plasma density lower than the cutoff density) in front of the antenna elements.

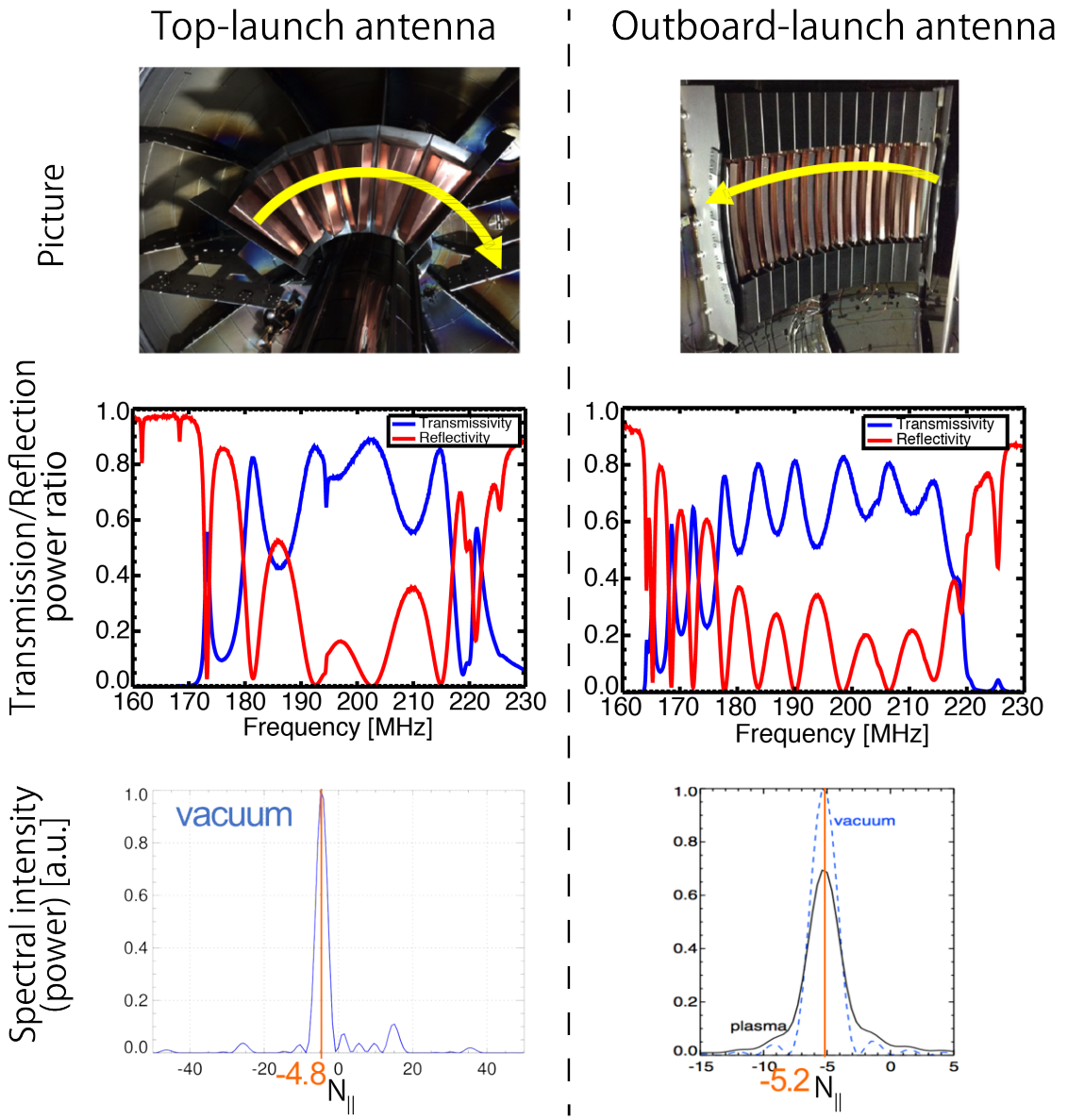

Figure 3.3: Photographs, frequency characteristics (power reflectivity and transmission), and power spectra of the top-launch CCC antenna (left) and the outboard-launch CCC antenna (right). The antenna frequency characteristic is measured including feedthroughs after installation, and the power spectrum of the outboard-launch antenna is quoted from Ref. [22].

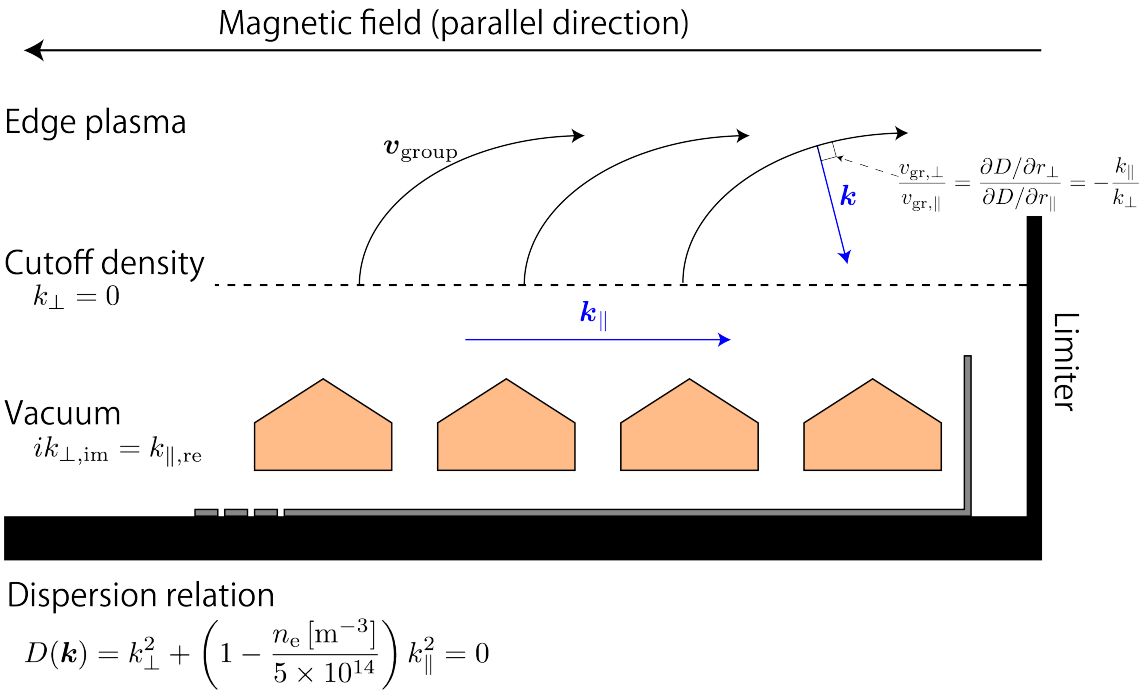

Figure 3.4: LHW propagation in the vicinity of the surface of a CCC antenna.

3.4 Soft X-ray detectors

Information on the energetic electrons accelerated by the LHW, such as the energy range and the degree of velocity space anisotropy, can be obtained by measuring the soft X-ray emission (10 eV–10 keV). The two types of detectors which have sensitivities in this energy range are used. The detectors are installed inside the vacuum vessel because photons in this energy range are seriously attenuated by air.

3.4.1 AXUV detector

An absolute extreme ultraviolet (AXUV) silicon photodiode used in the present experiment is manufactured by OPTO Diode Corp. and has sensitivity in the soft X-ray energy range (Fig. 3.5). One channel is located on the midplane at $R = 825$ mm with a radial sightline viewing through a vacuum vessel with a diameter of 60 mm.

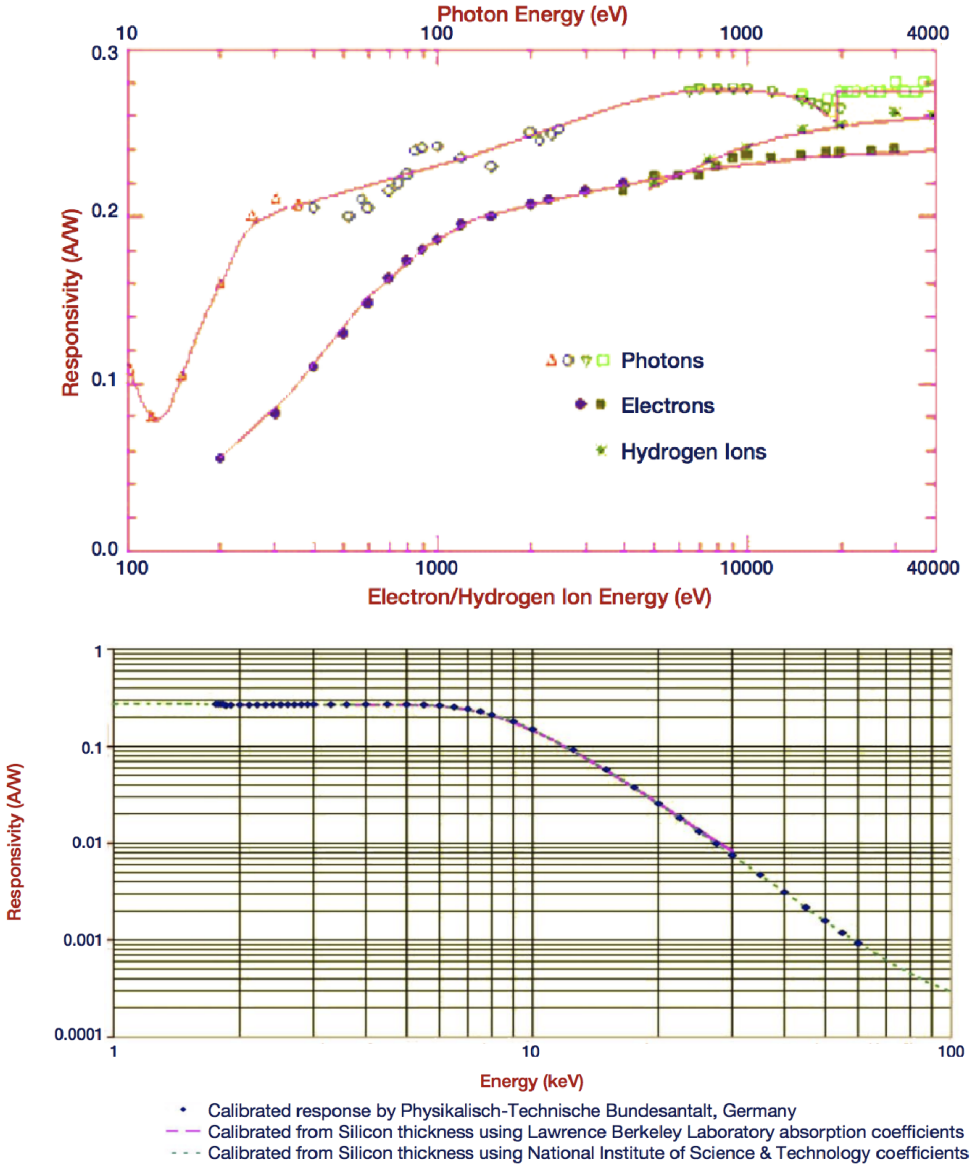

Figure 3.5: Responsivity of AXUV photodiode used in the present experiment [36]. In the photon energy range of 250 eV–8 keV, the responsivity is in the range of 0.2–0.3 A/W.

3.4.2 SBD detector

A surface barrier diode or a Schottky barrier diode (SBD) is a silicon detector with a thin aluminum film. The depletion layer in silicon has a thickness of 100 μm. By applying a bias voltage, current proportional to the incident photon energy is obtained (3.62 eV per electron-hole pair). On TST-2, a soft X-ray measurement is carried out with three SBDs, without a filter, with a polypropylene filter, and with a beryllium filter, in addition to AXUV detectors. The viewing sightlines and the viewing angles are the same as those of the horizontally viewing AXUV detector. The calculated attenuation properties and the sensitive energy range of SBD detectors are shown in Fig. 3.6.

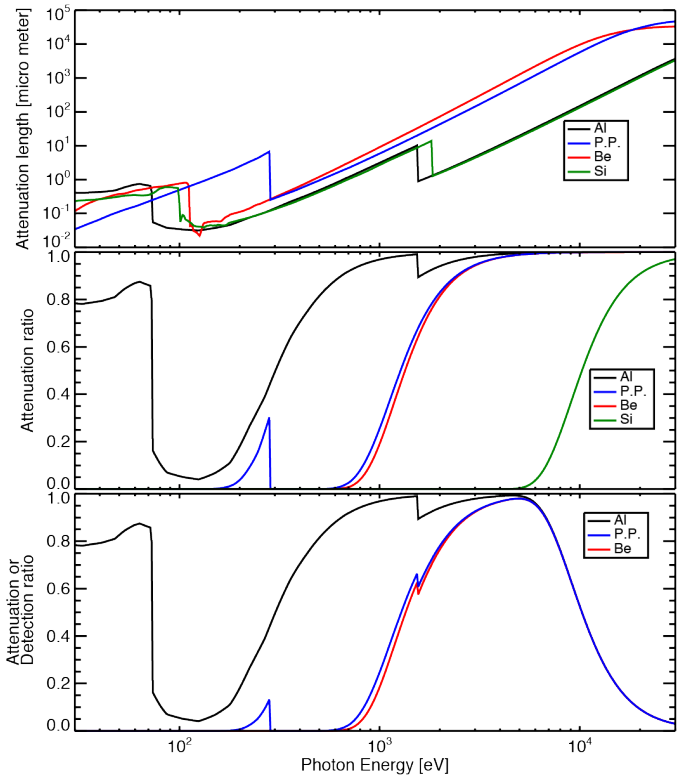

Figure 3.6: The soft X-ray attenuation characteristics of aluminum, polypropylene, beryllium, and silicon [37–39]. The attenuation length characterizes the strength of photon attenuation. The attenuation ratio is calculated by using the thicknesses used in the present experiment. The detection ratio is determined from the above calculations for the three detectors used in the present experiment (Al film only, Al film with 8 μm polypropylene filter, and Al film with 15 μm beryllium filter).

Chapter 4

Experimental Results

4.1 Typical plasma evolution

A typical example of a TST-2 plasma which was formed, ramped up the plasma current, and sustained entirely by non-inductive means, without the use of the CS, is shown in Fig. 4.1. First, neutral gas is introduced into the vacuum vessel with an externally applied toroidal magnetic field and a weak vertical magnetic field. The gas is ionized using the ECW at a frequency of 2.45 GHz, and the plasma is formed. The corresponding magnetic field for electron cyclotron resonance is 0.088 T. The ECW power is absorbed at a specific major radius in the vacuum vessel where the resonance condition is satisfied and produces an unconfined plasma distributed cylindrically with its axis coincident with the major axis of the torus and (Fig. 4.2). Subsequently, the LHW is launched (from the outboard antenna in this case). The LHW power is absorbed by electrons due to Landau damping, and a toroidal current is induced in the plasma. This initial current is mostly driven by the electron pressure gradient [40–42]. When the toroidal current becomes high enough so that the poloidal magnetic field produced by the toroidal current cancels the applied vertical field and a toroidal configuration with closed magnetic flux surfaces (tokamak configuration) is formed (Fig. 4.3). A current jump is observed when this spontaneous flux closure takes place. After the flux closure, current is driven mostly by wave-particle interaction, i.e., by Landau damping of the LHW and velocity space diffusion of the electron velocity distribution function. The current is ramped up by increasing the vertical magnetic field to satisfy the tokamak equilibrium condition (radial force balance). As the confinement of charged particles improves during plasma current ramp-up, the plasma density and pressure also increase. The plasma temperature is typically on the order of 10 eV, but gradually higher energy electrons are generated due to the acceleration of electrons by Landau damping. Since the confinement of energetic electrons also improves with plasma current increase, soft X-ray emission with photon energies of 1 keV or higher becomes observable. In particular, photon emission with energies above the soft X-ray band provides important

indications of the energetic electrons which carry the majority of the plasma current in plasma driven by the LHW.

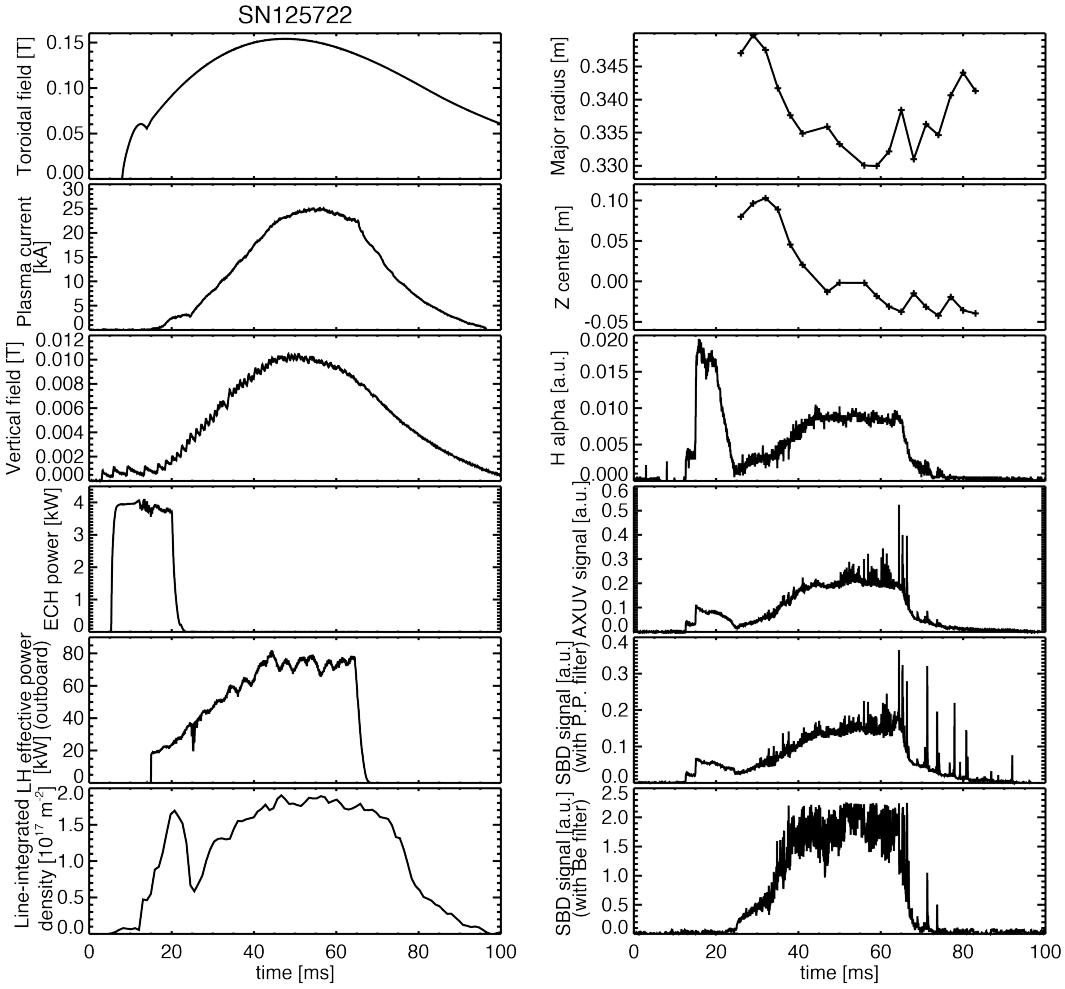

Figure 4.1: Typical example of a non-inductively driven TST-2 plasma. Parameters plotted are: toroidal magnetic field at $R = 0.38\,\mathrm{m}$ (near the plasma center), toroidal plasma current, vertical magnetic field, ECW input power, LHW input power from the outboard antenna, line integrated plasma density on the midplane ($z = 0$), major radius and vertical position of the geometric center of the plasma obtained by equilibrium reconstruction using EFIT [43], H_α line emission intensity, radiation detected by AXUV photodiode (photon energy: 1 eV–10 keV), radiation detected by SBD photodiode with polypropylene filter (photon energy: 100 eV–300 eV and 1 keV–10 keV), and radiation detected by SBD photodiode with beryllium filter (photon energy: 1 keV–10 keV). The lines of sight of photodiodes are horizontal on the midplane towards the plasma center.

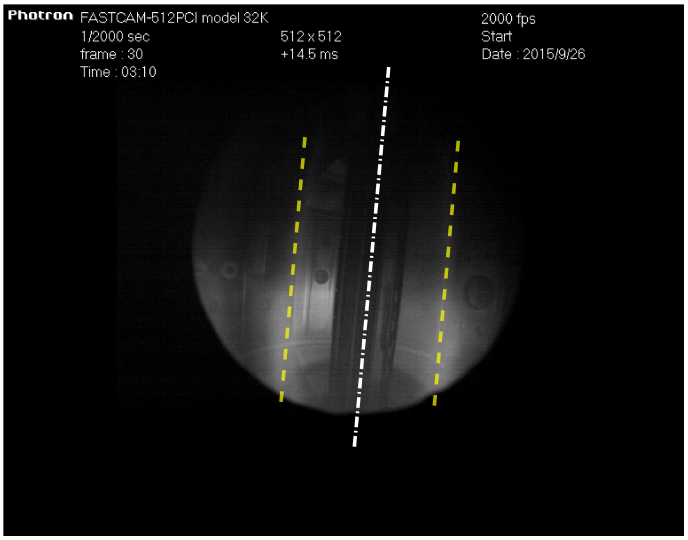

Figure 4.2: Cylindrical plasma produced by ECH ionization (14.5 ms). From the measured toroidal field, the major radius of the resonance surface is calculated to be 0.26 m. The white chain line indicates the vertical axis of TST-2, and the yellow dashed lines indicate the major radius where the plasma is cylindrically formed due to ECW.

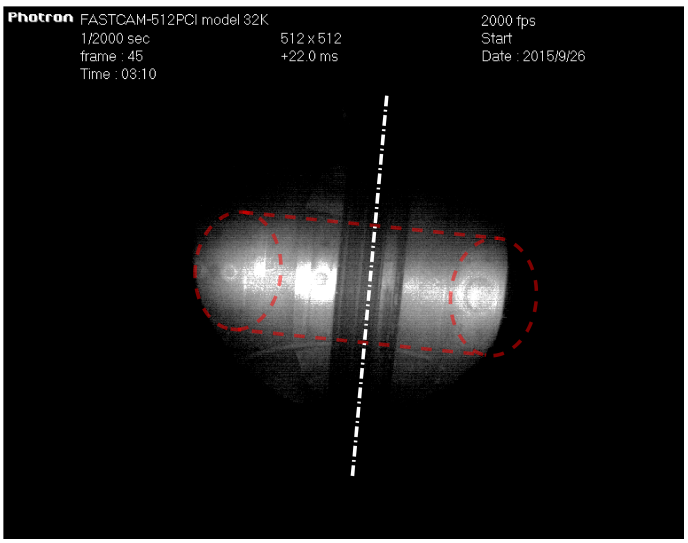

Figure 4.3: Tokamak configuration observed at 22 ms, formed after LHW injection which started at 15 ms. The white chain line indicates the vertical axis of TST-2, and the red dashed lines indicate the estimated tokamak shape seen from the picture.

4.2 Comparison among different launching locations

It is known empirically that it is difficult to start the plasma current using only the top-launch antenna. In Fig. 4.4, the initial plasma current ramp-up phase is compared between outboard launch and top launch cases. Although the ultimately achieved plasma currents are the same, in the top launch case the initial plasma formation is delayed, and the plasma current ramp-up rate is lower. The time delay from the initial toroidal current formation and the formation of closed magnetic surfaces (as indicated by the current jump) is 16 ms (from 15 ms to 31 ms in Fig. 4.4) for outboard launch and 21 ms (from 26 ms to 47 ms in Fig. 4.4) for top launch. For the top launch case, the plasma minor radius is smaller and unstable during this period, so it is difficult to ramp-up the plasma current by applying an additional vertical magnetic field. There are two reasons to explain the difficulty to use top launch LHW for plasma start-up. Firstly, since the plasma is initiated in front of the antenna, well above the midplane of the vacuum vessel, careful control of the vertical plasma position becomes necessary. Secondly, wave propagation and absorption are less favorable. During the early phase of the discharge when the plasma current is low, the poloidal wave number upshift hardly occurs because the poloidal magnetic field is too low, so the parallel wave number is determined almost entirely by the toroidal mode number n as $k_{\|} = n/R$. Although the excited wave numbers are nearly the same for both antennas, the excited toroidal mode numbers are significantly different, $n = 4.0$–7.9 for the top antenna and $n = 13.0$ for the outboard antenna. Since the toroidal mode number is conserved during propagation because of toroidal symmetry, the parallel wave number is inversely proportional to the major radius. In the case of outboard , the parallel wave number increases significantly while propagating in the plasma, but in the case of top , the parallel wave number does not change substantially (the parallel refractive index and the toroidal mode number are similar near $R = 0.24$ m). As a result, during the early phase of plasma start-up, top-launched LHW is poorly absorbed by Landau damping compared to outboard-launched LHW. Therefore, top-launch LHW is used after discharge with a plasma current of about 5 kA is formed by outboard-launch LHW.

For discharges using the top-launch antenna, experiments were also conducted with the direction of the toroidal magnetic field reversed. The purpose is to simulate the case of bottom-launch LHW. The reason is that in the case of top launch with the toroidal magnetic field in the normal direction, the helical magnetic field line directs the LHW towards the outboard side, whereas in the case of bottom launch, the LHW is directed towards the inboard side. When the direction of the toroidal magnetic field is reversed, the helicity of the magnetic field also reverses, and the top-launch LHW is directed towards the inboard side, simulating bottom launch. Using this fact, a comparison was made under the same conditions for top launch, outboard launch, and (simulated) bottom launch. The maximum injected RF power is about 80 kW and the vertical magnetic field is determined from the force balance of the plasma in the major radial

direction. The major radius is around 0.34 m, and the minor radius is around 0.21 m (Fig. 4.5). In this comparison, the highest plasma current achieved was 23.5 kA for bottom launch, 21.5 kA for top launch, and 19.5 kA for outboard launch.

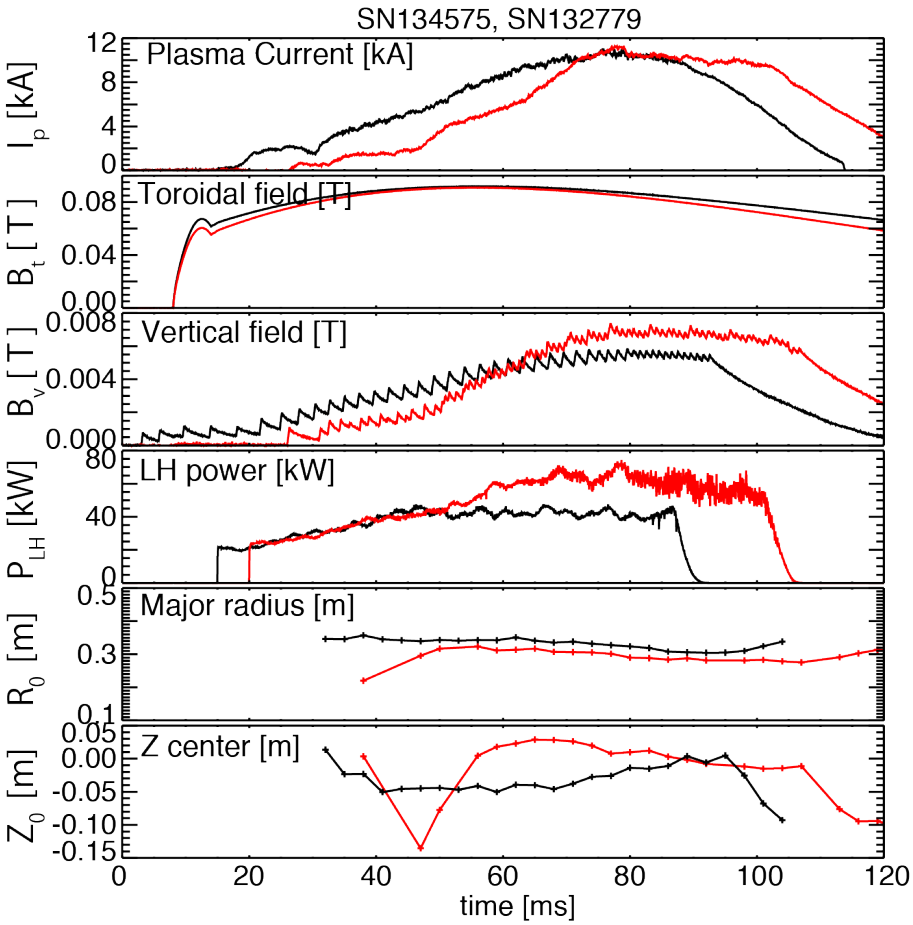

Figure 4.4: Comparison of plasma start-up between outboard launch (black) and top launch (red). Parameters plotted are: toroidal plasma current, toroidal magnetic field at $R = 0.38$ m (near the plasma center), vertical field, LHW input power from the outboard antenna and the top antenna, major radius and vertical position of the geometric center. The lines of sight of photodiodes are horizontal on the midplane towards the plasma center.

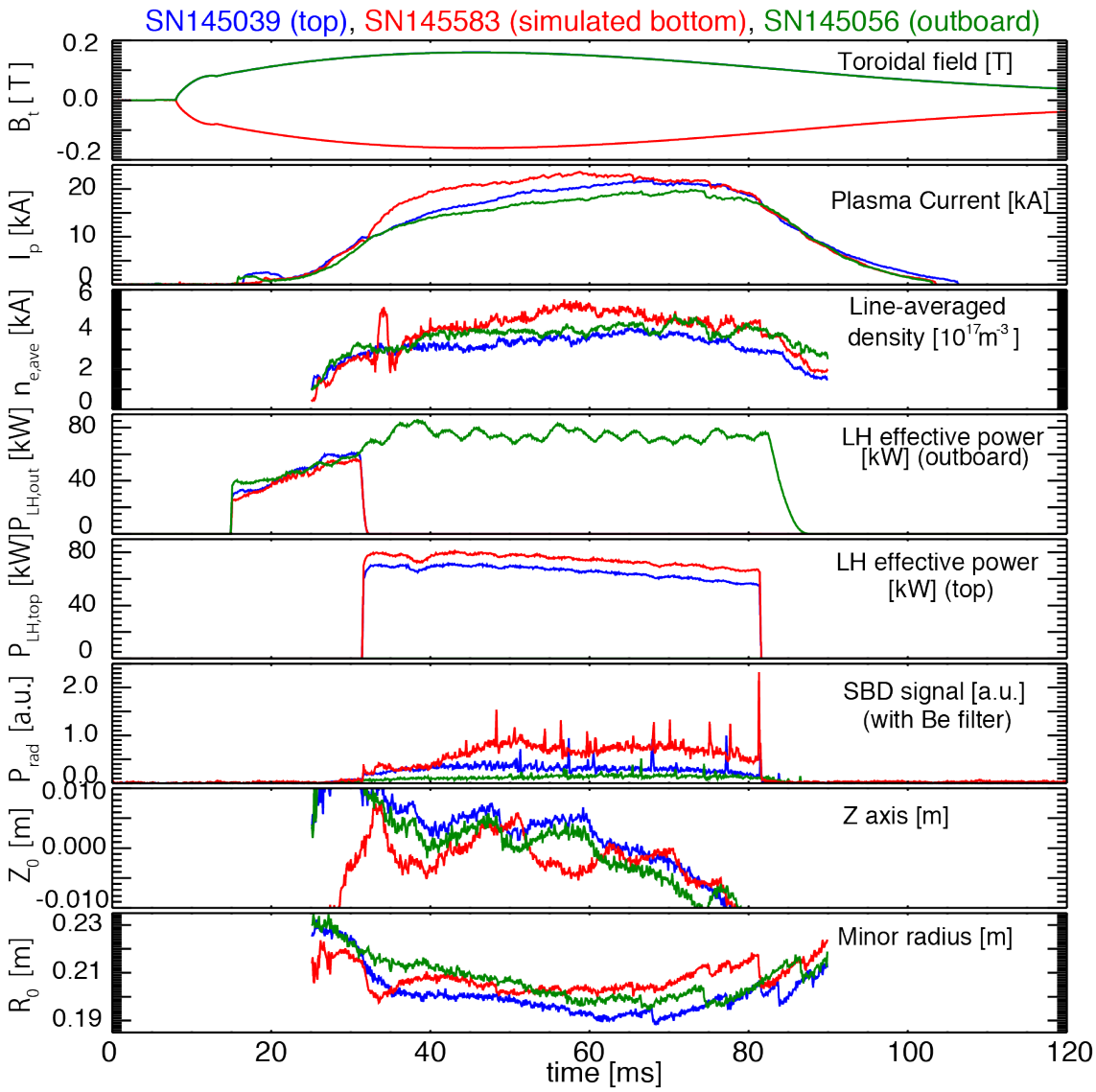

Figure 4.5: Comparison of discharges with simulated bottom launch (red), top launch (blue), and outboard launch (green). Plotted parameters are toroidal magnetic field at $R = 0.38\,\mathrm{m}$, plasma current, line averaged plasma density at midplane, LH input power from the outboard antenna, LH input power from top antenna, SBD photodiode signal with beryllium filter (photon energy: 1 keV–10 keV), vertical position and major radius of the geometric center of the plasma.

Although the plasma current ramp-up rate is determined by the ramp-up rate of the applied vertical magnetic field, there is a trade-off with the plasma minor radius due to the power balance in the major radial direction. For the discharges with the top limiter

position of 350 mm, we achieved a current value of 21.1 kA with the outboard , 26.0 kA with the top and 26.7 kA with the simulated bottom , which is the highest in TST-2 history. Fig. 4.7 shows the peak value of the drive current at each shot as a function of the toroidal magnetic field. In general, there is a positive correlation between the toroidal magnetic field and the driving current, and as a physical explanation, particle diffusion in the minor radial direction due to the Larmor motion and drift velocity can be suppressed by the toroidal magnetic field, and the plasma current can be improved due to better confinement of fast electrons. However, in Fig. 4.7, the peak value of the current is seen in the range of the toroidal magnetic field of 0.13–0.14 T in the case of outboard , and also in the case of top , the peak plasma current can be seen around 0.19 T. The apparent current peak is because the high magnetic field (coil current) cannot be maintained for a long time because of the capacity of the capacitor bank for the toroidal magnetic field coil, so achieving the maximum plasma current in the high magnetic field side required the fast increase of the plasma current at the same time. In order to increase the plasma current, it is necessary to increase the vertical magnetic field at the same time. On the other hand, an excessive vertical magnetic field causes a strong electromagnetic force in the axial direction of the vacuum vessel to the entire tokamak and finally destroy the equilibrium. Figure 4.7 shows a comparison of the average plasma current ramp-up rate from the start of RF power injection to the maximum current for each discharge. For discharges with the major radius of 0.32–0.33 m, the ramp-up rates were 0.91 MA/s for bottom launch, 0.76 MA/s for top launch, and 0.53 MA/s for outboard launch.

In the range 0.13–0.14 T, the restriction of the current ramp-up rate in the case of outboard launch still does not affect dominantly, and comparing that the maximum plasma current is 21.1 kA with the outboard launch and 23.6 kA with the top launch, it is estimated that there is a superiority of about 2.5 kA (11–12 %) for the top launch regardless of the limit of current ramp-up rate. From the above, top launch could produce more current by 2.5 kA than in the case of outboard launch in the discharges with the current ramp-up rate slow enough to follow even with the outboard launch, and top launch enabled to generate an additional current of about 2.4 kA (from 23.6 kA to 26.0 kA), which is limited by the constraint of the capacitor bank.

In comparison with the top launch and the simulated bottom launch, in the toroidal magnetic field range 0.17–0.18 T, the difference in the maximum plasma current is less than 0.5 kA and it is considered to be within the range of reproducibility. Therefore, it can not be said that there is a difference in driven current with the discharges where the current ramp-up rate is not severe for the top launch. On the other hand, in the discharges with the magnetic field of 0.19 T or more, since there is no positive correlation between the toroidal magnetic field and the driving current in the case of the top launch, the difference appears in the achievable plasma current due to the difference between the current ramp-up rate in the case of top launch and that of the simulated bottom launch. From the above, it can not be said that the simulated bottom launch drives

a significantly higher plasma current more than the top launch in the discharges with the current ramp-up rate slow enough to follow up with the top launch, and from the superiority of the current ramp-up rate, it can be estimated that the simulated bottom launch could generate an additional current of about 0.7 kA (about 3%) in the constraints of the capacitor bank.

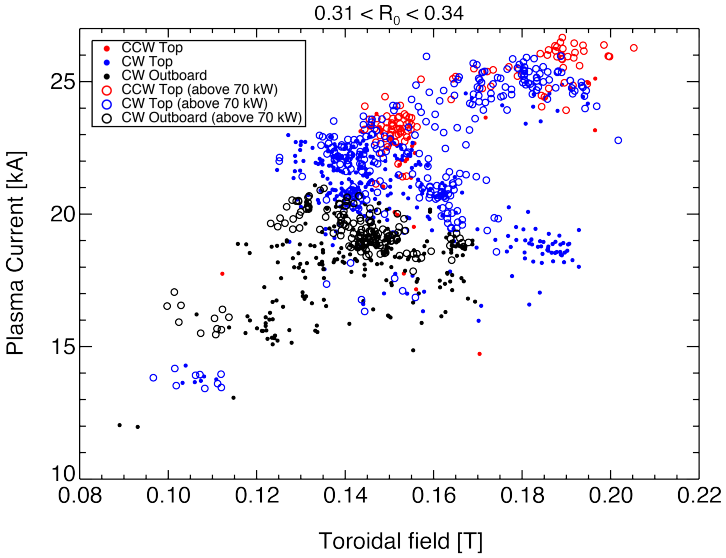

Figure 4.6: Dependences of the achieved plasma current on the toroidal magnetic field for simulated bottom launch (red: CCW top), top launch (blue: CW top), and outboard launch (black: CW outboard). The plasma major radius is in the range of 0.31 m $< R_0 <$ 0.34 m. The hollow circles indicate the discharges with LHW injection power above 70 kW.

4.3 Comparison among different top limiter positions

The plasma cross-section is determined by the cross section of the vacuum vessel. In TST-2, there is an outboard limiter for securing a low-density area in the vicinity of the antenna from the time of installing the outboard antenna for the length in the radial direction, and the plasma radial size is limited by the outboard limiter ($R = 585$ mm) and inboard limiter ($R = 130$ mm). Likewise, the maximum size is currently determined by the upper and lower limiters also in the vertical direction. Originally there were no upper and lower limiters, but there was a gap between the ceiling and floor of the TST-2 container (about $Z = \pm 700$ mm) and the closed flux surface. Since LHW can

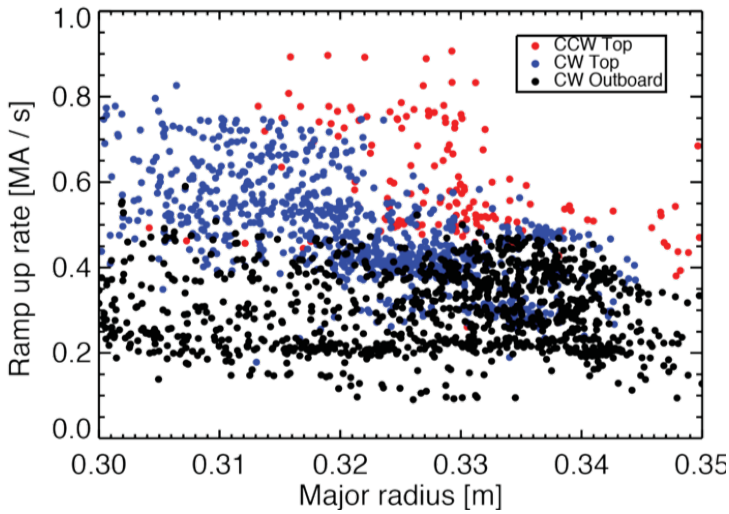

Figure 4.7: Dependence of the average plasma current ramp-up rate on the major radius for simulated bottom launch (red: CCW top), top launch (blue: CW top), and outboard launch (black: CW outboard).

also propagate within SOL if it is above the cutoff density, upper and lower limiters are provided to suppress the density of the gap range so that the power of LHW is not unnecessarily dissipated. When the limiter position is 450 mm, the density of the plasma core can be kept high with the similar power as compared with the case without the limiter, and the driven current value is improved. After the installation of the top antenna, the top limiter was lowered to $Z = 300$ mm in order to secure a low-density area near the antenna. As a result, the current value that can be driven with LHW decreases (Fig. 4.8), and it is considered that the excessive approach of the limiter limited the size of the core region as well as the gap region (see Fig. 4.8). When the limiter position was pulled up together with the top antenna and set to $Z = 350$ mm, the current value was improved 18 kA to 21 kA from, but the current amount was still restrained. As a result, the limiter position suitable for the current drive is between $Z = 350$ mm and $Z = 450$ mm.

4.4 Soft X-ray emission characteristics

As shown in Fig. 4.6, fast electrons of about 1 keV or more are additionally generated in the case of top launch. In the figure, discharge begins by the outboard launch, and it switches from 31 ms to top launch in approximately 2 ms. After that, it can be read from the signal of SBD with Be filter that it suddenly increases according to the current value raised by the fast electrons of 1 keV or more up to 45 ms. It is considered that

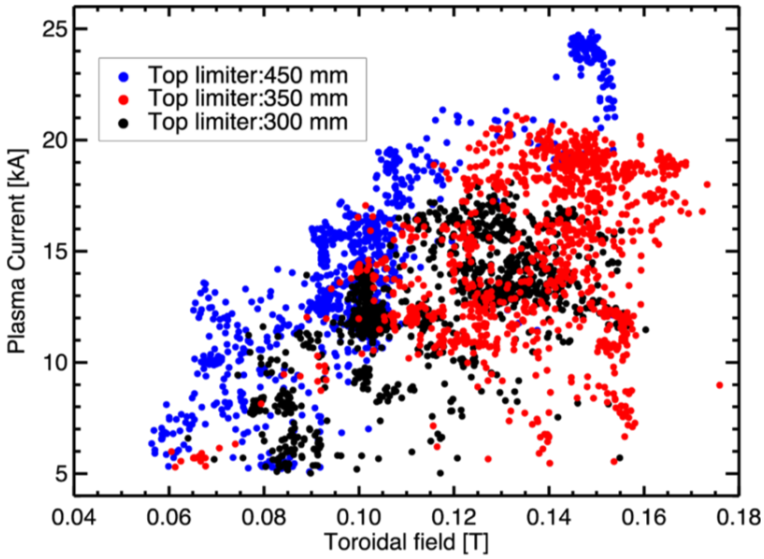

Figure 4.8: Comparison of achieved plasma current using outboard launch for different locations of the top limiter: 450 mm (blue), 350 mm (red), and 300 mm (black).

a sufficient amount of fast electrons are generated by Landau damping so far. Subsequently, the signal amount of the SB filter with the Be filter has a strong positive correlation with the incident power of the upper antenna. An interesting phenomenon in comparing discharges of different plasma currents is that the maximum intensity detected by the SBD with polypropylene filter is largely divided into two ways corresponding to the maximum plasma current. This change is far from the issuance of SBD with Be filter, and it is considered that photons of 200–300 eV capable of transmitting only polypropylene, or electrons of similar energy band generating the photons are involved. The following equation expresses the relationship of the wave number of the LHW and the kinetic energy of the produced fast electrons due to Landau damping.

$$E = \frac{511}{2N_{\parallel}}\,[\mathrm{keV}] \tag{4.4.1}$$

In order to increase the electrons in this energy region, it is necessary to increase the wave number up to $N_{\parallel} = 29$–35. From this comparison, in the discharge above the current value of 15 kA, the significant increase of SBD with polypropylene filter can be seen in the next chapter, but it changes greatly with discharge exceeding 18 kA. When comparing with discharges (18 kA, 19.5 kA, 20.5 kA) where the current value is 18 kA or more, the characteristics of change do not seem to differ much. The wave number increase will be discussed using the theory and the calculations in the next chapter. As a result, it is found that the plasma current at which the electrons start to generate

200–300 eV due to the sharp rise in wave number is about 16 kA, which coincides well with the phenomenon observed by an experiment. Also, since the thermal speed of electrons limits the wave number increase, it is in good agreement with the expectation that the emission with the energy of 200-300 eV will be saturated under the plasma current of 18 kA or more.

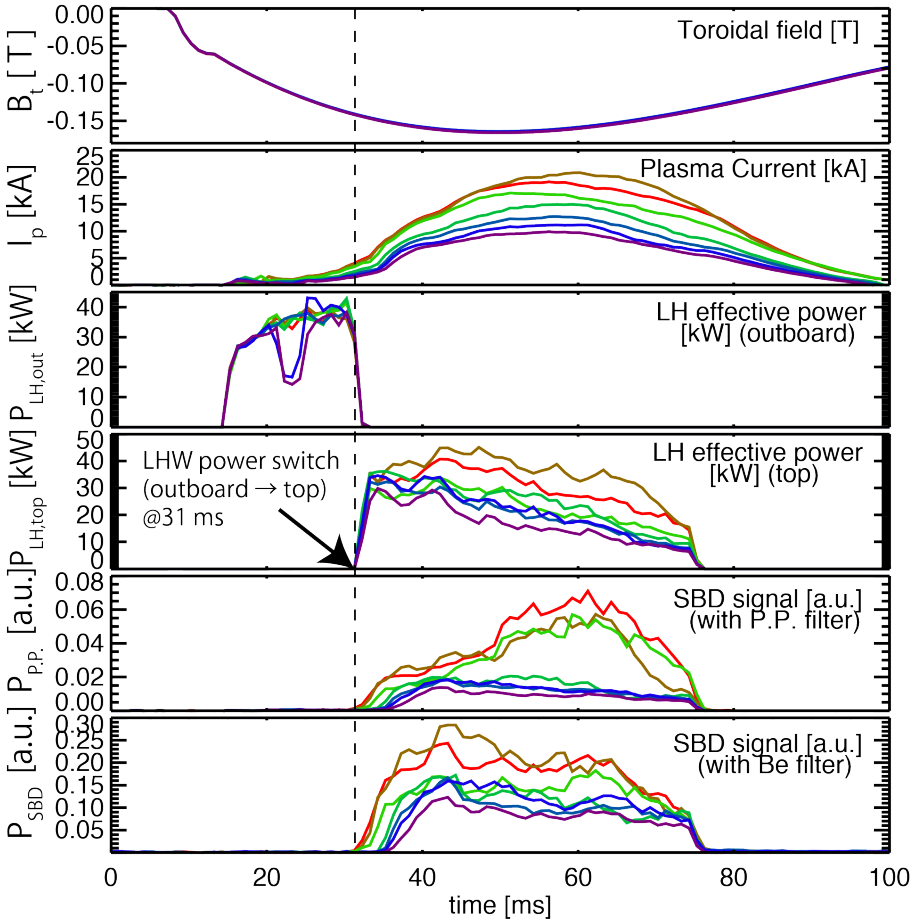

Figure 4.9: The waveforms for different maximum plasma currents (10–20 kA). SBD photodiode signal with polypropylene filter (photon energy: 100 eV–300 eV, 1 keV–10 keV) and SBD photodiode signal with beryllium filter (photon energy: 1 keV–10 keV).

Chapter 5

Wave and Particle Numerical Simulation

5.1 Comparison among different launching locations

Propagation and absorption of LHW were calculated for different launching locations using the GENRAY ray-tracing code [44]. The electron temperatures and density profiles measured by the Thomson scattering were used. The electron temperature profile is hollow with central and edge values of 10 eV and 50 eV. The electron density profile is peaked with the central value of $7.7 \times 10^{17}\,\mathrm{m}^{-3}$. The wave number of the injected LHW is distributed in the range $|N_\parallel| = 2.7$–9.5 for the outboard-launch antenna and $|N_\parallel| = 1.4$–8.7 for the top-launch antenna.

LHW propagation was calculated using GENRAY for different launching locations (Fig. 5.1) [45]. The parallel wave number of the LHW launched from the outboard antenna increases in inverse proportion to the major radius because the toroidal mode number is conserved. On the other hand, for the LHW launched from the top antenna the parallel wave number evolution is greatly influenced by the evolution of the poloidal mode number, so the wave number changes independently of the major radius. In this temperature range (10 eV to 50 eV), $N_\parallel$ increases to about 30 and the LHW is strongly absorbed by electron Landau damping. In the case of top launch, LHW is absorbed near $r/a \sim 0.5$, but in the case of outboard launch, strong absorption by thermal electrons occurs near the plasma edge. In the case of simulated bottom launch (top launch with reversed B_t), $N_\parallel$ decreases initially as the LHW approaches the midplane, and the LHW continues propagating downward and is reflected at the bottom limiter. After reflection, the LHW propagation is similar to the top-launch case (but upside down), and the parallel wave number increases towards the inboard side.

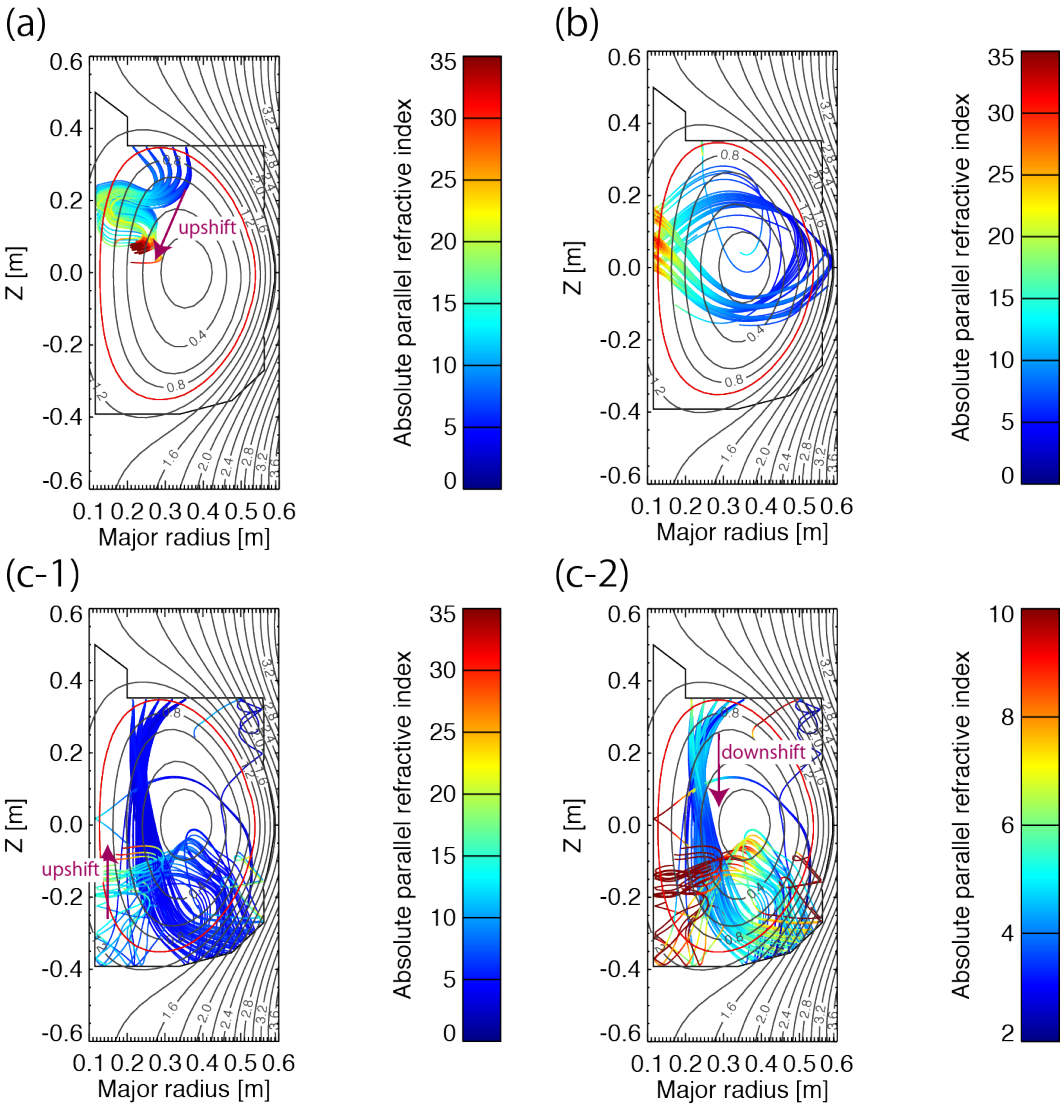

Figure 5.1: LHW propagation calculated by GENRAY. (a) Top launch, (b) outboard launch, and (c-1), (c-2) simulated bottom launch (top launch with reversed B_t) with two different color scales for the absolute value of the parallel refractive index.

The electron velocity distribution function is obtained by solving the Fokker-Planck equation using the CQL3D code [46]. The current density profile (Fig. 5.2) is obtained by taking a velocity moment of the distribution function $\int d\boldsymbol{v} v_{\mathrm{tor}} f(\boldsymbol{v})$, where v_{tor} is the toroidal electron velocity, $\boldsymbol{v}$ is the eletron velocity, and $f(\boldsymbol{v})$ is the velocity distribution function. The relative values of the calculated driven current (highest for top launch with reversed B_t, intermediate for top launch, and lowest for outboard launch) agree

qualitatively with experimental results (see Fig. 4.5 and Fig. 5.2). The current is distributed in the range $r/a = 0.4$–1.0 in all cases, but the current is lowest in the case of outboard launch. This is because the strong upshift in wave number occurs near the inboard edge in the case of outboard launch, so wave absorption and electron acceleration occur in this region. Consequently, the fraction of accelerated electrons with unconfined orbits (i.e., orbit loss) increases and the driven current is reduced.

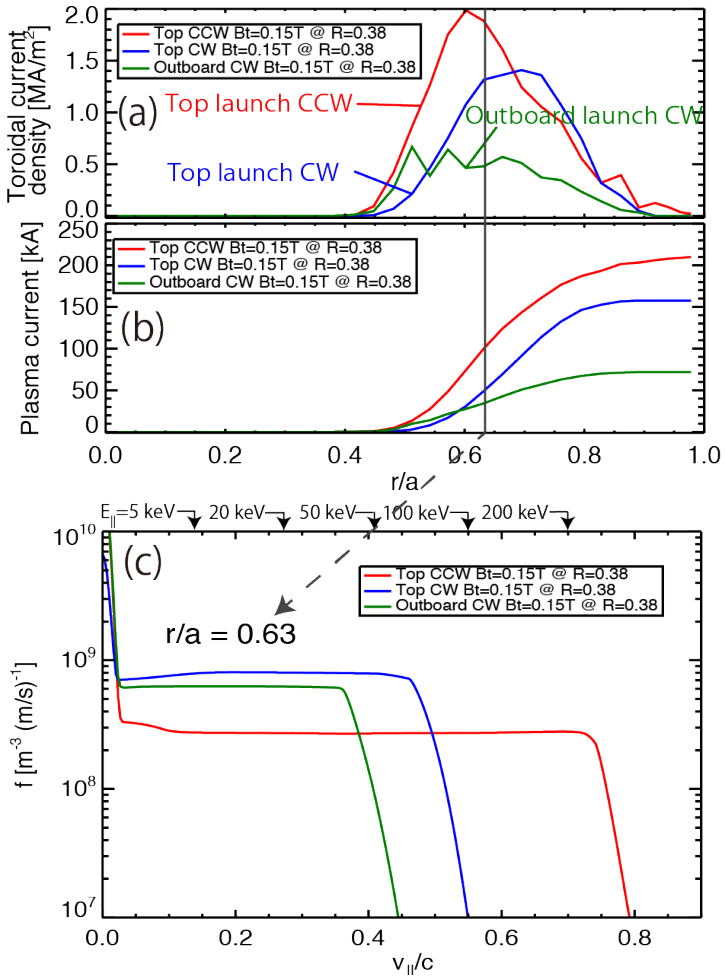

Figure 5.2: (a) Driven plasma current density profile, (b) integrated plasma current, and (c) electron parallel velocity distribution function obtained by GENRAY/CQL3D.

The experimental observation that the driven current is higher for simulated bottom launch than top launch can be explained as follows. When the LHW is absorbed strongly by thermal electrons due to the parallel wave number upshift, thermal electrons are accelerated and the velocity distribution function is flattened locally. The

accelerated electrons absorb LHW with higher phase velocities (lower wave numbers). This process continues progressively, and faster electrons are generated as LHWs with faster phase velocities are absorbed, until there are no more LHWs with faster phase velocities. In both simulated bottom launch and top launch cases, there are regions where the parallel wave number increases around $r/a \sim 0.5$ and the region where the parallel wave number hardly changes from $N_\parallel = -5$ (Figs. 5.1(b) and 5.1(c-1)). The electron velocity distribution function becomes widely flattened over the velocity range corresponding to this range of parallel wave number. In the case of simulated bottom launch, the parallel wave number decreases immediately after launch, enabling the generation of faster electrons. Considering that the calculation shows the tail of the velocity distribution function extending to significantly higher velocities in the case of simulated bottom launch, the driven current (which is proportional to the velocity moment) is higher than for top launch. This result indicates that the additional current due to the parallel wave number downshift is significant. The range of wave numbers and the electron velocity distribution function formed by LHW are summarized below,

As indicated in Sec. 2.10, the LHW wave numbers in the plasma determine the electron velocity distribution. As can be seen in Fig. 5.2, flattening of the electron velocity distribution function by quasi-linear velocity space diffusion connects the energetic electron distribution to the bulk (Maxwellian) electrons. The lower limit and the upper limit of the quasi-linear plateau determine the electron distribution function and the driven current.

- Top launch: The wave number increases continuously up to $|N_\parallel| \sim 35$ where the LHW rays are totally absorbed in the plasma while propagating in the poloidal direction in the region $r/a \sim 0.6$. Since there is no decrease in wave number, the launched wave number ($|N_\parallel| = 1.4$–8.7) and the slight wave number increase immediately after launching determines the width of the non-Maxwellian electron velocity distribution function, and the upper limit of the velocity distribution function is determined. The result of CQL3D calculation shows flattening of the distribution function to about $v/c = 0.47$. Therefore, it can be estimated that $|N_\parallel| = 2.1$ is the lower limit of the wave number .

- Outboard launch: The LHW rays pass through the region of $r/a \sim 0.6$ mostly along the poloidal direction, but the maximum wave number in this region is smaller than that for the case of top launch ($|N_\parallel| \sim 20$), and the electron velocity distribution extends to about $v/c = 0.36$. Therefore, $|N_\parallel| = 2.8$ is the lower limit of the wave number. This agrees with the lower limit of the launched wave number ($|N_\parallel| = 2.7$–9.5).

- Simulated bottom launch: The wave number continuously decreases by a factor of two in the region of $r/a \sim 0.6$. The wave number returns to the value at the time of launching around the lower side limiter, and some rays undergo wavenumber

upshift (although it is not enough to contribute significantly to the height of the plateau). Since the distribution function is flat up to $v/c = 0.75$, it is estimated that $|N_\parallel| = 1.3$ is the lower limit of the wave number.

There is a factor of $|N_{\parallel,\min}^{-2}|$ in the expression for the driven current (Eq. 2.10.4). In the case of simulated bottom launch, this factor ($1.3^{-2} = 0.59$) is more than a factor of two larger than for other injection schemes (top launch: $2.1^{-2} = 0.23$, outboard launch: $2.8^{-2} = 0.13$).

For top launch and bottom launch, there are advantages and disadvantages regarding the height and width of the quasi-linear plateau. The driven current is the highest for simulated bottom launch both experimentally and numerically. It is shown that a significant wave number decrease is expected only in the case of simulated bottom launch. It is certain that this is an important factor to maximize the driven current.

In order to maximize the LHW driven current, both the width and the height of the quasi-linear plateau must be considered. First of all, considering that the velocity distribution initially develops from the Maxwellian distribution by Landau damping, the height of the non-plateau is determined by the maximum parallel wave number of the absorbed wave. In contrast, after the distribution begins to evolve, the minimum parallel wave number to be absorbed becomes important for determining the theoretically achievable plasma current. It is difficult to keep the desired high wave number component and low wave number component by LHW launched from a single location. It is more realistic to ensure these wave number components by simultaneous launching from multiple locations. Comparing the characteristics of the converged velocity distribution functions depending on the launch location shown in Fig. 5.2. It is optimal to use the top launch for the height of the plateau and simulated bottom launch for the width. It can be seen that the simultaneous launch from the top and the bottom has the best synergistic effect with respect to current drive.

5.2 Wave number evolution

Consider a dimensionless dispersion relation

$$D = \frac{1}{2}\left(1 + \frac{Sk_\perp^2}{Pk_\parallel^2}\right) = 0. \tag{5.2.1}$$

Since the relationship $D = 0$ must always be satisfied as the wave propagates through the plasma, D is a conserved quantity, and can be regarded as a Hamiltonian for wave propagation. The parameter τ can be interpreted to be the time normalized by the wave period from the following equation,

$$\frac{\mathrm{d}t}{\mathrm{d}\tau} = -\frac{\partial D}{\partial \omega} \sim -\frac{1}{P}\frac{\omega_{\mathrm{pe}}^2}{\omega^3} \simeq \frac{1}{\omega}. \tag{5.2.2}$$

The temporal evolutions of the wave number and the wave position are expressed as follows using τ,

$$\frac{\mathrm{d}\boldsymbol{k}}{\mathrm{d}\tau} = -\frac{\partial D}{\partial \boldsymbol{r}} = -\frac{\partial}{\partial \boldsymbol{r}} \ln \frac{|P|}{S}, \tag{5.2.3}$$

$$\frac{\mathrm{d}\boldsymbol{r}}{\mathrm{d}\tau} = \frac{\partial D}{\partial \boldsymbol{k}} = k_{\parallel}^{-1}\boldsymbol{e}_{\parallel} - k_{\perp}^{-1}\boldsymbol{e}_{\perp}. \tag{5.2.4}$$

In the LH frequency range, P and S are approximated as

$$P \simeq -\frac{\omega_{\mathrm{pe}}^2}{\omega^2} \simeq \frac{n_{\mathrm{e}}\,[\mathrm{m}^{-3}]}{5\times 10^{14}}, \tag{5.2.5}$$

$$S \simeq 1 + \frac{\omega_{\mathrm{pe}}^2}{\Omega_{\mathrm{e}}^2} - \frac{\omega_{\mathrm{pi}}^2}{\omega^2} \simeq 1 + \left(\frac{9\sqrt{n_{\mathrm{e}}\,[10^{18}\,\mathrm{m}^{-3}]}}{28 B_{\mathrm{t}}\,[T]}\right)^2 \left[1 - \left(\frac{B_{\mathrm{t}}\,[T]}{0.44}\right)^2\right], \tag{5.2.6}$$

where ω_{pi}^2 is the ion cyclotron frequency. Typical peak densities in non-inductively started TST-2 plasmas are in the range 5×10^{17} to $10^{18}\,\mathrm{m}^{-3}$, and the toroidal magnetic field at the plasma center is in the range 0.1 to 0.2 T. Since P depends only on the density, it is constant on the magnetic surface, but S is a decreasing function of the magnetic field for our field strength (where B_{t} is far below 0.44 T). Especially in the vicinity of the magnetic axis, $\omega_{\mathrm{pe}}/\omega_{\mathrm{ce}}$ is much greater than 1 and decreases on the high magnetic field side (inboard side). As a result, $-P/S$ has a peak slightly towards the high field side of the magnetic axis. Eventually, the poloidal component contributes to the gradient of $-P/S$, and the poloidal wave number changes. As can be seen from Fig. 5.3, when the LHW is in the upper half of the plasma, the absolute value of the incident wave number increases, and if it is in the lower half, the wave number decreases.

The LHW propagates to the inboard side for top launch and simulated bottom launch, but this can be interpreted as follows. The pitch angle $B_{\mathrm{p}}/B_{\mathrm{t}}$ (B_{p} is the poloidal magetic field) of the magnetic field in non-inductively started TST-2 plasma is 0.05 at most where plasma current is driven, even for the total plasma current I_{p} of 20 kA. Without considering the pitch angle, the LHW trajectory perpendicular to the magnetic field is in the poloidal direction. The ray equation can be written as $d\boldsymbol{r}_{\perp}/d\tau = -k_{\perp}\boldsymbol{e}_{\perp}$, and in the direction perpendicular to the magnetic field line, the direction of the wavevector and the direction of the group velocity are reversed. In the case of top launch, the poloidal wave number increases along the downward gradient of $-P/S$, and the direction of group velocity approaches the direction of the upward gradient (Fig. 5.3).

As a result, the LHW propagates towards the inboard side to the peak of $-P/S$. However, this is the case in which the pitch angle is completely ignored. Since the LHW propagates nearly in the same direction as the magnetic field line, the effect of a small pitch angle should be added. In the case of LHW, the direction of wave propagation deviates from the magnetic field line by the angle $\sqrt{-S/P}$ rad (which

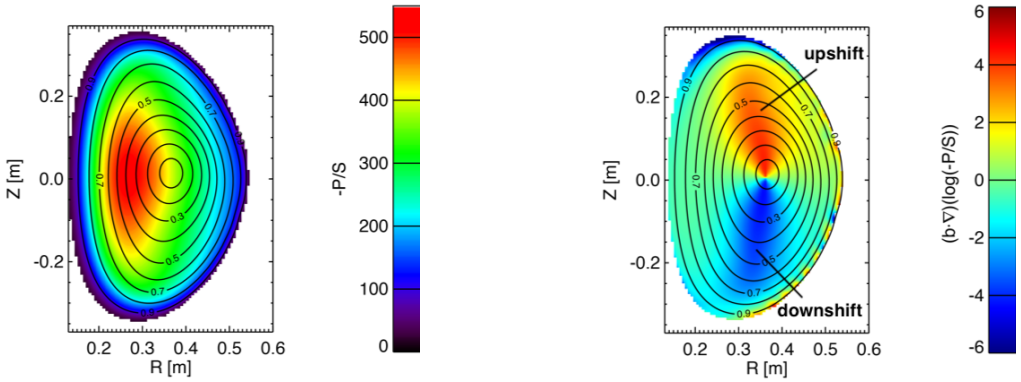

Figure 5.3: $-P/S$ profile (left) and the poloidal gradient of $-P/S$ (right) for typical density profile [47]. The peak density is $7.7 \times 10^{18}\,\mathrm{m}^{-3}$, and the toroidal field is 0.15 T at the magnetic axis ($R = 0.38\,\mathrm{m}$). When the poloidal gradient is positive, the poloidal wave number change causes parallel wave number upshift. When the poloidal gradient is negative, the poloidal wave number change causes parallel wave number downshift.

is called resonce cone). With this alone, one degree of freedom remains for LHW propagation in azimuthal direction, but when upshift or downshift of the wave number occurs due to the gradient of $-P/S$, the LHW has a strong directivity in the poloidal direction rather than in the perpendicular direction to the magnetic surface, as shown in Fig. 5.4. In this case, the propagation of the wave in the poloidal direction is determined by comparing the pitch angle $B_\mathrm{p}/B_\mathrm{t}$ and the resonance cone angle $\sqrt{-S/P}$.

Figure 5.5 shows the pitch angle normalized by the angle of resonance cone $B_\mathrm{p}\sqrt{-P}/B_\mathrm{t}\sqrt{S}$. If this value is less than 1 and has a strong directivity in the poloidal direction by upshift or downshift, the LHW is expected to propagate towards the peak of $-P/S$, whereas if this value is greater than 1, the LHW propagates following the magnetic field line twist. An interesting point is that the normalized pitch angle is about 0.5 on the upper side in the vicinity of $r/a \sim 0.5$, but it approaches 1 near the midplane. This is due to the combined effect of $-P/S$ which is peaked on the inboard side and of the increasing pitch angle due to the narrower space between magnetic surfaces. In the case of top launch, the poloidal direction towards the peak of $-P/S$ from the antenna and the direction of magnetic field line twist are opposite, which makes the wave stagnant near the midplane. This fact explains that a large wave number increase occurs near the midplane for top launch as shown in Fig. 5.1, though the poloidal projection of the gradient of $-P/S$ is small. On the other hand, wave number downshift is not significant. In the case of simulated bottom launch, the wave number decreases to about half ($N_\parallel = 2$–3) at the midplane, but no further wave number decrease occurs. Downshift occurs in the case of simulated bottom launch because $d\boldsymbol{k}_\mathrm{p}/d\tau$ does not change, while the magnetic field line twist is reversed, so the contribution of $\boldsymbol{k}_p$ is reversed. The pitch angle and the upward gradient of $-P/S$ match with each other

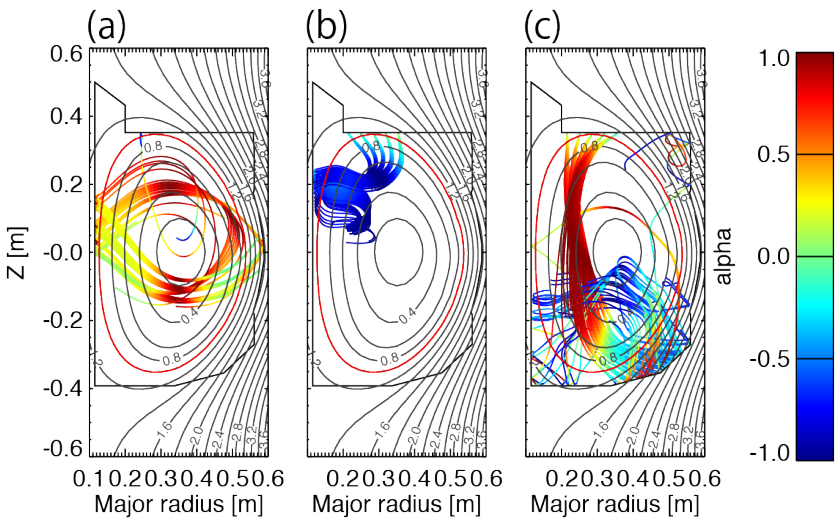

Figure 5.4: The directivity of wavevector along the poloidal field $\boldsymbol{k} \cdot \boldsymbol{B}/k|B|$. Different plots are showing the cases of (a) outboard launch, (b) top launch, and (c) simulated bottom launch. Strong directivity along the poloidal direction is observed where significant upshift/downshift can be seen.

due to the reversal of the field line twist, so instead of slowing down, acceleration takes place.

The degree of change in the wave number by upshift or downshift is derived from the toroidal mode number conservation. The toroidal mode number is expressed as follows using wave number components in parallel and perpendicular directions:

$$k_{\mathrm{tor}} R = \left(k_{\parallel} \cos\theta + \alpha k_{\perp} \sin\theta \right) R, \tag{5.2.7}$$

where

$$\theta = \arctan \frac{B_{\mathrm{p}}}{B_{\mathrm{t}}} \simeq \frac{B_{\mathrm{p}}}{B_{\mathrm{t}}}, \tag{5.2.8}$$

$$\alpha = \frac{\boldsymbol{k}_{\perp} \cdot \boldsymbol{B}_{\mathrm{p}}}{k_{\perp} B_{\mathrm{p}}}. \tag{5.2.9}$$

Applying the LHW dispersion relation $k_{\perp} = k_{\parallel}\sqrt{-P/S}$ and neglecting the second and higher order terms of pitch angle, the toroidal mode number is approximated as

$$k_{\mathrm{tor}} R \simeq k_{\parallel} \left(1 + \alpha \sqrt{\frac{|P|}{S}} \frac{B_{\mathrm{p}}}{B_{\mathrm{t}}} \right) R = \mathrm{const.} \tag{5.2.10}$$

The equilibrium reconstructions used in Figs. 5.6, 5.7, 5.8, and 5.9 were based on magnetic data taken in a discharge with a plasma current of 20 kA. Based on these

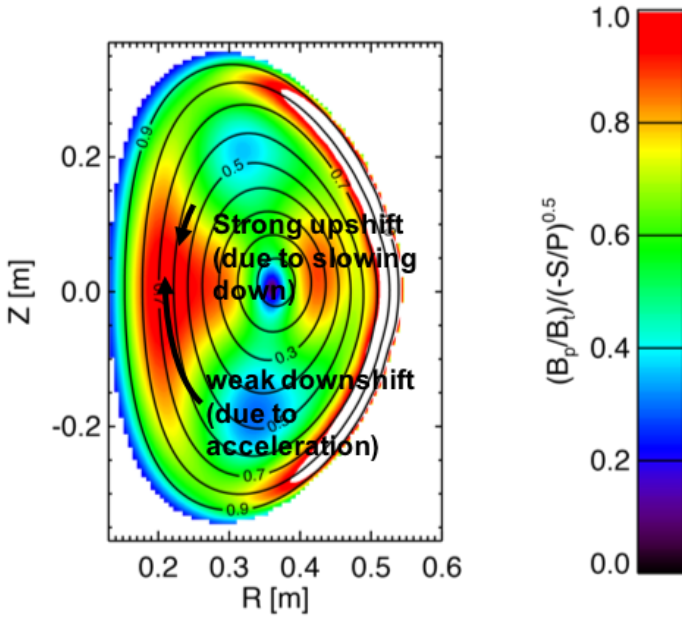

Figure 5.5: Normalized pitch angle.

data, the poloidal magnetic field was calculated by scaling the poloidal magnetic field to different values of the plasma current. In these figures, the rays were traced until 80 % of the injected RF power is absorbed by the plasma. In the calculation for $I_p = 20\,\mathrm{kA}$, the normalized pitch angle was nearly 1 in the vicinity of the midplane. In the case of top launch, a rapid increase in $N_\parallel$ occurrs in this region, and a strong wave absorption by thermal electrons takes place. For the cases shown in Fig. 5.6 ($I_p = 6\,\mathrm{kA}$ and $8\,\mathrm{kA}$), $N_\parallel$ is inversely proportional to the major radius ($N_\parallel \propto R^{-1}$) because the magnetic field pitch angle is very small. For the cases shown in Fig. 5.7 ($I_p = 10\,\mathrm{kA}$ and $14\,\mathrm{kA}$), a significant $N_\parallel$ upshift occurs near the midplane. For the cases shown in Fig. 5.8 ($I_p = 16\,\mathrm{kA}$ and $18\,\mathrm{kA}$), $N_\parallel$ variation due to the effect of normalized pitch angle becomes important. It is noteworthy that $N_\parallel$ on the midplane increases from 20 to 30 due for a small plasma current increase of only $2\,\mathrm{kA}$. It is suggested that there is a threshold plasma current (above $16\,\mathrm{kA}$ in this case) above which $N_\parallel$ upshift increases abruptly. Finally, for the cases shown in Fig. 5.9 ($I_p = 20\,\mathrm{kA}$ and $24\,\mathrm{kA}$), the $N_\parallel$ upshift is sufficient to cause strong absorption, and the location where the normalized pitch angle becomes 1 shifts upward and the position where strong $N_\parallel$ upshift occurs slightly shifts upward as the plasma current increases further.

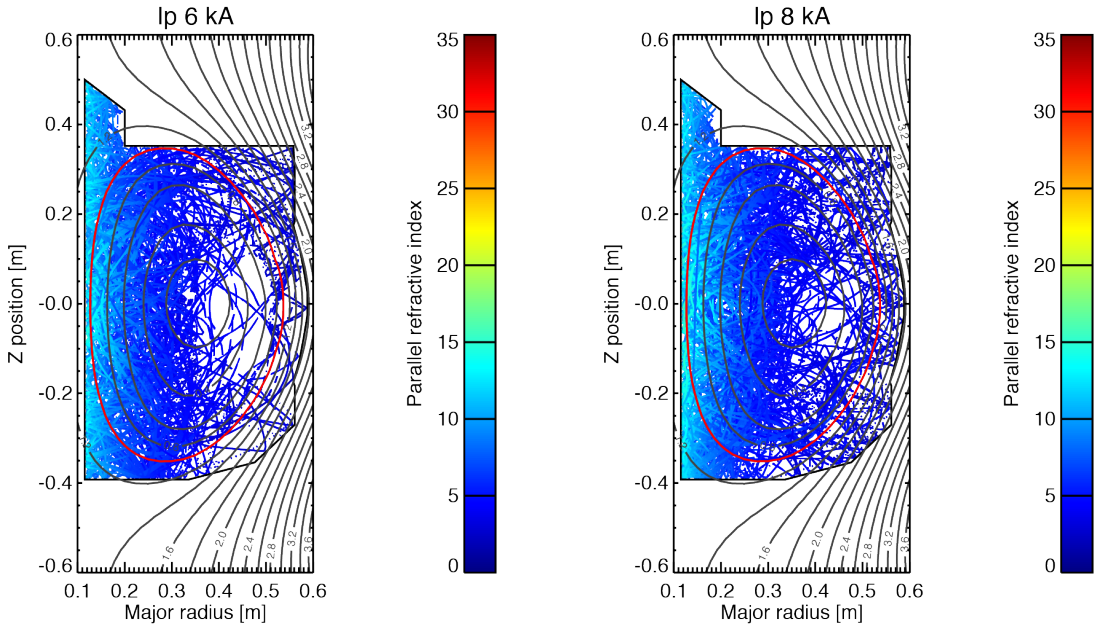

Figure 5.6: Evolution of $N_{\|}$ calculated by GENRAY for $I_{\mathrm{p}} = 6\,\mathrm{kA}$ (left) and $8\,\mathrm{kA}$ (right).

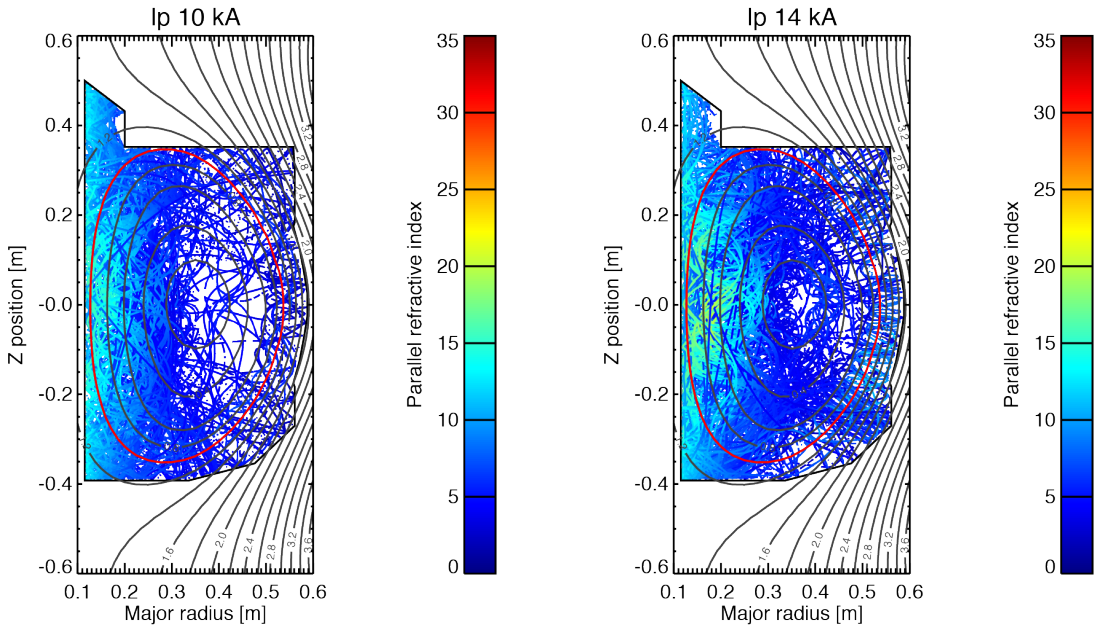

Figure 5.7: Evolution of $N_{\|}$ calculated by GENRAY for $I_{\mathrm{p}} = 10\,\mathrm{kA}$ (left) and $14\,\mathrm{kA}$ (right). $N_{\|}$ upshift occurs near the midplane.

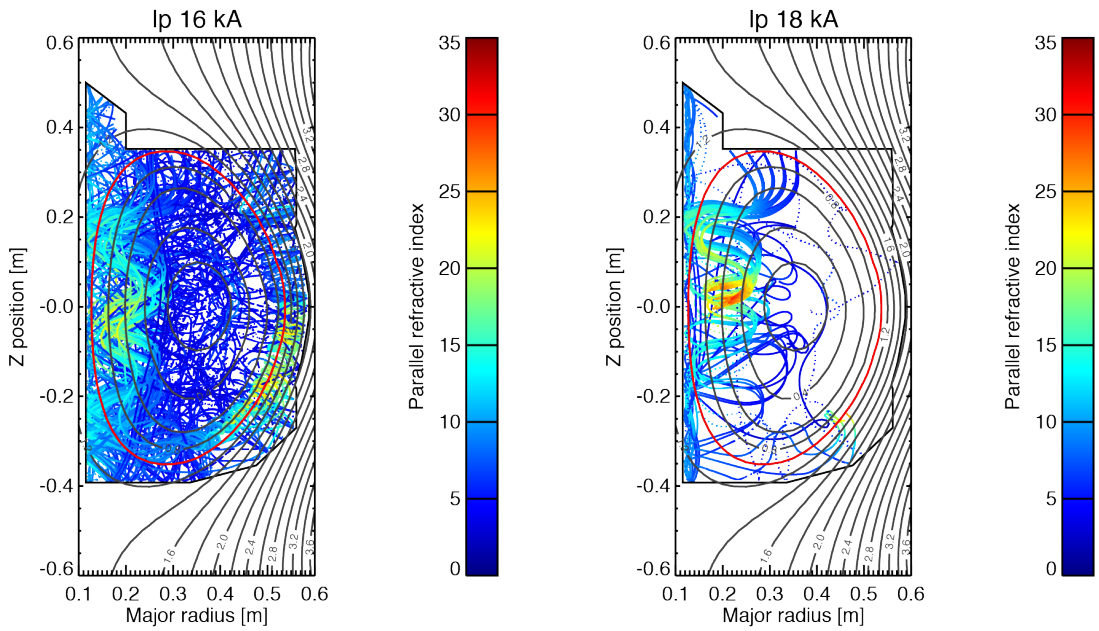

Figure 5.8: Evolution of $N_{\|}$ calculated by GENRAY for $I_{\mathrm{p}} = 16\,\mathrm{kA}$ (left) and $18\,\mathrm{kA}$ (right). Significant $N_{\|}$ upshift can be seen near the midplane.

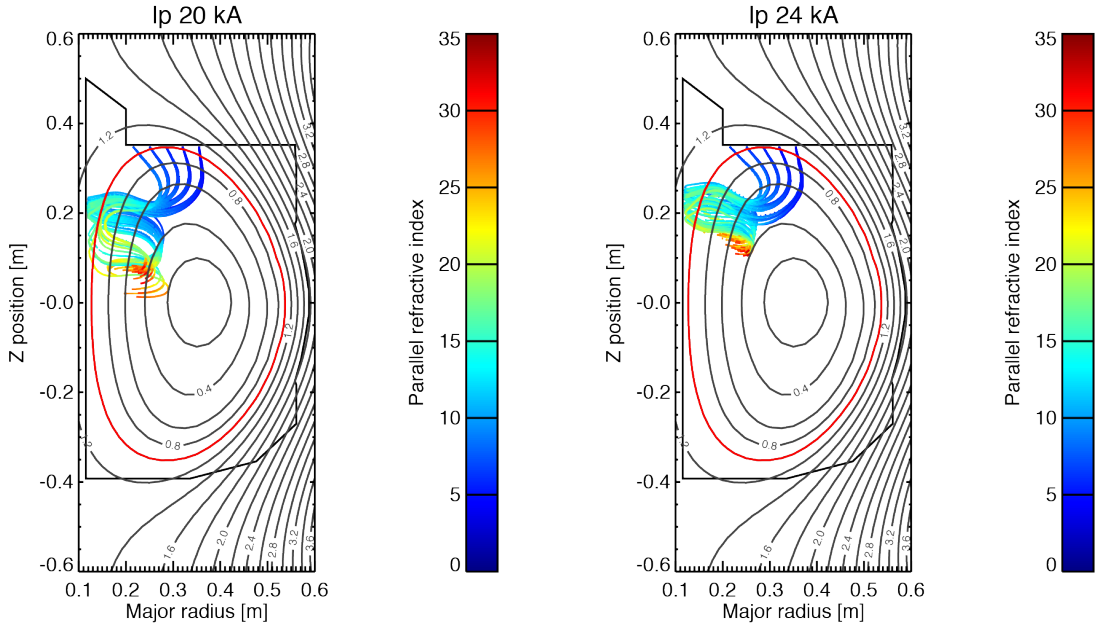

Figure 5.9: Evolution of $N_{\|}$ calculated by GENRAY for $I_{\mathrm{p}} = 20\,\mathrm{kA}$ (left) and $24\,\mathrm{kA}$ (right). $N_{\|}$ upshift is sufficient for strong absorption by thermal electrons.

To summarize the results of GENRAY calculations of the LHW rays launched from

the top of the plasma, the rays converge and are attracted towards the peak of $-P/S$ located on the inboard side, and significant $N_\parallel$ upshift occurs in a specific region in the poloidal cross section due to the balance between the magnetic field line pitch angle and the angle of the LHW resonance cone. Regarding $N_\parallel$ upshift and downshift of the LHW, the effect due to the magnetic field gradient along the magnetic field line [48] and the effect due to the magnetic shear (the radial gradient of the pitch angle) [49] are known. For the former effect, the contribution from the magnetic field gradient ($\propto R^{-1}$) in the direction of the magnetic field line is very small in the vicinity of the midplane and significant $N_\parallel$ upshift in this region cannot be explained. For the latter effect, $N_\parallel$ upshift as the rays travel across the magnetic surface is explained by using toroidal mode number conservation, when $S \simeq 1$ (i.e., $\omega_{\rm pe}^2/\omega_{\rm ce}^2 \ll 1$) so the dispersion relation has no magnetic field dependence, this effect cannot explain $N_\parallel$ upshift while the rays travel on the magnetic surface. Considering the effect of wave stagnation in the poloidal cross section in addition to the effect of magnetic field gradient, the convergence of rays towards the peak of $-P/S$ and the significant $N_\parallel$ upshift in this region can be explained successfully. In the case of top launch, by introducing a magnetic field dependent term in the toroidal mode number conservation equation due to the fact that $\omega_{\rm pe}^2/\omega_{\rm ce}^2 > 1$ near the center of the plasma in a typical TST-2 discharge, an expression in terms of spatially varying parameters such as density and pitch angle was derived as follows,

$$k_\parallel \simeq k_{\parallel 0} \left[\left(1 - \sqrt{\frac{|P|}{S}} \frac{B_{\rm p}}{B_{\rm t}} \right) R \right]^{-1}, \tag{5.2.11}$$

where $k_{\parallel 0}$ is the initial parallel wave number. With this expression, it became possible to estimate the magnitude of $N_\parallel$ upshift analytically without performing ray-tracing calculations. GENRAY calculations showed that the $N_\parallel$ upshift increases abruptly for plasma currents above 16 kA. On the other hand, the experimental result shown in Fig.4.9 indicated that the signal intensity measured by the SBD detector with polypropylene filter showed a drastic increase in discharges with $I_{\rm p} > 15$ kA. In order to investigate the correspondence between $N_\parallel$ upshift and soft X-ray emission, a quantitative comparison of the electron velocity distribution function among different equilibria was carried out using the CQL3D Fokker-Planck code.

Figure 5.10 shows the results of CQL3D calculations using equilibria with $I_{\rm p} =$ 14 kA, 16 kA, 18 kA, 22 kA and GENRAY results. Regarding the current distribution, there is no large change in the current profile which is hollow and peaked around $r/a = 0.6$–0.7. There is a significant difference between the integrated plasma current calculated by CQL3D and the plasma current of the original equilibrium. For this reason, a reliable quantitative comparison cannot be made , but this discrepancy in the plasma current can be attributed to the degree of $N_\parallel$ upshift of the LHW calculated by GENRAY. Regarding the electron velocity distribution function, it can be seen from the right frame of Fig.5.10 that there is a strong inverse correlation between the plasma

current of the equilibrium used and the lowest energy from which the distribution begins to flatten from the Maxwellian distribution. The electron velocity along the magnetic field corresponds well to the phase velocity of the LHW. In addition, the fraction of electrons with kinetic energies of 200—-300 eV, the energy band that passes through the polypropylene filter but not the beryllium filter, starts to increase for equilibrium plasma currents exceeding 16 kA (Fig. 5.11). The top three frames of Fig. 5.12 show the 2-D distributions of the soft X-ray energy flux from the plasma for viewing angles of the SBD detector with polypropylene filter calculated by CQL3D. It can be seen that the soft X-ray energy flux has a strong positive correlation with the plasma current, and is greatly different between equilibria with $I_\mathrm{p} = 16\,\mathrm{kA}$ and 18 kA. In the lower left frame, the energy-resolved soft X-ray intensity is shown. It can be seen that the soft X-ray energy flux in the energy range 200–300 eV increases greatly when the equilibrium plasma current exceeds 16 kA. The integrated soft X-ray energy flux over the entire field of view is shown in the lower right frame of Fig. 5.12

In reality, the integrated energy flux assuming bremsstrahlung emission, calculated by CQL3D, does not match quantitatively with the energy flux measured by the SBD detector (typical signal level of 0.1 V corresponds to $3.6\,\mu$W, while the calculated energy flux is on the order of $0.01\,\mu$W). Although additional processes such as recombination radiation (free-bound transition of electron state) and line emission (bound-bound transition of electron state), and perhaps even particle transport which may drive fast electrons out of the core must be included for improving quantitative estimates, the result of CQL3D calculation that the low energy soft X-ray emission (200–300 eV) increases abruptly above a certain threshold value of the plasma current is plausible.

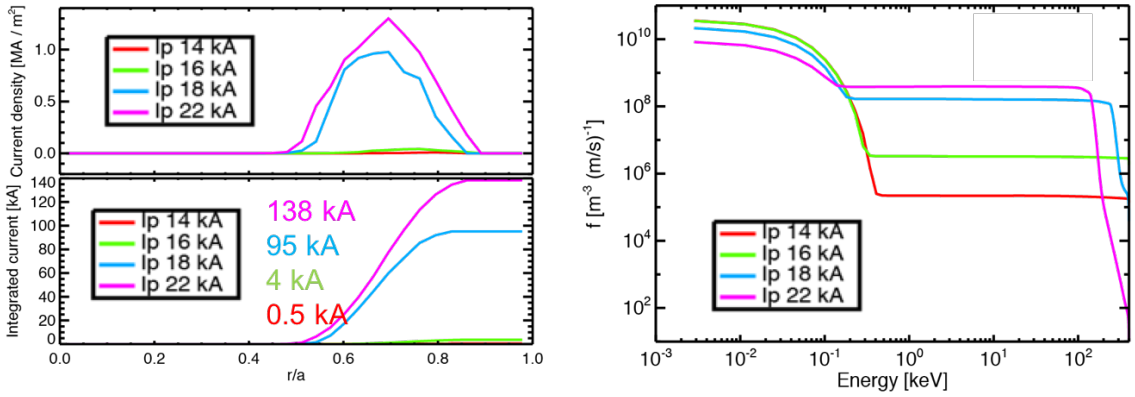

Figure 5.10: The current density profiles (upper left), integrated currents (lower left), and electron energy distribution functions (right) calculated by GENRAY / CQL3D using equilibria with different plasma currents (14 kA, 16 kA, 18 kA, and 22 kA).

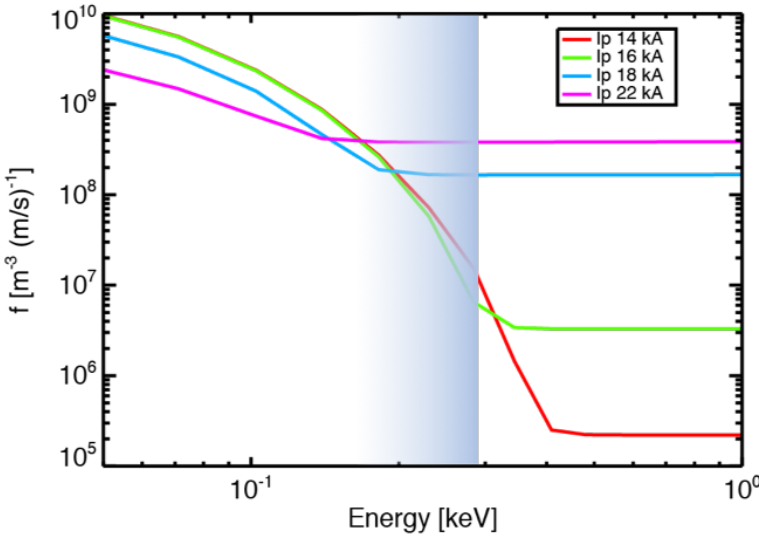

Figure 5.11: Electron energy distribution functions (same as in Fig. 5.10 but over a different energy range). The shaded region (200 eV–300 eV) indicates the energy range that can be detected by SBD with polypropylene filter but cannot be detected by SBD with beryllium filter.

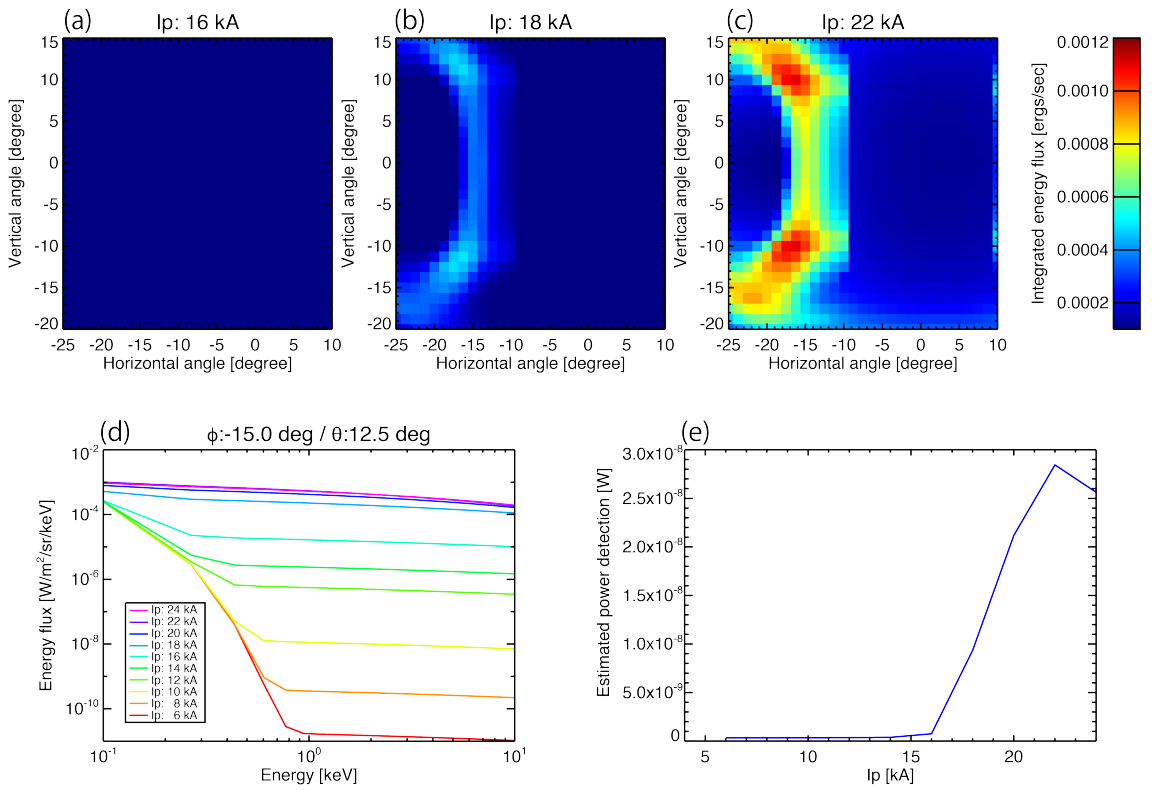

Figure 5.12: Soft X-ray emission calculated by CQL3D. Upper plots show emission profiles for plasma currents (a) 16 kA, (b) 18 kA, and (c) 22 kA as functions of toroidal and poloidal angles viewed from the SBD detector. (d) shows the energy-resolved soft X-ray intensity along the sightline with toroidal angle of −15 degrees and poloidal angle of 12.5 degrees for different plasma currents obtained from equilibrium reconstruction. (e) shows the calculated total bremsstrahlung power that would be observed by the SBD detector.

5.3 Wave simulation in the vicinity of the antennas

Antenna tuning is performed before the antenna is installed inside the vacuum vessel. The wave number spectrum in air (or vacuum) is described in Sec. 3.3. However, it is not obvious whether or not the wave number spectrum remains the same in the presence of plasma. To analyze the behavior of the antenna in the presence of plasma, the RF electric field distribution in the vicinity of the antenna was calculated by the finite element method using COMSOL Multiphysics® [50]. By specifying the spatial distributions of the electron density and the magnetic field in the vicinity of the antenna, the Stix parameters (the parameters D, P, S defined in Sec.2.4) and the cold plasma

dielectric tensor can be evaluated. The wave behavior in the antenna and its vicinity can be calculated. For convenience of calculating the toroidal wave number spectrum, the electron density was chosen to be a function of the vertical position Z for the top-launch antenna and a function of the major radius R for the outboard-launch antenna.

In the case of the outboard-launch antenna, a typical electron density of $10^{16}\,\mathrm{m}^{-3}$ at the limiter edge, measured previously by a Langmuir probe, was used as the limiter density at $R = 585\,\mathrm{mm}$. The density decay length (the length over which the density decreases by $1/e$) in front of the antenna was taken to be 4 mm to match the calculated antenna power transmissivity to the value measured experimentally ($-20\,\mathrm{dB}$). The spatial distribution of the RF toroidal electric field on the midplane excited by the outboard-launch antenna is shown in Fig. 5.13, and the toroidal mode number spectrum is indicated by the red dotted line in Fig. The highest peak is at a toroidal mode number of $n = -14$ ($n = 2\pi N_\parallel R/1.5$ for 200 MHz), which corresponds to $N_\parallel = -5.4$ at $R = 0.621\,\mathrm{m}$ in front of the antenna, which is close to the assumed $N_\parallel$ of -5. However, since the limiter is too close to the first element of the antenna (on the input side), the excited LHW is reflected by the limiter. The reflected component appears at the mirror image toroidal mode number from the main peak of the excited LHW spectrum around $n = +10$. In contrast, Fig. shows the case with the limiter moved farther away by 70 mm in the toroidal direction at $R = 585\,\mathrm{mm}$. By moving the limiter away from the antenna, the amplitude of the reflected component is greatly reduced.

The top-launch antenna has the limiters located 30 degrees away from both ends of the antenna in the toroidal direction. This corresponds to a displacement of 99–196 mm from the outmost elements (which extends from $R = 190\,\mathrm{mm}$ to 375 mm), so the wave number reversal by reflection at the limiters is negligible. On the other hand, since the plasma is not necessarily close to the top limiter and the power transmissivity varies with time, the transmissivity and the wave number spectrum are calculated by moving the density profile relative to the antenna (Fig. 5.14). Specifically, the density profile shown in Fig. similar to the case of outboard-launch antenna is given, and the relationship between the position of the cutoff density layer and the antenna power transmissivity and the excited wave number spectrum are investigated. The distance between the cutoff density layer and the antenna surface is referred to as an antenna-plasma distance.

As shown in Fig. 5.15, the antenna power transmissivity decreases as the antenna-plasma distance decreases, which means that the power injected into the plasma increases. The toroidal mode number spectrum has a peak at $n = -6$ (corresponding to $N_\parallel = -5.1$ for the top-launch antenna centered at $R = 283\,\mathrm{mm}$). Reducing the antenna-plasma distance increases the intensity of this peak, but the intensity saturates when the antenna-plasma distance is in the range 7 mm–17 mm. On the other hand, the peak toroidal mode number $n = 18$ (corresponding to $N_\parallel = 15$ at the top-launch antenna centered at $R = 283\,\mathrm{mm}$) is excited, and when the antenna-plasma distance approaches 7 mm this peak will increase further.

The reason why the secondary peak in the wave number spectrum appears at a wave number of -3 times of the main peak is due to the fact that the phase difference between adjacent elements for exciting the wave number of the main peak is 90 degrees in the case of top-launch antenna (60 degrees in the case of outboard-launch antenna). At the same time, waves corresponding to a phase difference of -270 degrees can be excited simultaneously. In the vicinity of the antenna (where $\omega_{\mathrm{pe}}^2/\omega_{\mathrm{ce}}^2 \ll 1$), the dispersion relation for electrostatic waves asymptotically approaches $k^2 = 0$, and the attenuation length of the RF electric field in the direction perpendicular to the antenna plane become close to the excited wavelength in the toroidal direction. Therefore, a secondary short wavelength component appears only when the cutoff density layer approaches very close to the antenna. In order to maximize the forward power flow subtracted by the reversed power flow, a desirable range of the antenna-plasma distance is 17–27 mm. Based on calculation results, the power transmissivity of the antenna in this range is expected to be 18 % to 40 %. On the other hand, the transmissivity fluctuates during a discharge, but for some discharges with $I_{\mathrm{p}} > 20\,\mathrm{kA}$, the transmissivity is often around 20 %, and it seems that a proper coupling strength can be maintained. An example of such a discharge is shown in Fig. 5.16. During the current ramp-up phase until 50 ms, the major radius was kept not less than 0.34 m, and the antenna power transmittance was maintained around 20 %. However, after 50 ms, the toroidal magnetic field decreased and the plasma current couldn't be maintained. On the other hand, the transmittance exceeded 40 % at 60 ms when the major plasma radius became 0.33 m. As in this shot, there is a clear negative correlation between the size of the plasma cross section and the antenna transmittance, but as long as the top and the bottom limiter is located at the current position, the antenna power transmittance is kept satisfactory when the sufficient plasma major radius is sustained.

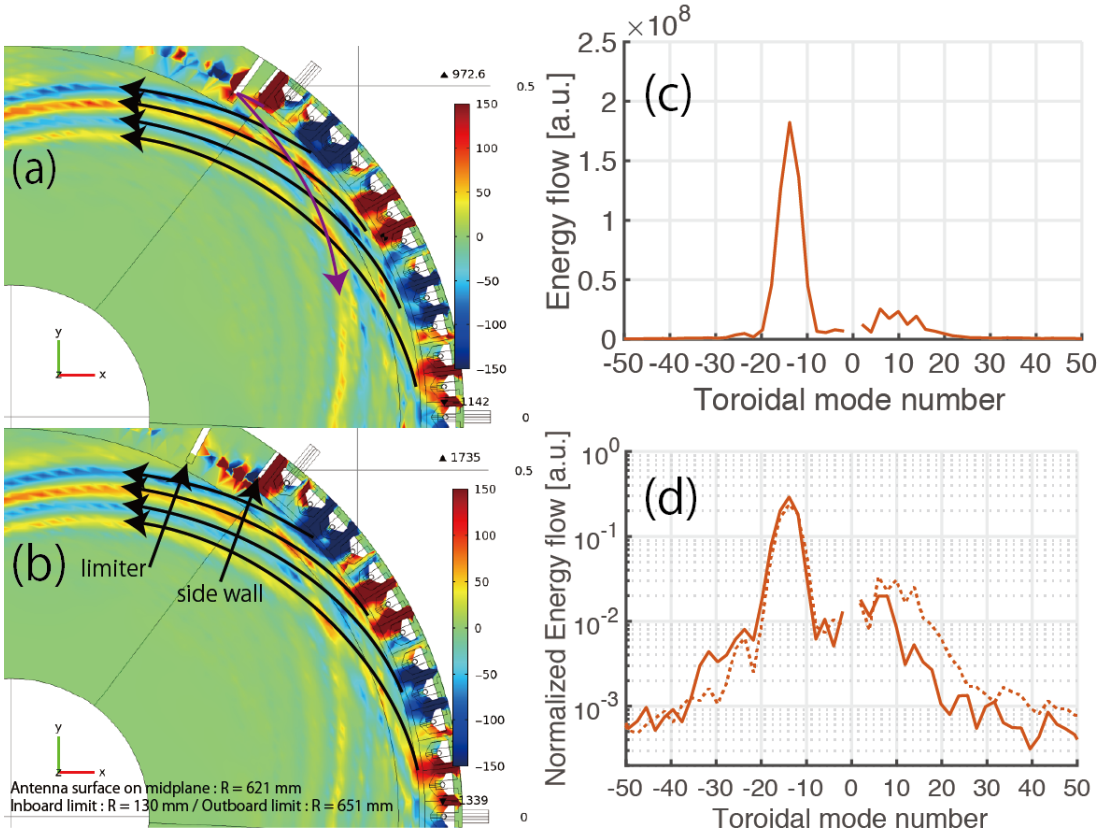

Figure 5.13: (a) and (b) show the toroidal electric field excited by the outboard-launch antenna on the plotting plane calculated by COMSOL with the limiter (a) at the original position, and (b) moved away toroidally by 70 mm. Wave reflection from the limiter can be seen. The limiter is installed to reduce the density in front of the antenna, and the side walls are installed for impedance correction. The electron density ($1.0 \times 10^{16}\,\mathrm{m}^{-3}$) and the $1/R$ dependence of the toroidal magnetic field strength are included in the cold plasma dielectric tensor, but the magnetic field pitch angle due to the poloidal magnetic field is not included. (c) shows the toroidal mode number spectrum of the radial energy flow calculated for the present limiter position. (d) shows a comparison of the toroidal mode number spectrum of the radial energy flow with the limiter at the original position (dashed line) and with the limiter moved away toroidally by 70 mm (solid line). The toroidal mode number n_t of the 200 MHz LHW is given in terms of $N_\parallel$ as $n_\mathrm{t} \simeq 2\pi N_\parallel R/1.5$ near the antenna, where R is the major radius.

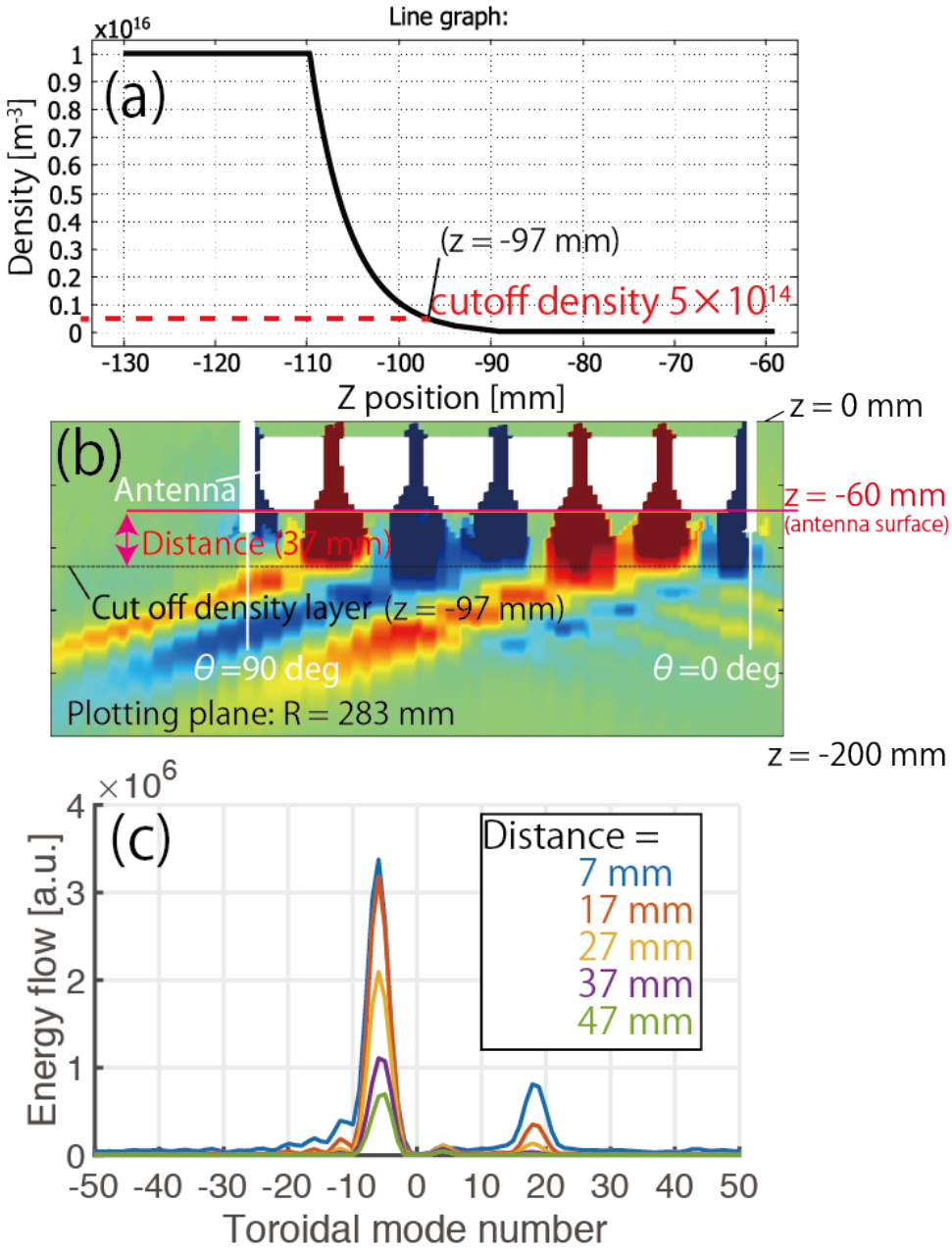

Figure 5.14: Effect of the antenna-cutoff distance on the excited toroidal mode number spectrum for the top-launch antenna calculated by COMSOL. (a) shows the density profile in the vertical direction, and (b) shows the antenna-cutoff distance and the toroidal electric field distribution on the plotting plane $R = 283\,\mathrm{mm}$. In this case, the cutoff density layer is located at $z = -97\,\mathrm{mm}$ and the antenna surface is at $z = -60\,\mathrm{mm}$, so the antenna–plasma distance is 37 mm. (c) shows the excited toroidal mode number spectrum of the vertical energy flow for different antenna-plasma distances from 7 mm to 47 mm.

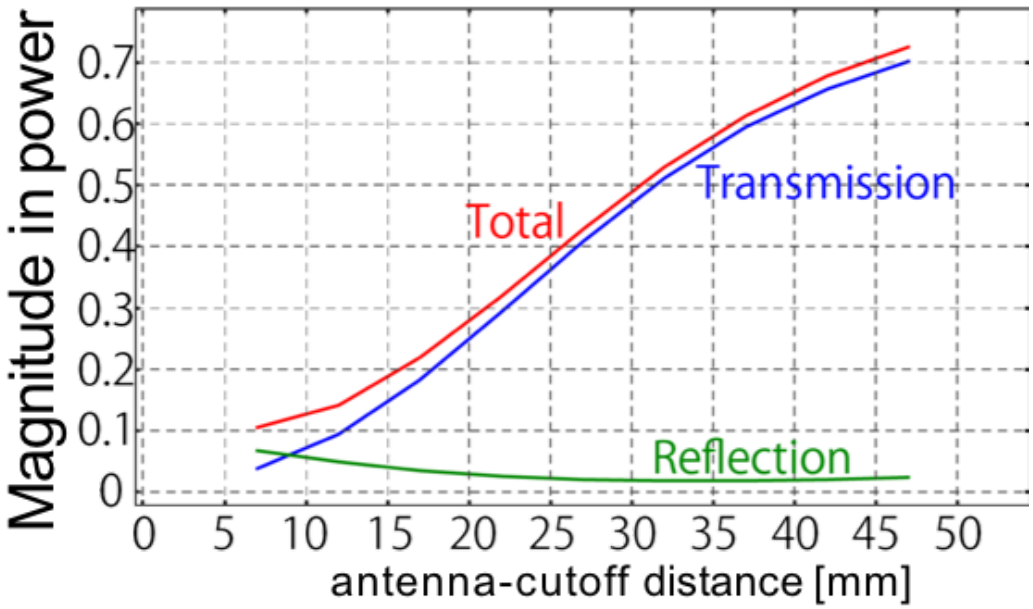

Figure 5.15: The reflectivity, transmissivity and their total of the top-launch antenna as a function of antenna-cutoff distance calculated by COMSOL.

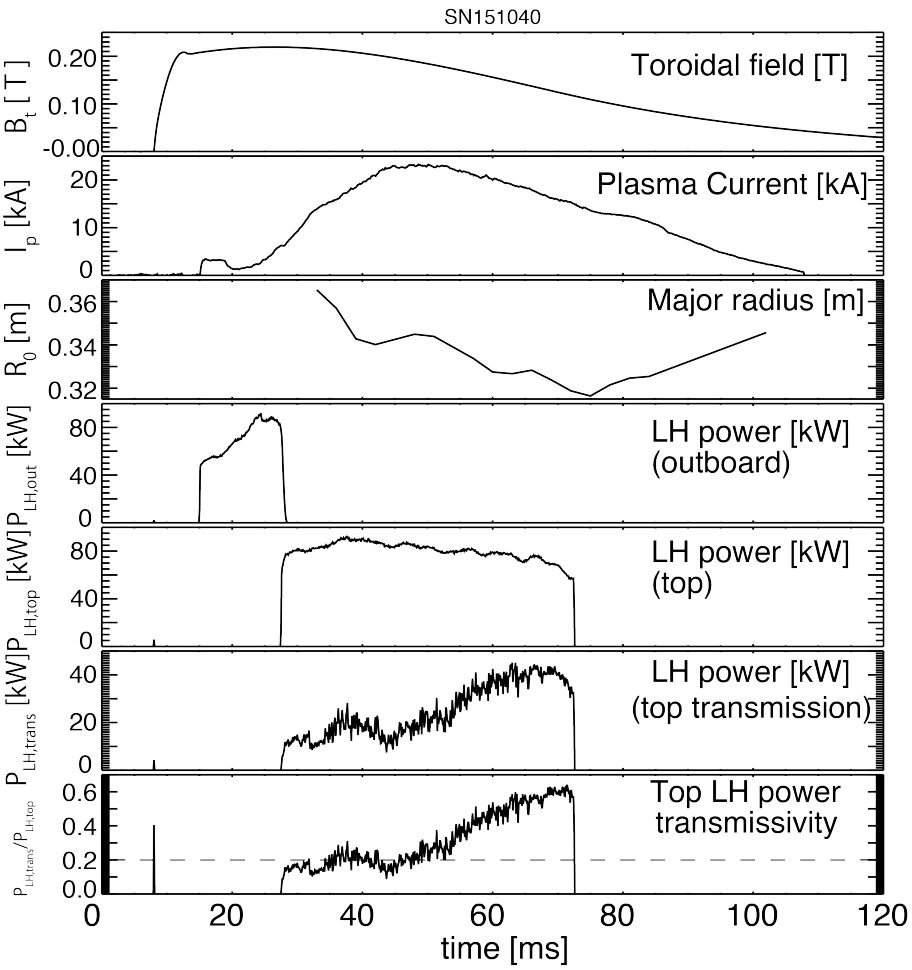

Figure 5.16: An example of the discharge with top launch. The maximum plasma current is 23 kA, and the antenna power transmissivity is around 20% at the peak plasma current (50 ms). Parameters plotted are: toroidal magnetic field at $R = 0.38$ m (near the plasma center), toroidal plasma current, major radius of the geometric center, LHW input power from the outboard antenna and the top antenna, LHW power transmission and the transmissivity of top antenna.

Chapter 6

Conclusions and Future Development

6.1 Conclusions

In order to realize an economically competitive tokamak fusion reactor with low aspect ratio, elimination (or significant reduction) of the central solenoid is required. Methods of non-inductive current drive and current ramp-up using the LHW are being developed on the TST-2 spherical tokamak. A unidirectional travelling LHW can transfer wave momentum (and energy) to electrons by Landau damping. As demonstrated in previous studies, the CCC antenna has the advantages of high wave excitation efficiency and high directivity of the parallel wave number spectrum compared to conventional waveguide array antennas. In this thesis, current drive characteristics are compared among different LHW launching schemes using the newly developed top-launch CCC antenna in addition to the existing outboard-launch CCC antenna. The launching schemes are outboard-launch, top-launch, and simulated bottom-launch. Bottom-launch is simulated by top-launch with the direction of the toroidal magnetic field reversed.

For discharges with the top limiter position at 350 mm, the highest plasma currents achieved were 21.1 kA by outboard launch, 26.0 kA by top launch, and 26.7 kA by simulated bottom launch. In the case of outboard launch, the highest plasma current was observed at toroidal magnetic fields around 0.13–0.14 T. In the case of top launch, the highest plasma current was observed at toroidal magnetic fields around 0.19 T. The average plasma current ramp-up rate for discharges with the major radius of 0.32–0.33 m were 0.91 MA/s for bottom launch, 0.76 MA/s for top launch, and 0.53 MA/s for outboard launch. The superiority of the top-launch antenna was confirmed. However, the installation of the top-launch antenna limited the cross sectional area of the plasma, and the driven plasma current was reduced. When the vertical position of the antenna was raised from 300 mm to 350 mm (height of the top limiter edge measured from the midplane), an increase in the plasma current from 18 kA to 21 kA was confirmed, in the

case of outboard launch. A comparison of discharge waveforms for different launching schemes but with similar LHW powers (80 kW) and plasma major radii (around 0.34 m) was made. The maximum plasma currents were 23.5 kA for bottom launch, 21.5 kA for top launch, and 19.5 kA for outboard launch.

Based on the calculation of GENRAY, the top antenna was introduced with the aim of being able to increasing the parallel wavenumber and mitigate the density limit at the core region while propagating toward the center of the magnetic axis. The wavenumber increase was thought to be due to the change in the pitch angle. By using the top antenna, it became possible to significantly increase the current. There is a comparison of stationary solutions using GENRAY / CQL3D, which gives the explanation that the wavenumber upshift along the magnetic surface enables the broad Landau damping in velocity space. It can be seen that these simultaneous injections have the best synergistic effect with respect to current drive. In addition, simultaneous incidence of the top-launch antenna and the outboard-launch antenna with the reversed toroidal magnetic field is expected to provide a better synergistic effect than simultaneous injection without the reversed field. In the case of top launch, LHW propagates along the certain magnetic surface (around $r/a \sim 0.5$). The wavenumber was increased as it propagated. This is because the deviation from the magnetic axis of the $-P/S$ peak (S becomes inversely proportional to B^2 where $\omega_{\mathrm{pe}}/\omega_{\mathrm{ce}} > 1$) and the slowing down of the wave (pitch angle and the angle of resonance cone are balanced).

In order to investigate the spectrum of the antenna in the presence of plasma, calculations were performed using COMSOL Multiphysics®. For the outboard antenna, the electric field near the antenna was calculated based on the past probe data and measured antenna transmission ratio. The peak of the spectrum is about $N_{\parallel} = -5.4$, and the wavenumber is not greatly different from the tuning value $N_{\parallel} = -5$. As a result, it is found that the limiter for suppressing the density in the vicinity of the antenna reflects a part of the wave, and the peak of the spectrum appears in the opposite direction. It is also found that the reflection can be significantly reduced by shifting the limiter position for about 70 mm. For the top antenna, calculations were performed by giving the same density gradient as the outboard antenna near the antenna. As a result, the wave number of the peak hardly depends on the distance between the antenna and the plasma, which is about $N_{\parallel} = -5.1$, which is almost the same as the value at the time of tuning. As the distance between the antenna and the plasma becomes closer, the transmission power of the antenna decreases and the injected power into the plasma increases. However, it was found that the short wavelength component in the opposite direction is excited when the distance becomes excessively small. As a result, it was considered that the distance between the antenna and the plasma was 17 mm-27 mm (antenna transmittance was 18%–40%).

6.2 Future development

An additional RF system at higher frequency (in the range of 450 to 500 MHz) is being planned primarily for core electron heating in TST-2. Propagation properties of the LHW were discussed using Stix parameters P and S in the previous chapter. For the current TST-2 core plasma parameters (density: 10^{17}–$10^{18}\,\mathrm{m}^{-3}$ and magnetic field: 0.1–0.3 T), $|P|$ is inversely proportional to the square of the frequency, and is constant on a flux surface. On the other hand, S is not constant on a flux surface but smaller on the high field side. Based on this consideration, it is expected that the deviation of the peak of $|P|/S$ from the magnetic axis becomes smaller and the LHW tends to propagate closer to the plasma center. Although the effect of parallel wavenumber upshift/downshift was discussed by comparing the angle of the resonance cone and the pitch angle, since the resonance cone angle $-S/P$ is approximately proportional to the square of the frequency, attraction of the LHW towards the peak of $|P|/S$ becomes very strong at higher frequency in the LHW frequency range. For 450 MHz, P is multiplied by $200^2/450^2 = 0.20$, and the rate of change of S is negligibly small. Since the resonance cone angle becomes larger by a factor of $450/200 \simeq 2.3$, the significant wavenumber upshift seen for 200 MHz LHW and plasma current of 20 kA would require 2.3 times larger pitch angle. It is expected that the parallel wavenumber upshift for top launch and downshift for simulated bottom launch would be gentle until the plasma current approaches 45 kA. Considering conservation of the toroidal mode number, $-PB_\mathrm{t}/SB_\mathrm{p} \simeq 1$ in the vicinity of the midplane for 200 MHz and 20 kA, $-PB_\mathrm{t}/SB_\mathrm{p} \simeq 0.43$ for 450 MHz, so the degree of parallel wavenumber upshift for top launch and 20 kA becomes about 75% $[(1 - 0.43)^{-1} = 1.75]$ and the downshift for simulated bottom launch becomes about 30% $[(1 + 0.43)^{-1} = 0.70]$. Up to now, with the 200 MHz LHW, plasma current ramp up to 27 kA has been achieved. With future improvements, robust LHW injection that is not strongly influenced by the plasma current and the LHW propagation path does not change greatly can be realized by using LHW at higher frequency.

Acknowledgements

First of all, I would like to thank Prof. Takase who is an academic supervisor in the Ph.D. course. I was able to receive guidance and correct advice at any time, I have been saved many times in my dilemma. He also gave me many opportunities to go abroad to see and learn a lot about tokamak devices in the world.

Next, I would like to thank Assoc. Prof. Ejiri and Assist. Prof. Tsujii. They gave me accurate indications and guidelines whenever my understanding of plasma physics or analyses were unsatisfactory.

Also, I would like to thank some other co-researchers. Dr. Syunichi Shiraiwa gave me some insightful suggestions to improve the 3D wave simulation. Dr. Charles Moeller kindly gave me some advice about testing and using the top launch antenna. Dr. Shinya used to be a senior student in the RF team, and I was encouraged by him many times. His current activeness in the research institute has become a big goal of mine.

I'm also grateful to the students in this laboratory. Always funny topics did not run out, and whenever I was in trouble I was saved in many ways, I felt like they were my encouraging friends.

Finally, I would like to thank my parents and my sister for encouraging me to keep going.

Appendix

A Antenna modification and tuning

Installation of the top-launch antenna enabled achievement of higher plasma currents compared to the outboard-launch antenna under the same conditions. However, its installation at the top of the vacuum vessel limited the vertical size of the plasma because the initial position of the top limiter was 300 mm above the midplane, much closer to the plasma than the original top and bottom limiters at $Z = \pm 450$ mm. This restriction limited the plasma cross section and the plasma current. In oorder to ameliorate this limitation, the antenna was raised by 50 mm and the top limiter was moved to 350 mm by shortening the vertical stubs (shorted coaxial lines). This change resulted in some improvement in the driven current. Further improvement required shortening the stubs even more. This was accomplished by increasing the inductance per unit length by reducing the diameter of the inner conductor of the coaxial line. The dependence of the inductance per unit length on the radius of the inner conductor is derived as follows. The relationship between the current that flows on the surface of the inner conductor and the magentic flux per length between the inner and outer conductors is

$$\Phi = \int_a^b dr \frac{\mu I}{2\pi r} = \frac{\mu I}{2\pi} \ln \frac{b}{a}, \tag{A.1}$$

where a is the radius of the inner conductor and b is the radius of the outer conductor. So the inductance per length is

$$\frac{\mathrm{d}L}{\mathrm{d}l} = \frac{\Phi}{I} = \frac{\mu}{2\pi} \ln \frac{b}{a}. \tag{A.2}$$

It is obvious that when the radius of the outer conductor is fixed, the inductance per length is proportional to $-\ln a$. The inductance per unit was doubled by reducing a to 2.5 mm from the initial radius of 6.4 mm. The proper lengths of the stubs were determined by by performing parameter scans with COMSOL to preserve the wave excitation characteristic of the top antenna, including a proper frequency pass band, a proper phase shift between adjacent elements (which determines the wavenumber spectrum), and low enough reflectivity at the operating frequency. The simplest model

of the CCC antenna consists of L-C resonant circuits coupled to neighboring circuits by mutual capacitance (Fig. A.1). Therefore, the same antenna characteristics should be reproduced if the inductance of the stub is conserved. In the parameter scan shown in Fig. A.2, there are two regions with low reflection corresponding to different phase shifts. In the present case, 90 degrees/element would produce the desired parallel refractive index of $N_{\|} \sim -5$.

Tuning of the antenna was perfoemed guided by simulation results of the antenna using LTspice [51, 52]. LTspice runs much faster than COMSOL, so it is suitable for parameter scans. An LTspice model of a single stub was first adjusted to reproduce measurements of a single L-C circuit. LTspice model of the entire top-launch antenna was used to optimize the frequency pass band, phase shift at the operating frequency, and the feeding points at the input and output elements. Antenna tuning was performed efficiently using this approach. The LTspice model and a comparison of the calculated and measured frequency characteristics of the modified top-launch antenna are shown in Fig. A.3

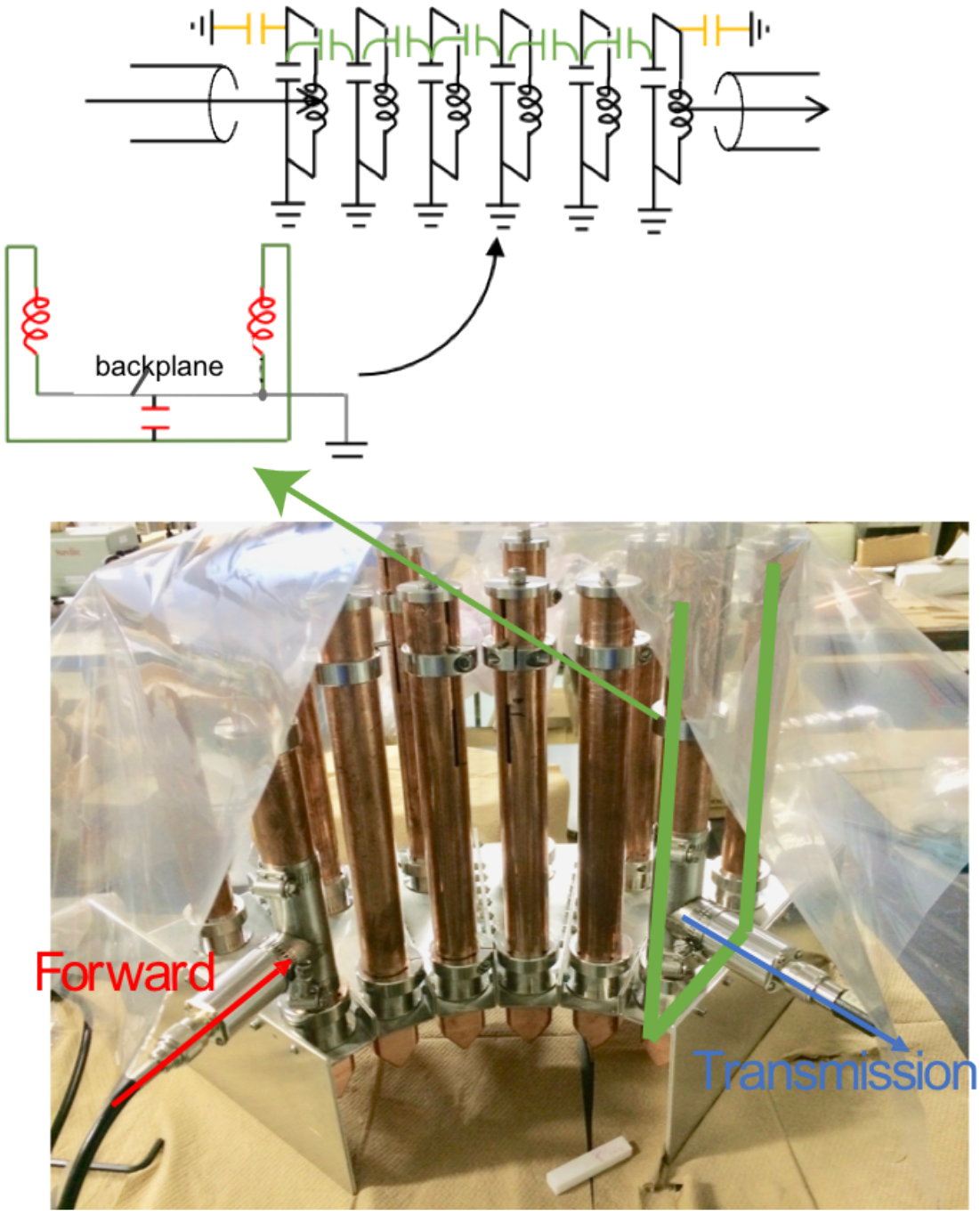

Figure A.1: Simplified circuit model and photograph of the top-launch antenna. In the case of the outboard-launch antenna, the number of L-C circuits is 13.

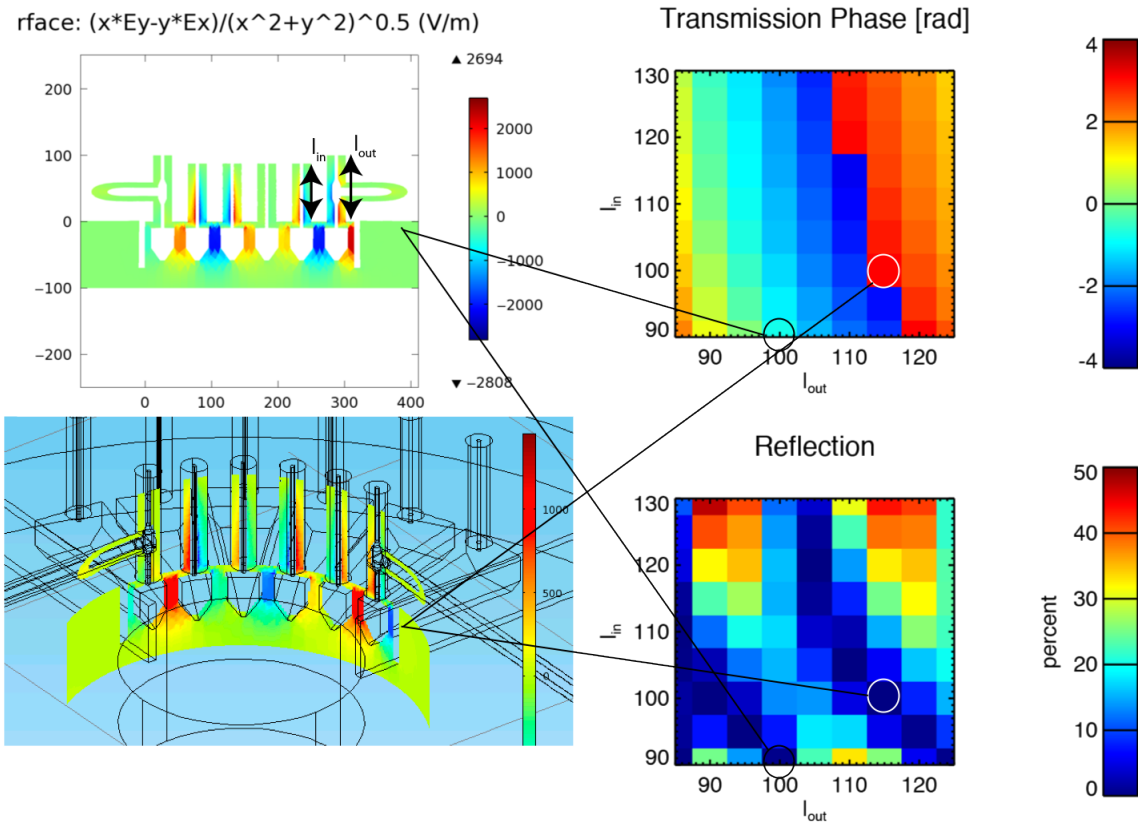

Figure A.2: Results of parameter scan for the stub lengths L_{in} and L_{out} for the top launch antenna. The toroidal electric field distributions for the two regions of low reflectivity are shown on the left. Both cases have low reflectivities, but the phase shifts from the antenna input to the output are different.

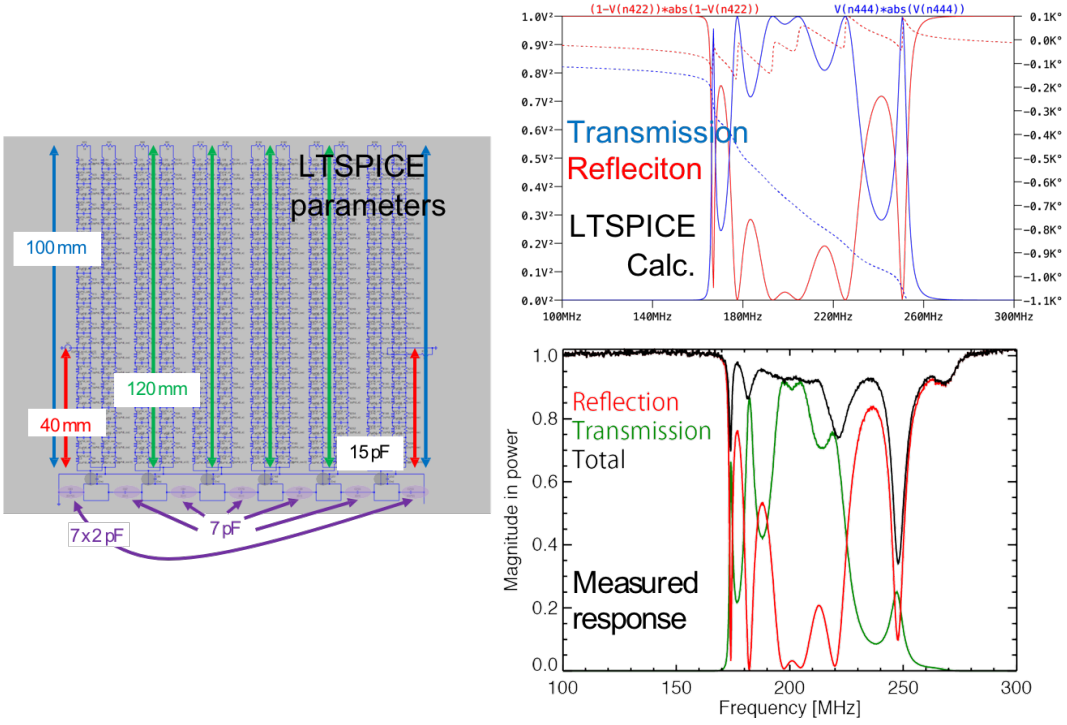

Figure A.3: LTspice model (left), and calculated (upper right) and measured (lower right) frequency characteristics of the top antenna after modification and tuning.

Bibliography

[1] Georgeanne R. Caughlan et al. *Atomic Data and Nuclear Data Tables*, 32(2):197–233, 1985.

[2] File:Binding energy curve - common isotopes.svg - Wikimedia Commons. https://commons.wikimedia.org/wiki/File:Binding_energy_curve_-_common_isotopes.svg.

[3] G. Audi et al. *Nuclear Physics A*, 729:337–676, 2003.

[4] Jet Team. *Nucl. Fusion*, 32(2):187–203, 1992.

[5] H. Kishimoto et al. *Nucl. Fusion*, 45:986–1023, 2005.

[6] C. Theiler. PhD thesis, 12 2011.

[7] R. Raman et al. *Plasma Physics and Controled Fusion*, 56:103001 (19pp), 2014.

[8] Y-K. M. Peng et al. *Nuclear Fusion*, 26:769–777, 1986.

[9] Z. Gao. *Matter and Radiation at Extremes*, 1(3):153–162, 2016.

[10] Y. Takase et al. *Nuclear Fusion*, 41:1543–1550, 2001.

[11] A. Ejiri et al. Ion temperature increase during MHD events on the TST-2 spherical tokamak. Technical report, 2003.

[12] S. Shiraiwa et al. *Review of Scientific Instruments*, 74:1453–1456, 2003.

[13] S. Bernabei et al. *Physical Review Letters*, 49(17):1255–1258, 1982.

[14] W. F. Jobes et al. *Physical Review Letters*, 52(12):1005–1008, 1984.

[15] P. T. Bonoli et al. *Nuclear Fusion*, 58:126032 (15pp), 2018.

[16] Y. Takase et al. *Nuclear Fusion*, 51:063017 (8pp), 2011.

[17] H. Togashi et al. *Plasma and Fusion Research: Rapid Communications*, 9:1202005 (3pp), 2014.

[18] A.. Ejiri et al. *Nuclear Fusion*, 49:065010 (12pp), 2009.

[19] T. Ogawa et al. *Nuclear Fusion*, 41:1767–1775, 2001.

[20] Y. Takase et al. *Nuclear Fusion*, 53:063006 (6pp), 2013.

[21] T. Wakatsuki et al. *Nuclear Fusion*, 54:093014 (14pp), 2014.

[22] T. Shinya et al. *Nuclear Fusion*, 55:073003 (8pp), 2015.

[23] Y and others Takase. *Nuclear Fusion*, 57:102005 (12pp), 2017.

[24] T. Shinya et al. *Nuclear Fusion*, 57:036006 (8pp), 2017.

[25] Y. Takase. 4 Energy Flow and Accessibility. http://fusion.k.u-tokyo.ac.jp/∼takase/plasma1_ch4.pdf.

[26] Thomas H. Stix. *Waves in Plasmas*. 1992.

[27] Y. Takase. 6 Landau Damping. http://fusion.k.u-tokyo.ac.jp/∼takase/plasma1_ch6.pdf.

[28] C. F. F. Karney et al. *The Physics of Fluids*, 22:1817–1824, 1979.

[29] K. Miyamoto. *Fundamentals of Plasma Physics and Controlled Fusion*. 2000.

[30] A Ejiri et al. Plasma current generation and ramp-up by the lower hybrid wave using outboard-launch and top-launch antennas on the TST-2 spherical tokamak. https://conferences.iaea.org/indico/event/151/papers/6165/files/4548-FEC2018preejiriV3.pdf.

[31] Y. Takase et al. *Nuclear Fusion*, 46:S598–S601, 2006.

[32] Tokamak Operations and Engineering. http://www.ga.com/tokamak-operations-and-engineering.

[33] C. P. Moeller et al. *AIP Conference Proceedings*, 289:323–326, 1994.

[34] M. Brambilla. *Physics of Plasmas Close to Thermonuclear Conditions Proceedings*, pages 291–311, 1 1981.

[35] X. Litaudon et al. *Nuclear Fusion*, 30(3):471–484, 1990.

[36] OPTO DIODE: AXUV/SERIESXUV/UVG Salient Applications. www.aptechnologies.co.uk. Technical report.

[37] B. L. Henke et al. *Atomic Data and Nuclear Data Tables*, 54(2):181–342, 1993.

[38] J. H. Hubbell et al. *Journal of Physical and Chemical Reference Data*, 4(3):471–538, 1975.

[39] X-Ray Attenuation Length. http://henke.lbl.gov/optical_constants/atten2.html.

[40] A. Ejiri et al. *Nuclear Fusion*, 47:403–416, 2007.

[41] C. B. Forest et al. *Physics of Plasmas*, 1(5):1568–1575, 1994.

[42] C. B. Forest et al. *Physical Review Letters*, 68:3559–3562, 1992.

[43] L. L. Lao et al. *Nuclear Fusion*, 25(11):1611–1622, 1985.

[44] A P Smirnov. The GENRAY Ray Tracing Code. Technical report, 2003.

[45] S. Yajima et al. *Plasma and Fusion Research*, 13:3402114 (4pp), 2018.

[46] R W Harvey and M G Mccoy. The CQL3D Fokker-Planck Code (reconstituted in editable form from General Atomics Report GA-A20978, 1992). Technical report, 2005.

[47] N. Tsujii et al. *Nuclear Fusion*, 57:126032 (11pp), 2017.

[48] P. T. Bonoli et al. *The Physics of Fluids*, 25:359–375, 1982.

[49] J. J. Schuss et al. *Nucl. Fusion*, 21(4):427–452, 1981.

[50] COMSOL Multiphysics® Modeling Software. https://www.comsol.eu/.

[51] LTspice | Design Center | Analog Devices. https://www.analog.com/en/design-center/design-tools-and-calculators/ltspice-simulator.html.

[52] Katarzyna Opalska. Lumped circuit model of RF amplifier for SPICE simulator. *Proc. of SPIE*, 9290(December 2014):929033–1, 2014.